Extra-Solar Planetary Atmospheres and Interior Structure: Implications for Observational Signatures

Thesis

Extra-Solar Planetary Atmospheres and Interior Structure: Implications for Observational Signatures

Victoria Louise Bending

BA (Hons) (Open University) 2004
MPhys (Durham) 2009

This thesis is submitted for the degree of
Doctor of Philosophy

Department of Physical Sciences
The Open University

Submitted: October 2015

DATE OF SUBMISSION : 30 OCTOBER 2015
DATE OF AWARD : 13 OCTOBER 2016

Acknowledgements

I would like to acknowledge the help of my supervisors, Dr. Stephen Lewis and Dr. Ulrich Kolb, without whose advice and guidance this PhD would never have been completed and for which I am extremely grateful. I would also like to thank Geoff Bradshaw for repeated and patient help with many and varied computer problems (despite 50% of them originating between keyboard and chair). My fellow students, friends, and officemates Maria Duffy, Liam Steele, James Holmes, Alex Barrett, and more all provided a great deal of friendship, support, and advice, as did the wider circle of Coffee Club, without whom I would not only have probably gone insane but also died of caffeine withdrawal. My fellow fiction writers, including Andy Carter, Alan Bradshaw, and Jean-David Bodénan, also provided much-needed windows into other worlds. Finally, I would like to thank my parents for putting up with my endless fretting and for taking on the Herculean task of helping to proof-read this thesis.

Abstract

Hot Jupiter exoplanets are a previously unknown and fascinating field of study. Models of planet formation based only around the Solar System did not predict their existence, occupying as they do the orbital region less than 0.1 AU from their parent stars. Believed to be tidally locked, always presenting the same face to the star, these gas giants are bathed in intense irradiation, and inhabit a regime alien to anything known in the Solar System. As exoplanetary surveys discover an increasing number of planets, the ubiquity of hot Jupiters in the galaxy continues to be confirmed.

Both the evolution and the atmospheric dynamics of these unusual planets are natural focuses of study. However, most authors have historically concentrated on one or the other of these two lines of enquiry, although both are linked. In the case of gas giants in particular, which have no true ground or otherwise easily defined surface layer, the two regimes blend towards the outer layers of the planet. This convergence renders the possibility of model overlap ever more relevant, a possibility that is here studied, both independently and together, ultimately continuing to the modelling of the specific known exoplanets HD 209458b, HD 189733b, and WASP-7b.

It is found that, while it is reasonable for interior evolution model results to be used to provide boundary conditions and atmospheric characteristics for the purposes of three-dimensional atmospheric modelling, the reverse is a much more difficult proposition, providing few truly relevant constraints. Observational characteristics are also predicted, with cyclic variability found in the case of HD 209458b, a more permanently variable state in the case of HD 189733b, and very little longitudinal temperature variation for the calmer atmosphere of WASP-7b.

Contents

Chapter 1. Introduction 1

Chapter 2. Background 9
2.1. Exoplanets: Discovery and Observation 11
2.2. Atmospheres of Exoplanets 20
2.3. Interiors of Gas Giants 30

Chapter 3. Atmospheric Modelling 35
3.1. PUMA 38
3.2. Experiments 42
3.3. Discussion 67

Chapter 4. Interior Modelling 69
4.1. MESA 70
4.2. Experiments 78
4.3. Discussion 89

Chapter 5. Connecting the Interior and Neutral Atmosphere 91
5.1. The Atmosphere as Influenced by the Interior 92
5.2. Insight into the Interior from the Atmosphere 105
5.3. Specific Exoplanets 110
5.4. Discussion 123

Chapter 6. Conclusions 125
6.1. The Evolution of Hot Jupiter Exoplanets 126
6.2. The Atmospheres of Hot Jupiter Exoplanets 126
6.3. Evolution and Atmospheric Dynamics: Complementary Factors? 128
6.4. Observational Implications 129
6.5. Further Work 131

References 135

CHAPTER 1

Introduction

A large number of gas giant planets have been discovered orbiting with periods of less than 10 days, or within 0.1 AU. The very first extrasolar planet discovered orbiting a Sun-like star (a G dwarf of similar mass, metallicity, and effective temperature), 51 Peg b (Mayor and Queloz, 1995), is such a planet, with an orbital distance of 0.05 AU and a period of just over 4 days. Subsequent discoveries proved conclusively that this was no outlier, but a member of a new class of planets now commonly known as "hot Jupiters". Previous solar system formation models, which naturally placed gas giant planets in the outer reaches of their systems, where they are observed in the Solar System, did not expect such large planets so close to their parent stars. It is now widely held that these hot Jupiters formed far from the star, as is necessary for them to obtain large quantities of light elements, but then proceeded to migrate inwards, often disrupting the orbits of other planetary bodies in the process. For a review of the current understanding of the causes, processes, and possible outcomes of planetary migration, see, e.g. Baruteau and Masset (2013); Kley and Nelson (2012).

Observations have demonstrated that stars, brown dwarfs, and planets exist on a continuum of masses, and they must be categorised accordingly. The International Astronomical Union has adopted the following working definitions for these objects. (Boss et al., 2003) The definition of a star is relatively little debated, as this is any object large enough to ignite hydrogen fusion in its core. Thus, any object with a mass above $75M_{\mathrm{J}}$ (that is not a stellar remnant, i.e. a black hole, neutron star, or white dwarf) is a star. Deuterium fusion, however, begins in much lower-mass objects, with a limiting value of only $13M_{\mathrm{J}}$. Sub-stellar objects of greater mass, wherever located, are considered brown dwarfs, while objects of lesser mass are considered planets by the IAU provided that they are in orbit around a larger body, be it a brown dwarf, star, or stellar remnant. Free-floating objects of "planetary" mass are considered a separate category of sub-brown-dwarfs, unless they can be shown to have been ejected

from a planetary system. As a working definition, this definition is likely to evolve in the future as our knowledge expands.

Orbiting at such small distances, well within the orbit of Mercury (0.4 AU), hot Jupiters may have effective temperatures of up to 2,000 Kelvin due to the enormous quantities of energy received from their parent stars. They are believed to be tidally locked due to their close proximity, with the period of rotation identical to the period of the orbit, guaranteeing that the same side of the planet always faces the star. This immense flux of energy affects the long-term evolution of the planet, and the extreme heat input on only one side creates a unique pattern of atmospheric forcing. In many ways, hot Jupiters are utterly unlike any planets previously known.

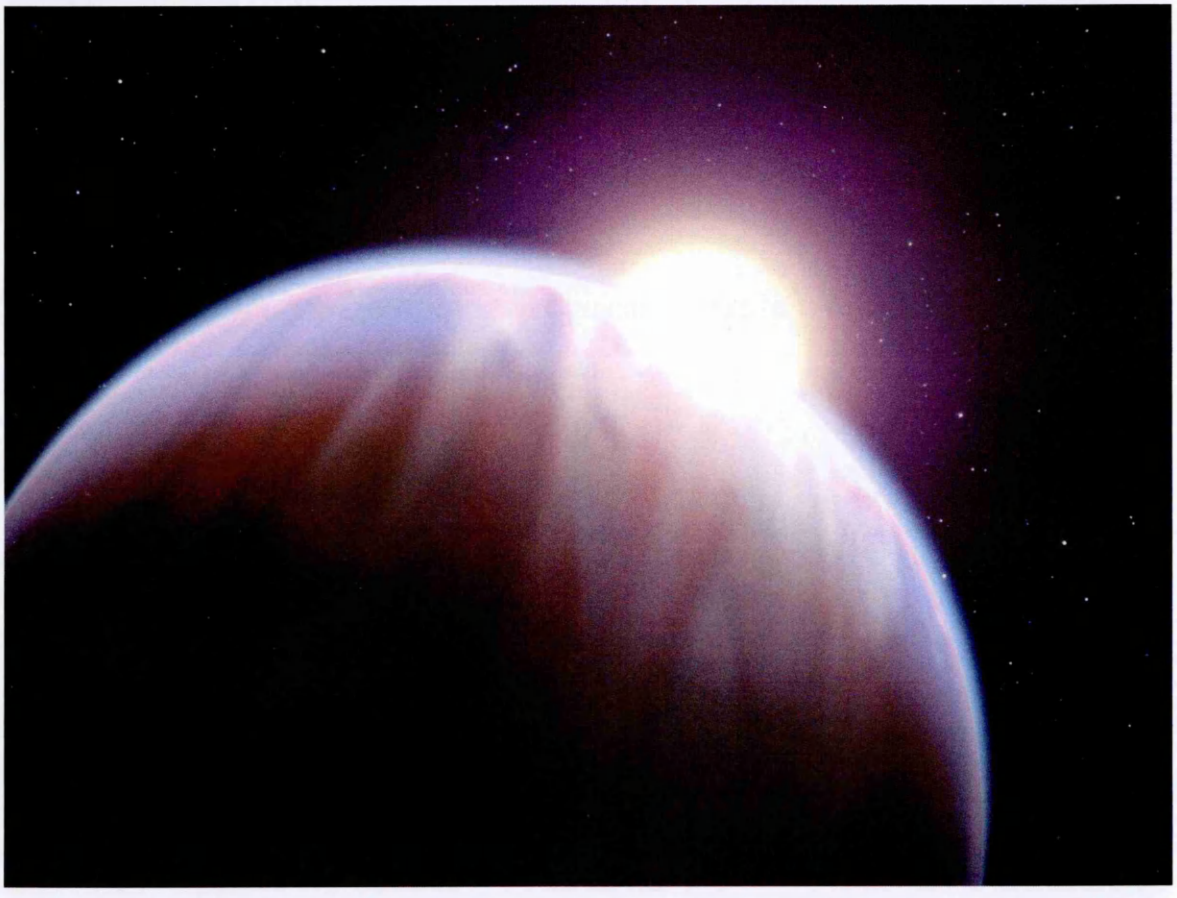

FIGURE 1.1. Artist's impression of hot Jupiter HD189733b, with its host star partially visible beyond it. Although the planet cannot be directly imaged as depicted here, light passing through its upper atmosphere has enabled transmission spectra to be studied, and careful monitoring of the light curve used to infer temperatures in the atmosphere. Image credit: NASA/ESA.

Although many studies have been made individually of the possible formation histories of these planets, and of their likely atmospheric conditions, few authors have investigated the interdependence of these two lines of enquiry since the papers by

Guillot and Showman (2002); Showman and Guillot (2002). This work aims to provide additional perspectives, not only on the post-migration evolution and atmospheric conditions of hot Jupiter exoplanets, but also on how the evolution may affect those atmospheric conditions, and whether the atmospheric conditions appreciably affect the evolution. With some large-scale observations of atmospheric conditions already available, such as the temperature map of HD 189733b produced by Knutson et al. (2007) (see discussion in Chapter 2, Section 2.1), this work further aims to apply the knowledge gained to predictions of factors that are now observable or will likely become observable with next-generation instruments.

Hot Jupiters inhabit an atmospheric regime very different to Solar System gas giants, which rotate on timescales unrelated to the length of their orbits and whose energy input from the Sun is comparable to or less than the energy emerging from the planet's core. The interior flux from a hot Jupiter, on the other hand, will be much lower than the energy input from the parent star, and all this energy is predicted to be incident on only one side of a typical (tidally locked) hot Jupiter. Although various authors have studied this circulation, few of the available simulations are easily comparable, performed with different models under different conditions. Few of these models have been directly compared in this regime, with the only intercomparison test to date performed by Heng et al. (2011) based on the work by Menou and Rauscher (2009). Such tests facilitate the interpretation of future studies, allowing model differences to be taken into account and separated from physical effects of altered simulation parameters, a difference particularly important in the poorly-constrained area of exoplanetary atmospheres. A first objective of this work in the study of exoplanetary atmospheres was thus to perform the intercomparison test of Heng et al. (2011), producing detailed diagnostic information for use in both future tests and by future modellers. Subsequent to this test, specific known exoplanets are then simulated, using a selection of both well-studied and relatively unstudied planets.

The evolutionary history and interior structure of gas giants is a long-studied subject, yet even those of our Solar System remain mysterious to a degree. Jupiter, for example, could still have a rocky core of up to 20 Earth masses, or no solid core at all. (Nettelmann, 2011) Hot Jupiters in general occupy a far broader swathe of parameter space, with masses up to the deuterium-burning limit, and observed radii in some cases

much larger than ordinarily predicted. Possible evolutionary scenarios for these planets are investigated, first in the general sense, and then for a selection of specified planets. The number of factors at play over the course of a hot Jupiter's existence are immense: from formation to migration (including planet-planet interactions or even collisions); core mass, absence, or erosion; chemical composition; irradiation; tidal influences due to the close orbit; and more. The evolutionary investigation is thus here limited to the factors of gross composition (metallicity), the mass of an entirely non-interacting core, and the degree of irradiation.

Atmospheric and interior modelling of hot Jupiter exoplanets are active and rapidly growing fields of research in their own right. However, little work has been done connecting the two, or studying the potential for one form of model to influence the other. This thesis further aims to unite the two strands of enquiry, applying the results of interior modelling to atmospheric simulations and vice versa, and investigating the resultant effects. Finally, the two strands of modelling are performed in sequence on the chosen 'real' exoplanets previously studied, allowing the precise differences that result to be elucidated.

Beginning with the very earliest detections of extrasolar planets (Wolszczan and Frail, 1992; Mayor and Queloz, 1995), astronomers have striven to learn more about these distant, fascinating objects. Though very few planets can be directly imaged, a wealth of observations from both ground- and space-based facilities now provide data on the conditions of hot Jupiters. Currently active space missions dedicated to searching for and observing exoplanets are Kepler, now in a second mission phase after component failures reduced its pointing accuracy, and GAIA, which will release its first data to the public in late 2016, with CoRoT, a previous planet-hunting satellite, de-orbited in 2014.

Beginning with transmission spectroscopy of the upper atmosphere of transiting exoplanets, obtained during the transit while the planet lies directly between Earth and its star, the first hints of spatial resolution have now been obtained in a temparature map of HD 189733b by Knutson et al. (2007), while high-altitude winds have been detected on HD 209458b by Snellen et al. (2010). Such observations are greatly rewarding, but require hours of observing time on powerful telescopes. If the detection thresholds for these and more types of observations can be characterised according

to the likely conditions prevailing on each planet, observing time can potentially be used more efficiently, and the requirements to observe signatures beyond the capability of current telescopes may be used to inform the construction of next-generation equipment. The results generated throughout the thesis are examined for observing potential, either now or in the future.

The questions this thesis seeks to answer can thus be summarised as follows:

(1) How does the interior structure of a hot Jupiter evolve?

(2) How does the atmosphere of a hot Jupiter behave?

(3) To what extent do these factors affect one another?

(4) What conclusions can be drawn for future observations?

In order to study the atmospheric conditions prevailing upon hot Jupiter exoplanets, the freely available simple GCM PUMA was chosen. Its fully free, modular code and long modelling ancestry, together with its simplicity, which is an asset in modelling such a poorly constrained problem, make it an attractive choice for such a project. Originally designed for Earth, PUMA has not previously been used in the modelling of gas giants, so it was necessary to test it in this environment, and to write additional code to permit it to simulate the strong day-night forcing characteristic of hot Jupiters. It was then applied to both the previously mentioned intercomparison situation, and new simulations of known exoplanets, using all available constraints from the data. Finally, its interaction with the results of MESA is investigated, and again applied to known exoplanets, both well-studied, allowing results to be compared with others in the literature, and less so, generating new predictions.

To model the interior structure and evolution of hot Jupiters, the freely available community model MESA was chosen. Like PUMA, it is fully free, with modular, up-to-date code. It also has an active online community of users constantly working on improvements and extensions to the code, resulting in support and advice from experienced users being permanently available if required. MESA is a stellar model by design, with modifications recently added extending it to simulate gas giant planets. The modularity of this code renders it particularly extensible as new functionality is required. After testing, MESA was used to investigate a sector of the parameter space that hot Jupiters inhabit, followed by specific modelling of certain planets, and finally

studying what inferences can be drawn from PUMA models to set the MESA boundary conditions, and the extent to which this affects the planetary evolution.

Chapter 2 outlines the background of the search for exoplanets and the rich history of modelling planetary atmospheres and stellar and gas giant interiors, as well as discussing the work done to date on modelling exoplanets in both fields. This in-depth analysis of the field sets the stage for the subsequent modelling work carried out in Chapters 3, 4, and 5.

In Chapter 3, the atmospheric model PUMA is introduced in greater detail. It is benchmarked against other models used in the field of exoplanetary atmospheric modelling, following the tests originally proposed by Heng et al. (2011). These tests are further expanded upon, producing mean and standard deviation plots and studying more aspects of the circulation than previously. Benchmark tests provide a full set of standard parameters on which model runs are to be based, allowing for direct comparison of different models. Such tests are vital in determining the degree to which the results of a given model are due to the planetary conditions, and thus may be considered to potentially reflect reality, and which are artefacts of the model in question. Studies are then carried out using the planet of the benchmark as a base point from which to investigate the effects of varying individual parameters, such as the planetary radius, in the hot Jupiter regime.

Chapter 4 introduces and tests the stellar and gas giant interior structure model MESA. It is then applied to "standalone" scenarios covering a broad range of possible exoplanetary parameters. The effects of the variation of parameters such as metallicity or core mass on the final state of the planet is investigated. Further, more specific studies are additionally conducted, mimicking the conditions of known exoplanets, and their results compared with other, similar studies of the same planets.

Chapter 5 then proceeds to unite the two strands of enquiry. In this chapter, selected MESA models from Chapter 4 are used as the basis for PUMA studies, and additional MESA models are run using the outer boundary constraints provided by certain PUMA runs in Chapter 3. Finally, the known planets HD 209458b, HD 189733b, and WASP-7b are studied using both models. Despite the relative simplicity of the parametrisations, they show distinct and potentially recognisable signatures.

Finally, Chapter 6 draws together the conclusions of all the preceding chapters, and further advances them to the predictions that may be made for the results of observations both now and in the immediate future.

CHAPTER 2

Background

Although humans have stared at the sky since before recorded history, the first exoplanets were only discovered in recent decades, with the first extrasolar planet discovered around a pulsar by Wolszczan and Frail (1992), and the first planet discovered about a Sun-like star by Mayor and Queloz (1995). Dwarfed in every way by the stars that host them, they require sophisticated instruments to detect. Although transit observation and precise measurements of the star's radial velocity have been the most rewarding avenues of detection, exoplanets have also been discovered through astrometry (Muterspaugh et al., 2010), direct imaging (Bonnefoy et al., 2011), pulsar timing (Wolszczan and Frail, 1992), and even gravitational microlensing (Bond et al., 2004).

As the field of exoplanet observation has expanded, going from just a handful of known planets to over a thousand, so the variety of planetary types has increased. In addition to the small, rocky planets and distant gas and ice giants of the Solar System, rocky "Super-Earths" up to ten Earth masses have been discovered, and gas giants larger than Jupiter found in locations far closer to their stars than the orbit of Mercury. The continuum of planetary masses and locations has grown far more diverse than might have originally been expected, and it can no longer be assumed that Solar System planets are typical of more than a small proportion of planetary systems.

Possibly the largest multi-planet system currently known is HD 10180, potentially containing 9 planets. Tuomi (2012) re-analysed HARPS (the High Accuracy Radial velocity Planet Searcher) radial velocities obtained between 2003 and 2009, and discovered periodicities corresponding to nine planets, rather than the initially proposed number of five to seven (Lovis et al., 2011). These planets are all of relatively small minimum mass, with $m_p \sin(i)$ between 1.3 and 65.8 $M_\oplus$, and are located between 0.022 AU to 3.5 AU from the star, with the least massive planets generally closer than the most massive. Some other examples of large exoplanetary systems are Kepler-90, with seven planets (Cabrera et al., 2014; Schmitt et al., 2014), and Kepler-11, with six (Lissauer et al., 2011).

These many-planet systems are unusual among those thus far detected, appearing as more compact analogues of the Solar System, with smaller planets near to the star and gas giants further from it, a feature seemingly more common in many-planet systems than in those with few planets. This may be explained by the process of planetary migration: if a large planet migrates from a distant to a close orbit, it will disrupt the orbits of other planets in so doing, potentially ejecting them from the system or into the star itself. The majority of systems discovered to date contain few planets, and gas giants close to their parent stars. Observational bias may contribute to this to some extent, as planets that are both massive and close to their parent stars are easiest to detect by radial velocity and transit methods, the most successful means of exoplanet observation.

This chapter discusses the current state of the fields of primary importance to this work. First, Section 2.1 briefly summarises the detection and characterisation of exoplanets, outlining the available detection methods with particular attention to transiting planets and providing an overview of the classes of planet known to exist. Section 2.2 then discusses research into atmospheric dynamics and its application to exoplanets. Finally, Section 2.3 covers the evolutionary modelling of stellar and planetary interiors, with particular attention to brown dwarfs and gas giant planets.

2.1. Exoplanets: Discovery and Observation

It has long been hypothesised that stars other than our own harboured planets much like ours. However, until the first detection of an exoplanet about a Sun-like star by Mayor and Queloz (1995), exoplanets were primarily the domain of science fiction. Since that initial discovery, more and more observing time and dedicated programs such as SuperWASP (Pollacco et al., 2006) or the Kepler mission (Borucki et al., 2010) have been dedicated to expanding the field, and now a multitude of exoplanets of all sizes are known to exist, with even more yet to be confirmed and further discoveries announced regularly. Many of these planets are so utterly different to the planets of the Solar System as to defy all expectations. Their study sheds light on the processes by which solar systems form and evolve through time, on the wide variety of stable configurations for planetary systems, on the complexities of tidal effects, on atmospheric responses to previously unimagined conditions, and even on the question that mankind has asked since prehistoric times: are we alone in the universe?

2.1.1. Observation. Exoplanets may be detected in a variety of ways: by observing transits, measuring the Doppler shifts in the spectrum of a star, observing the star's movement, direct imaging (for nearby large planets orbiting young stars), gravitational microlensing, and even measurements of pulsar timings. A variety of other astronomical phenomena, however, may mimic the observational signature of a planet (for example, in the case of transiting systems, a small star transiting a much larger star, or a nearby eclipsing binary blended with the target star), and as such, potential planets that have only been detected by a single program are typically referred to as "planetary candidates" until follow-up observations can confirm or deny the existence of the proposed planet. As of this writing, almost 2,000 planets are known to exist around 1,250 stars (Schneider, 1995-2015).

2.1.1.1. *Transits.* A transit occurs when a planet passes across the face of its parent star as seen from Earth, blocking a small fraction of that star's light. This can only be observed for the fraction of systems with orbital plane essentially edge-on to the line of sight; that is, angle of inclination $i \approx 90°$. Depending on the characteristics of the planet and its orbit, the transit may take a period of time from hours to days, and reoccur on a timescale of days to decades (although transits of the latter timescale are not easily detectable). Planets closer to their stars are more likely to produce transits,

as they can be observed to cross the face of the star from a wider variety of inclinations. In general, the probability P of a transit being observable is related to the radii $R_\star$ of the star and R_P of the planet, and the semi-major axis a of the planet's orbit, by

$$P = \frac{R_\star + R_P}{a} \tag{2.1.1}$$

The radius of a planet will always be small compared to that of a star, and is typically ignored in this calculation, resulting in the simpler equation $P = R_\star/a$. The change in observed flux from a star of radius R_* due to a transiting planet of radius R_P is given by

$$\frac{\Delta F}{F} = \frac{{R_P}^2}{{R_\star}^2} \tag{2.1.2}$$

The typical change in stellar brightness due to a planetary transit is less than 1% (Haswell, 2010), often less than the noise on the observations, though large planets orbiting small stars may produce transit depths of up to a few percent. An idealised schematic of a transit and the associated light curve from the star is shown in Figure 2.1.

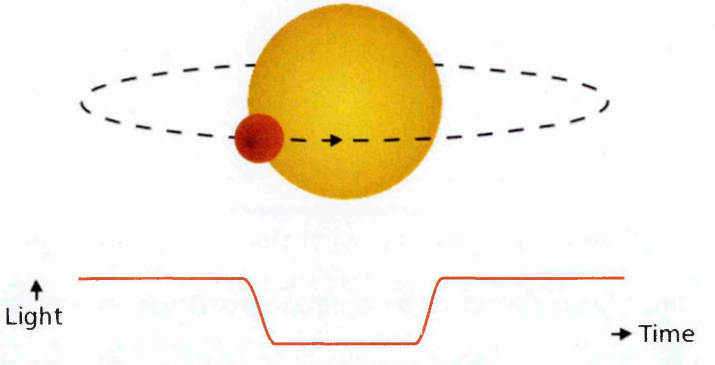

FIGURE 2.1. Schematic illustration of a planet transiting across the face of its star, with the corresponding light curve shown below.

As previously stated, similar signatures can be created by a variety of other astrophysical phenomena, such as transiting dwarf stars, nearby binary stars that are not resolved from the target star, the grazing eclipse of a binary system, or even the presence of a localised quantity of sunspots. Follow-up observations are thus required to confirm the presence of transiting planets following an initial detection. Each type of transit mimic has its own signature, allowing them to be differentiated. Grazing eclipses may be detected from the shape of the transit light curve. Since at no time

is either object completely superimposed over the other, the flux from the system descends to a minimum and then increases, creating a "V" shape rather than the "U" characteristic of a full transit. If the secondary eclipse can be detected, then provided that the two stars are not identical, successive transits will also alternate in depth as each star passes behind the other. Blended eclipsing binaries may be separated by observing with greater angular resolution. Brown dwarf transits are most difficult to distinguish from those of planets, since they reside immediately above them in the mass continuum, and the mass of the transiting object must be determined in order to confirm or deny a planet detection.

Transits deepen with increasing planet size, and are both easier to observe and occur more frequently at lower orbital distances: to observe Earth transiting across the Sun would require a minimum of two years to capture three transits, in the serendipitous case where observations coincidentally began at the time of the first transit, and a maximum of three. The most common types of planet found by transit searches are thus the large, close-in hot Jupiters, but as the duration of active transit-seeking programs increases, steadily smaller and more distant planets may be discovered using the greater amount of data available. The first planet to be detected by its transit was HD 209458b, with initial observations by Henry et al. (2000); Charbonneau et al. (2000).

2.1.1.2. *Radial Velocity.* The radial velocity technique detects the Doppler shift in the star's spectrum as its orbit about the common centre of mass accelerates it first towards, then away from, the Earth, as illustrated in Figure 2.2. The semi-amplitude of the radial velocity, K, of a star of mass $M_\star$ orbited by a planet of mass M_P at inclination i is given by

$$K = \left(\frac{2\pi G}{P_{orb}}\right)^{1/3} \frac{M_P \sin(i)}{(M_\star + M_P)^{2/3}} \frac{1}{\sqrt{1-e^2}} \tag{2.1.3}$$

where P_{orb} is the orbital period and e is the eccentricity of the orbit. (de Pater and Lissauer, 2007)

Radial velocity measurements reveal the mass of the planet as a function of stellar mass and orbital inclination. The stellar mass may be estimated from the spectral class of the star; however, the orbital inclination is known only for transiting planets, which must be at an inclination of 90° in order to be observed crossing the face of the parent star. Planets detected using the radial velocity method can therefore be assigned

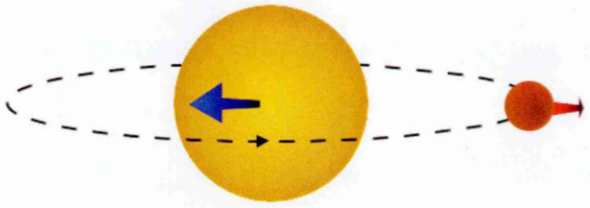

FIGURE 2.2. Schematic illustration of a star and planet orbiting in the same plane as the observer about their common centre of mass. As the star moves closer (and the planet recedes), the light emitted is blue-shifted. In the other half of its orbit, as the star moves away, its emitted light is red-shifted.

only minimum masses. The precision of radial velocity measurements is affected by the number of available spectral lines, making hot stars unfavourable targets. Stellar rotation and the star's intrinsic variability are also important sources of noise in RV measurements.

This technique is most sensitive to systems containing close-in large planets with their orbital plane parallel to the line of sight (inclination $i = 90°$), and insensitive to systems with a perpendicular orbital plane ($i = 0°$). It is thus complementary to the astrometry technique, and is often used to follow up detections of transiting planet candidates, as these planets must all have orbital inclinations of very close to 90° or a transit could not be observed. One of the earliest planets detected by this method was 51 Pegasi b, by Mayor and Queloz (1995).

2.1.1.3. *Astrometry.* Astrometry involves detecting the small motion on the sky of a star circling its system's common centre of mass, as shown in schematic in Figure 2.3. It is most sensitive to nearby systems with distant massive planets, and as such can be considered complementary to the radial velocity technique. If the system is perpendicular to the observer's line of sight, the star will appear to perform an elliptical or circular motion, while for a system in the plane parallel to the line of sight, it will appear to move back and forth along a line. Although there is a history of detections by this method later proven false, one planet discovered entirely through astrometry is HD 176051b, orbiting in a binary system (Muterspaugh et al., 2010).

2.1.1.4. *Direct Imaging.* In systems relatively near to Earth, it it possible to directly detect large, young planets that orbit far from their parent stars. Extremely high resolution imaging is required for such detections, separating the light from the parent

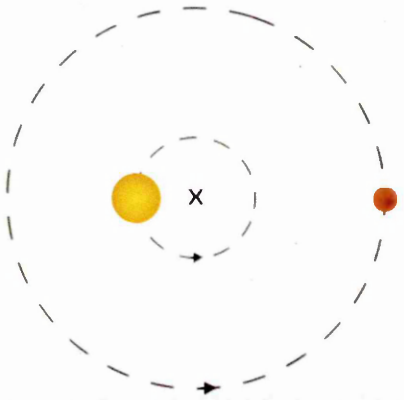

FIGURE 2.3. Schematic illustration of a star and a distant high-mass planet orbiting their common centre of mass, denoted by X, in the plane perpendicular to the observer's line of sight. The planet and star are not to scale, and the size of the star's orbit is exaggerated for clarity. Although the planet is undetectable, the "wobble" in the star's motion across the sky is not.

star from that of the much fainter planet. This resolution can be achieved in one of two ways:

Space-based telescopes are essentially diffraction limited, but are limited in number and size by the cost of getting them into orbit. The diffraction-limited angular resolution θ of a telescope of diameter D observing at wavelength λ is given by the equation determining the first minimum of the Airy disk produced:

$$\theta = 1.22\frac{\lambda}{D} \tag{2.1.4}$$

Ground-based telescopes, by contrast, are cheaper and easier to construct, but must contend with the distortions introduced by the atmosphere. A telescope becomes seriously limited by atmospheric turbulence once its diameter is roughly Fried's coherence length,

$$r_0 \approx 0.114\left(\frac{\lambda\cos(z)}{550}\right)^{0.6} \tag{2.1.5}$$

where λ is the wavelength of the light in nanometres, and z is the zenith angle. (Kitchin, 2003). In the visible range, it can thus be seen that telescopes above roughly 12cm in diameter will be severely affected by the resulting distortions. Since a 12cm telescope is too small to resolve the angular separation of an exoplanet and its parent star, corrective methods must be employed in ground-based observation. Adaptive optics is a system which deforms the telescope mirror to counteract the distortions of the atmosphere, employing a wavefront sensor to detect the aberration in the light produced by a known "guide star" (either a nearby bright star or an artificial "star" generated

by laser excitation of sodium atoms high in the atmosphere) and compensate for it in real-time. A non-specialist overview of adaptive optics is given by Rigaut (2015), and some recent examples of its use in astronomical observation range from Morzinski et al. (2015), imaging the nearby young exoplanet β Pictoris b, to Leethochawalit et al. (2016), studying gravitationally lensed star-forming galaxies at redshift $z \approx 2$.

Two examples of planets detected by direct imaging are shown in Figure 2.4.

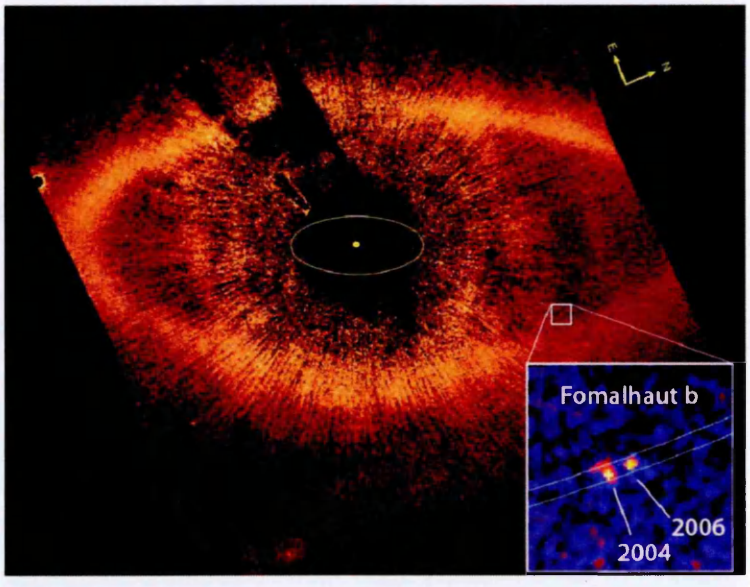

(a) *Fomalhaut b*

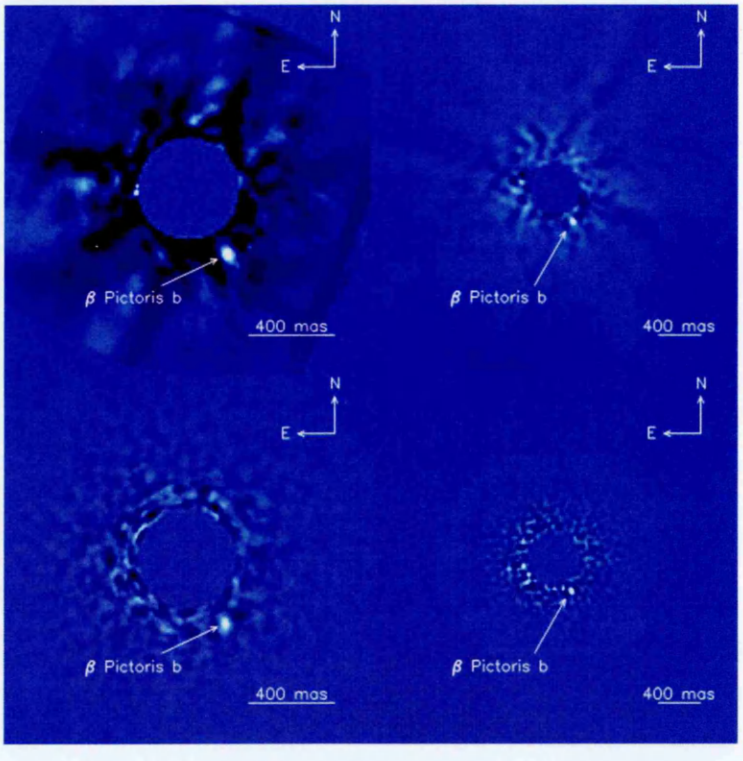

(b) *β Pictoris b*

FIGURE 2.4. Two examples of planets detected by direct imaging. (a) Fomalhaut b, taken from Fig. 1 of Kalas et al. (2008); (b) β Pictoris b, taken from Fig. 1 of Bonnefoy et al. (2011)

2.1.1.5. *Gravitational Microlensing.* Gravitational lensing is the magnification of a background object by a foreground object as the light is bent around it by the curvature of space-time. Microlensing occurs when a foreground star with an orbiting planet passes across a background star. The much smaller additional lensing due to the planet can be detected as a "blip" in the otherwise smooth magnification curve, as illustrated in Figure 2.5. Due to the low probability of observing a lensing event, microlensing surveys typically aim towards the Galactic centre, where the stellar density is highest. (Gaudi, 2012) While planets within a broad range of masses and distances can be detected by this method, its nature means that few have been observed: the first detection was made in 2003 by Bond et al. (2004), and at the time of writing, 40 planets had been detected in 38 systems by gravitational microlensing. (Schneider, 1995-2015) However, the probability of a lensing event is so low that microlensing planets, once observed, will almost certainly never be observed again in a human lifetime.

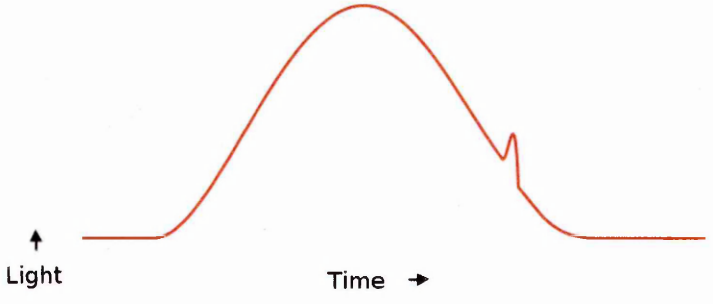

FIGURE 2.5. Example light curve due to a planetary microlensing event. The large increase in brightness indicates the presence of the foreground star, while the small bump is a microlensing event due to a foreground planet.

2.1.1.6. *Pulsar Timing.* Pulsar timing involves detecting small variations in the arrival of the pulses, caused by the motion of one or more orbiting planets. Because pulsars are extremely regular, even minute changes in their timing are distinctive, and periodic fluctuations can be used to detect the presence and mass of an orbiting body. Despite these systems having experienced supernovae in their past, several planets have been detected using this method, and in fact, the first exoplanet detection, by Wolszczan and Frail (1992), was due to pulsar timing variations.

At the time of writing, 19 pulsar planets had been detected, orbiting fourteen pulsars. (Schneider, 1995-2015)

2.1.1.7. *Characterisation.* Once an exoplanet detection has been confirmed, more detailed observations are often made in order to further characterise it, in particular in the case of transiting planets. The mass and radius of these planets can be uniquely obtained, providing the average density and thus the possible types of planet (e.g. gas giant, ice giant, rocky planet; see section 2.1.2 for further discussion). Spectral analysis of the transit may permit transmission spectroscopy of the uppermost layers of the planet's atmosphere. Close analysis of the entire light curve and of the secondary eclipse may reveal an approximate temperature map of the planet, as in the work by Knutson et al. (2007).

2.1.2. Planetary Characteristics. Planets are not all alike in character, as the Solar System amply demonstrates. They vary from small rocky bodies less massive than Mercury, to "Super-Earths", through ice giants such as Uranus and Neptune, up to gas giants more massive than Saturn or even Jupiter.

2.1.2.1. *Rocky Planets.* Rocky planets are potentially two classes of object. The first are small planets below around $10M_{\oplus}$, which never became massive enough to accrete a large gaseous envelope. Mars, Earth, Venus, and Mercury are all examples of this type of planet. The second potential class of rocky planet is the remnant left over when proximity to a star has stripped the envelope of a gas giant, exposing its core. Some small planets in extremely close orbits, such as CoRoT-7b, have been suggested as potential examples of this. (Jackson et al., 2009)

Rocky planets have the highest density of all possible planets, composed primarily of silicates and heavier elements in varying proportions. A purely silicate planet would be relatively light, while more iron-rich ones are increasingly dense. Despite their high density, rocky planets are the least massive type of planet, as rocky bodies that reach greater masses are able to accrete the lighter elements during formation. As the least massive category as well as the lowest in radius, rocky planets are the most difficult planets to detect by all means. However, 136 planets believed to lie within in this mass range have been discovered. (Schneider, 1995-2015)

2.1.2.2. *Ice Giants.* Ice giants, planets similar to Uranus and Neptune, are massive enough to have accreted a sizeable gaseous envelope, but contain proportionally much less hydrogen and helium, the lightest elements, than their gas giant counterparts. "Ices" such as water, methane, and ammonia make up a majority of the mass

of such planets. Whether a given planet is an ice giant or a gas giant may be partially determined from its density, although a large rocky core with a relatively small hydrogen-helium envelope may also pose as such a planet, and spectroscopic observations may be required to determine which is the case.

2.1.2.3. *Gas Giants.* Occupying the mass spectrum up to approximately $13M_J$, beyond which they begin to merge with the category of brown dwarfs, gas giants are composed primarily of the lighter elements. They may have solid rocky or metallic cores, although some of these may have been eroded into the planet as a whole: as well as the likely solubility of water ice in metallic hydrogen (Wilson and Militzer, 2012b), Wilson and Militzer (2012a) find that it may be possible for MgO, a likely rocky core constituent, to dissolve into an adjacent region of metallic hydrogen above temperatures of around 8,000-10,000 Kelvin. Provided that the dissolved elements are subsequently redistributed away from the boundary, this study indicates potentially significant rocky core solubility for planets of Jupiter's mass or greater. Wahl et al. (2013) continue this work to an investigation of the solubility of iron under such conditions, and find that it is likely to dissolve above temperatures of only 2,000 Kelvin where exposed to metallic hydrogen. The presence or absence of a core remains uncertain even for the gas giants of the Solar System, which can be observed in detail, and is another unknown in the study of gas giant exoplanets.

2.2. Atmospheres of Exoplanets

2.2.1. Theory. Three-dimensional atmospheric modelling involves solving the equations of motion for a gas on the surface of a sphere or oblate spheroid. Depending on the complexity of the model, various simplifying assumptions may be used. One of the most common is to reduce the full three-dimensional Navier-Stokes equations to what is typically known as the primitive equations of meteorology. In this case, hydrostatic balance and a shallow atmosphere are assumed (see, e.g. Andrews, 2000; Andrews et al., 1987).

The Navier-Stokes equation for fluid flow in an inertial frame is

$$\frac{D\mathbf{u}}{Dt} = -\frac{1}{\rho}\nabla p - g\mathbf{k} + \frac{\eta}{\rho}\nabla^2\mathbf{u} \tag{2.2.1}$$

The material derivative, the rate of change with respect to time following the motion of the fluid, is defined as

$$\frac{D}{Dt} \equiv \frac{\partial}{\partial t} + \mathbf{u}\cdot\nabla$$

$\mathbf{u}$ is the velocity vector, ρ is the density of the fluid, p is the pressure, g the acceleration due to gravity, $\mathbf{k}$ is the unit vector in the upward direction, and η is the viscosity.

With respect to a rotating frame, this becomes

$$\frac{D\mathbf{u}}{Dt} = -\frac{1}{\rho}\nabla p - 2\boldsymbol{\Omega}\times\mathbf{u} - \boldsymbol{\Omega}\times(\boldsymbol{\Omega}\times\mathbf{r}) - g\mathbf{k} + \frac{\eta}{\rho}\nabla^2\mathbf{u} \tag{2.2.2}$$

$\mathbf{u}$ is now the velocity as measured in the rotating frame, $\mathbf{r}$ the position vector, and $\boldsymbol{\Omega}$ is the angular velocity of that frame. The terms $2\boldsymbol{\Omega}\times\mathbf{u}$ and $\boldsymbol{\Omega}\times(\boldsymbol{\Omega}\times\mathbf{r})$ are the fictional Coriolis and centrifugal forces, respectively, arising from the motion of the rotating frame. These "forces" appear to an observer in the non-inertial reference frame of the rotating planet due to its rotation. The Coriolis force is proportional to the speed of motion, and causes a moving air parcel to appear deflected to the right (left) of its original course from the point of view of an observer in the northern (southern) hemisphere. It primarily affects atmospheric motion at large scales. The centrifugal force is dependent only on position, and acts perpendicularly outwards from the axis of rotation.

In order to model the atmosphere, simplifying assumptions are typically introduced at this point. Although there are various possibilities, those leading to the primitive

equations of meteorology are as follows. First, the atmosphere is assumed to be shallow with respect to the radius of the planet, such that all occurrences of $\mathbf{r}$ can be replaced with the planetary radius a. In the case of the Earth, the planetary radius is approximately 6,400 km, while the atmosphere is only around 100 km thick, or 1.6% of the radius, and this approximation is valid. For gas giants, with typical radii $\geq 10\times$ that of the Earth, this assumption will similarly remain valid as long as the model base (which on a gas giant must be arbitrarily placed, since there is no true solid ground) is set at an appropriate level. Additionally, the atmosphere is assumed to be in hydrostatic equilibrium, allowing vertical acceleration terms to be neglected, as in a shallow atmosphere the horizontal scales are vastly greater than the vertical.

Using these main assumptions, and taking into consideration the requirements of mass conservation and the laws of thermodynamics, the equations often known as the primitive equations of meteorology are then produced. In the form presented in the validation of PUMA's dynamical core (Liakka, 2006), they are:

$$\frac{D\mathbf{u}}{Dt} + f\mathbf{k} \times \mathbf{u} + \nabla_p \Phi = 0 \tag{2.2.3}$$

$$\frac{DT}{Dt} - \kappa T \frac{w}{p} = 0 \tag{2.2.4}$$

$$\nabla_p \cdot \mathbf{u} + \frac{\partial w}{\partial p} = 0 \tag{2.2.5}$$

$$\frac{\partial \Phi}{\partial p} + \frac{1}{\rho} = 0 \tag{2.2.6}$$

Equation 2.2.3 is the momentum equation, Equation 2.2.4 is the thermodynamic equation, Equation 2.2.5 is the continuity equation, and Equation 2.2.6 is the hydrostatic equation, with the material derivative here equating to

$$\frac{D}{Dt} = \frac{\partial}{\partial t} + \mathbf{u} \cdot \nabla + w \frac{\partial}{\partial p} \tag{2.2.7}$$

The horizontal velocity vector (u, v) is now denoted by $\mathbf{u}$, the vertical velocity by w, and the temperature by T. The Coriolis parameter $f = 2\Omega \sin(\phi)$, where ϕ is the latitude. The geopotential is denoted by Φ, and $\kappa = R/c_p$, where R is the specific gas constant and c_p the heat capacity for the atmosphere under consideration. $\mathbf{k}$ remains the vertical unit vector, p the pressure, and ρ the density. The first two of these four equations describe how air moves through the atmosphere (2.2.3) in the rotating reference frame of the planet, and how its temperature changes (2.2.4), while the second two explicitly

express that gas is neither created nor destroyed (2.2.5), and impose the condition of hydrostatic equilibrium (2.2.6). For the purposes of modelling, these equations may be rephrased in terms of vorticity, divergence, and the sigma-coordinate as described in Section 3.1.

2.2.2. Hot Jupiter Exoplanets: Observation and Theory. Although the number and variety of exoplanets now known is immense, and continues to increase, of specific interest to this project is the case of "hot Jupiters": gas giant planets, often with unexpectedly large radii, found extremely close to their parent stars ($\leq$ 0.1 AU) - in some cases, such as WASP-12b (Li et al., 2010; Fossati et al., 2010), these planets are found to be losing their atmospheres to their parent stars, with the potential to become entirely destroyed in the future. It has recently been noted that for those multi-planet systems with known obliquity (now standing at five, excluding the Solar System), the plane of the planetary orbits is almost perpendicular to the rotational axis of the parent star, whereas hot Jupiter systems commonly demonstrate spin-orbit misalignment (Albrecht et al., 2013). It is expected that solar systems which have not experienced particular disturbance would exhibit orbital motion in a plane and direction aligned with the rotational axis of the star, having formed from a single rotating disk of gas and dust. Exceptions to this imply that the orbits of the planet or planets have been disturbed, likely by migration processes, and other planets that initially formed are likely to have been scattered out of the system or into the parent star during the migration of the surviving giant. Unlike other gas giants or rocky planets, there is no analogue of such planets within the Solar System, and as such they represent an entirely new and exciting class of object.

The majority of information about hot Jupiter planets is obtained from transit studies, which provide information on the mass and radius and thus the density of these unfamiliar objects. In addition, transmission spectra may be obtained as light from the parent star passes through the planet's atmosphere (see, e.g. Haswell, 2010, for a full discussion). This can provide some information on the types and concentrations of molecules in the atmosphere.

More recently, brightness temperature maps of HD 189733b, such as that shown in Figure 2.6, have been obtained (Knutson et al., 2007; Agol et al., 2010; Majeau et al., 2012). This is accomplished by measuring the subtle variations in the brightness of the

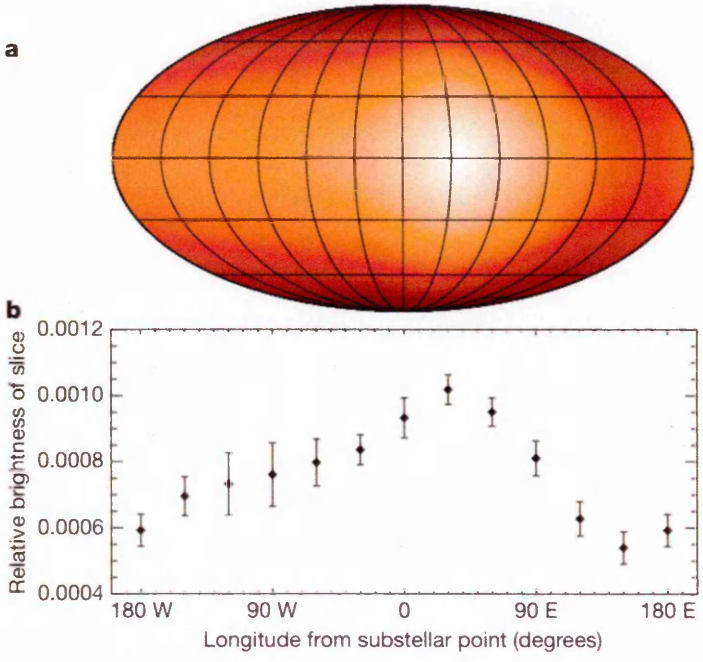

FIGURE 2.6. Taken from Fig. 3 of Knutson et al. (2007), **a** shows a brightness temperature map of HD 189733b, while **b** displays the data points from which the map was derived. The substellar point is located at (0,0).

system during the orbit, and in particular around the secondary eclipse. As the (tidally-locked) planet moves around its parent star, the total light reaching Earth from the system is the sum of the light from the star plus the light from the visible hemisphere of the planet. As different parts of the planet rotate in and out of view, the slight changes in overall brightness of the system can be measured and used to determine an average brightness temperature for longitudinal "slices" of the planet. In particular, the shape of the ingress and egress from the secondary eclipse, as the planet begins to be occluded or revealed by the star, provide information on the longitudinal brightness distribution of the star-facing hemisphere. It is notable that all such observations of HD 189733b have demonstrated a hotspot offset from the substellar point by around 30°, indicative of powerful equatorial winds.

A possible detection of winds on HD 209458b has also been made by Snellen et al. (2010), who observed the blueshift of carbon monoxide absorption lines in the planet's atmosphere. These measurements indicate winds of roughly 2 km s^{-1} at high altitudes, which agree with model predictions. However, the detail of such observations remains extremely limited due to the immense challenges in exoplanetary observation, leaving atmospheric models as the prime source of material for predicting the atmospheric conditions likely to prevail under such conditions.

There are many intriguing questions about the nature of hot Jupiter atmospheres. From studies of the chemical species likely to be present in these highly irradiated environments to investigations of the likely wind and temperature patterns and the prediction of possible observational signatures, all are to some extent interrelated. Atmospheric composition affects where stellar radiation is absorbed and reflected, and thus can affect one of the sources of energy that drive the motion of the atmosphere.

The modelling of large-scale atmospheric flows on exoplanets of all varieties is a rapidly expanding field of research. With regards to the specific area of hot Jupiter gas giants, many groups have conducted differing studies, using models of varying complexity and resolution. In particular, the well-observed planets HD 209458b and HD 189733b have been simulated in a variety of ways. Two-dimensional models permit greater horizontal or vertical resolution for a given amount of computing time, but at the cost of a dimension, often but not always the vertical. Many studies use the simple Newtonian cooling method as an approximation to the radiative transfer, but others include radiative transfer calculations of increasing complexity. Forcing in general, the periodic application of one or more adjustments to the modelled fields in order to force the atmosphere towards a specific state, typically reflecting influences not captured in the sphere directly covered by the model, is a complex subject, and the choice of suitable forcing is frequently at the judgement of the author of each individual study. Even the underlying equations governing the representation of atmospheric physics are model-dependent, with some models using the primitive equations as derived in Section 2.2.1, while others use alternate simplifications.

While some large-scale features (e.g. the appearance of a broad, superrotating - moving faster than would be possible were the atmosphere in solid-body rotation - jet at the equator) are agreed on by the majority of models, this is not always the case. Lacking direct observational data, as is readily available within the Solar System, exoplanetary modellers must rely on model results combined with clues teased from transit data, such as the brightness map of HD 189733b produced by Knutson et al. (2007), which finds a "hotspot" offset by approximately 30° from the sub-stellar point, or the Doppler shift detection of high-atmosphere ($0.01-0.1$ bar) winds on HD 209458b by Snellen et al. (2010).

The first three-dimensional atmospheric calculations in this area were performed for HD 209458b by Showman and Guillot (2002) as the second half of a study of both the atmospheres and interiors of hot Jupiters (part 1, Guillot and Showman (2002), is discussed further in Section 2.3) using the EPIC model, and found a strong (up to 1,500 m s^{-1}) superrotating equatorial jet, which offset the substellar hotspot eastward by around 60° longitude. This study was performed at a low resolution of 64 × 32 grid points horizontally, and 10 levels vertically between 100 and 0.01 bars, but the results have been robust to comparison with subsequent higher-resolution studies. Many other three-dimensional models find similar winds and offsets, such as the later work by Cooper and Showman (2005), which utilised a different model, the ARIES/GEOS Dynamical Core, and, relevantly, relied on the results of the radiative calculations of Iro et al. (2005) to inform the model conditions. Although the authors modelled the atmosphere down to 300 bar (ignoring the effects of the dissociation of molecular hydrogen at these depths), they noted that the winds drop swiftly to zero below approximately 30 bar. The hotspot was again found to be offset by approximately 60°, this time by an equatorial jet of up to 4,000 m s^{-1}, and the maximum wind speeds reached were over 9,000 m s^{-1}. Dependent on the location of the photosphere, the authors note that this hotspot could be more or less offset within their model by up to 20° in either direction.

In two dimensions, Cho et al. (2003) studied a shallow-water model of HD 209458b at T341 resolution, equivalent to a 1024 × 512 grid. They found moving temperature extrema near the poles due to strong polar vortices, rather than near the sub- and anti-stellar points, and westward rather than eastward equatorial flow, the latter of which is a common, though not necessary, feature of such two-dimensional models. Instead of the predictably offset hotspot of the three-dimensional models above, these vortices would revolve around the poles, causing distinctly different temperature observations to be made at the same time from orbit to orbit. A follow-up article by Menou et al. (2003) generalised these results to other, similar planets using the dimensionless Rossby and Burger numbers, predicting the existence of strong circumpolar vortices and few bands or jets as common features of hot Jupiter circulation. Langton and Laughlin (2007), also using a shallow-water model but with a radiative timescale 30× shorter than Cho et al. (2003), found as the most dominant feature a localised cold spot, offset eastward from the antistellar point by 60° – 70°, despite their westward equatorial jet. This

fixed feature was suggested to be due to their more rapid forcing, as with nil forcing they obtained the Cho et al. (2003) result. They additionally consider the possibility that HD 209458b is tilted through almost 90°: in this case, the planet is found to be warmer at the poles than the equator, with a periodic temperature variation and the warm face potentially marred by cool vortices that form at the poles and break as they move towards the equator.

Vertically, Burkert et al. (2005) carried out a two-dimensional study in this and the azimuthal dimension, neglecting latitude and the effects of curvature, and modelled an equatorial strip from the substellar to the antistellar point, using flux-limited diffusion for the radiation transfer. Since the perpendicular flow component is set to zero at each model boundary, it becomes impossible for this model to generate planet-encircling atmospheric flow as predicted by the simulations described above. The day-night temperature contrast was found to be sensitive to the atmospheric opacity, which strongly affected the depth of the heating experienced on the dayside: a low-opacity atmosphere permits the stellar irradiation to penetrate more deeply, allowing the heat deposited to be transported more efficiently.

From 2008 onwards, this hitherto small field began to expand rapidly.

Showman et al. (2008) simulate both HD 209458b and HD 189733b using the ARIES/GEOS dynamical core, a global, three-dimensional model run at 72×45 and 144×90 horizontal resolution, using 30-40 levels. Calculating a new set of temperatures and radiative time constants, they produce atmospheric circulation patterns similar to those found by other authors, and note that their models' lack of a stratosphere may cause part of their inability to fit some of the observed data points at certain wavelengths. Rauscher and Menou (2010) use the IGCM at T31 L33 to study HD 209458b between 1 mbar and 220 bar, with essentially the same setup as Cooper and Showman (2005) in order to compare the two results.

Cho et al. (2008) studied a broader range of gas giant parameters, using a single-layer equivalent barotropic model in isentropic coordinates, which permits higher horizontal resolution at the cost of the vertical dimension. To begin with, they tested the model on the Solar System's giant planets, at typical resolutions of T170. From this evaluation stage, the temperature is increased and the rotation rate decreased towards the final state of a tidally-locked planet on a 3.5 Earth day orbit, mimicking

HD 209458b. Winds of up to 1,000 m s^{-1} were again found, and, in common with the shallow-water model of Cho et al. (2003), a strong polar vortex. All such runs displayed in the paper were carried out at T106. Rauscher et al. (2008) use the same model to study the atmospheric dynamics of HD 209458b at T63 spectral resolution, while Langton and Laughlin (2008) study an eccentric hot Jupiter, HD 37605b, with a two-dimensional grid-based model integrating the primitive equations. Since the planet's orbit is eccentric, it is impossible for it to be fully synchronised. However, pseudo-synchronisation is assumed, in which the planet is approximately synchronised over the period of periastron passage. They find strong, stable circumpolar vortices, which migrate around the planetary poles. There is little comment on other circulation features.

Reviews such as those by Baraffe et al. (2010) or Seager and Deming (2010), cover much of the work in this field, although enough is being carried out that any one review will only be current for a short period of time. With a more tight focus, Watkins and Cho (2010) investigate the propagation of gravity waves on hot Jupiter exoplanets, using the example of HD 209458b, while Rauscher and Menou (2012b) study the role of drag mechanisms as a heat source in strongly forced atmospheres such as those of hot Jupiter planets.

Dobbs-Dixon and Lin (2008) model the atmosphere of hot Jupiters of varying rotation rate using a flux-limited radiative-hydrodynamical model between $\pm 70°$ and $1.06 - 1.2 R_J$, with a typical resolution having 60, 160, and 64 grid points in the radial, longitudinal, and latitudinal directions respectively. Showman et al. (2009) add non-grey[1], cloud-free radiative transfer to their GCM, the result of which they dub the SPARC/MITgcm (Substellar and Planetary Atmospheric Radiation and Circulation, with MITgcm as an acknowledgement of its progenitor model). They note that non-grey radiative transfer had not at the time of writing been carried out for any giant planet, extrasolar or otherwise. This model still uses the dynamical core of the MITgcm, and as such solves the primitive equations in gridpoint space, in this instance using the cubed-sphere grid rather than the standard latitude-longitude option. The resolutions studied are C16, C32, and C64, where CX refers to an X by X square on each side of the 'cube', and approximately correspond to latitude-longitude grids of

[1] "Grey" radiative transfer averages the opacity over all relevant wavelengths; non-grey calculations split the spectrum into multiple regions, each with an associated opacity, and calculate each separately.

64×32, 128×64, and 256×128 respectively. This cubed-sphere grid is shown in Figure 2.7. In different simulations, the top model layer is placed at 0.2 mbar or 2

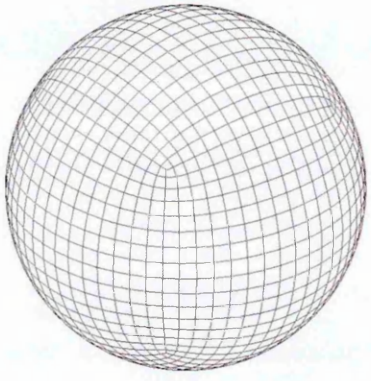

FIGURE 2.7. Example cubed-sphere grid at C16 resolution, taken from Fig. 2 of Showman et al. (2009).

μbar respectively, with 40 layers used in the first case and 53 in the second. They run various simulations of the two best-studied exoplanets, HD 209458b and HD 189733b, in both synchronous and asynchronous rotation. In common with previous studies without radiative transfer, they find in the synchronous cases a strongly superrotating equatorial jet between $\pm 30°$N, while the number and location of jets varies in the asynchronously rotating versions.

Work on transmission spectra includes that of Fortney et al. (2010), who calculate transmission spectra for both simple one-dimensional atmospheres, and complex three-dimensional atmospheres. Dobbs-Dixon et al. (2010) model the atmosphere of HD 209458b using the full three-dimensional compressible Navier-Stokes equations, coupled to a two-frequency flux-limited three-dimensional radiative model. Although they note that this form of the model cannot directly produce spectra, the resultant temperature-pressure profiles can be post-processed through the use of a one-dimensional radiative transfer code. Menou and Rauscher (2010) study radiation in the context of fast-moving atmospheric flows, suggesting that the standard radiative formalism used for Solar Systm planets is likely insufficient to model the powerful winds of hot Jupiters, and a more complex radiation-hydrodynamics treatment is more suitable. Dobbs-Dixon et al. (2012) use their radiative-hydrodynamical model to investigate the effect of jets on transit spectra. Other radiative transfer models include that of Rauscher and Menou (2012a), who add 'double-grey' radiative transfer to their previous model and study the new results. Additionally, Perna et al. (2012) use a three-dimensional circulation model

including dual-band radiative transfer to investigate the relation between irradiation temperature and the efficiency of heat redistribution.

Thrastarson and Cho (2010) study the effect of the initial flow setup on the final state, finding that there can be effects even under the application of strong (short-timescale) forcing. Thrastarson and Cho (2011) investigate the effects of model parameter choices and the physical significance, or lack thereof, of an arbitrary study's results. In particular, they find that a short thermal forcing time generally leads to large amounts of numerical noise, which must be damped by highly unphysical levels of dissipation.

2.2.2.1. *Intercomparison Studies.* Although intercomparison studies, tests in which multiple models are run on a prescribed test case and the outputs compared, are relatively common for Solar System planets, their appearance in exoplanetary modelling is more recent, and remains limited. Menou and Rauscher (2009) were the first to suggest a basic intercomparison test of the various models now used in the three-dimensional modelling of exoplanet atmospheres. They test their model, first in an Earth-like state on what is effectively a simpler version of the established benchmark of Held and Suarez (1994), then on a much-simplified setup designed to broadly resemble the properties of HD 209458b. They analyse the results thus obtained, and suggest the use of intercomparison studies in the circulation regimes of hot Jupiters, potentially based on that work. Heng et al. (2011) take this idea and expand upon it, generating further statistics and adding the comparison environment of a deep ($\geq$ 100 bar) model, in particular displaying temporal averages of both zonal mean wind and temperature for all cases.

2.3. Interiors of Gas Giants

2.3.1. Theory. The interior structure of gas giant planets may be modelled in a similar way as is often done for the structure of stars. Composed largely of hydrogen and helium, albeit with a potential small rocky core, they are in some respects similar to stars, though not massive enough to undergo nuclear fusion. One widely-used demarcation between planetary-mass and stellar-mass objects is at $13M_J$, above which limiting mass deuterium fusion is able to deplete the majority of the deuterium in the object's core (e.g. de Pater and Lissauer, 2007, p.476).

2.3.1.1. *Stars.* Stars begin their existence in the collapse of a cloud of interstellar gas, primarily composed of hydrogen and helium, with such little trace of heavier elements that those above helium are typically lumped together as "metals". Once the core has reached a sufficiently high temperature, nuclear fusion begins. Hydrogen is fused first, and dependent on the mass of the star, heavier elements may follow. The star's eventual fate likewise depends on its mass: a massive star above around $8M_\odot$ will end in a supernova, while less massive stars, after much longer lives, will end in a period of gravitational contraction. (Smith, 1995)

2.3.1.2. *Giant Planets.* In some respects, gas giant planets are similar to stars, and Jupiter itself has at times been dubbed a 'failed star'. Like stars, they are composed mainly of hydrogen and helium, but are not massive enough to ignite sustained fusion, and as such merely contract gravitationally throughout their lifetimes. Gas giants are typically assumed to have solid cores, although the mass of such a core is poorly constrained even for Solar System objects, and some studies have indicated that it may be possible for a core to "erode" away into the rest of the planet, as described by Wilson and Militzer (2012a).

2.3.2. Modelling Gas Giants. Interior structure models typically study the structure of the planet over its entire lifetime. The timescales involved are very different to those of atmospheric models, with each model timestep operating over thousands to millions of years. Extended equation of state tables are required compared to those used in stars, which do not typically reach the same low temperatures and pressures as a planetary model.

Many groups have modelled the interior structure of gas giant exoplanets, using a variety of codes. Guillot and Showman (2002) study the evolution of hot Jupiters

in conjunction with a further GCM study of their atmospheres in the final stage of evolution (Showman and Guillot, 2002). This joint study stands out as the majority of authors who study either atmospheric processes or planetary evolution rarely investigate both simultaneously. This discussion will focus only on the interior modelling side, as atmospheres have already been covered in Section 2.2.2.

A common issue to the evolutionary studies of hot Jupiter planets is the difficulty of reproducing the greatly inflated radius of some such planets. Additional energy sources have been suggested, though not all seem applicable to all cases. The energy added during tidal synchronisation is one possible source, providing additional heat in the interior during the circularisation stage of the planet's orbital evolution. The presence of planetary cores is a further factor, as in general a rocky core will contribute more, proportionally, to the mass of the planet for its volume compared to the majority hydrogen and helium constituents, resulting in a smaller planet for a given mass. Additionally, the matter of stellar irradiation must also be considered: hot Jupiters are in receipt of far more energy than any planet in the Solar System due to their proximity to their parent stars.

Tidal heating has been considered by many authors, with conflicting results. While some studies (e.g. Bodenheimer et al., 2001; Ibgui and Burrows, 2009) suggest that potentially the entire radius range of hot Jupiters may be explained by tidal heating, others indicate that other explanations must be sought. The work carried out by Leconte et al. (2010) studies tidal heating in particular detail, solving the tidal equations of Hut (1981) in full for systems of initial eccentricity $e \geq 0.2$ in particular, and demonstrating the distinct differences obtained between these solutions and those of studies conducted using the truncated tidal equations. In particular, at the higher eccentricities, the evolutionary paths can follow qualitatively distinct tracks depending on whether the truncated or full model is used, resulting in differing answers to the question of whether the inflated radii of hot Jupiters can be explained by tidal heating alone. While the full tidal model can explain the radii of some moderately bloated exoplanets, it cannot reproduce more extreme examples such as WASP-12b, requiring another source of energy.

The irradiation of the parent star is another suggested factor. However, it is likely that this energy will primarily be deposited in the upper atmosphere above a few tens of

bars, rather than directly reaching the deeper layers (see e.g. the discussion in Guillot and Showman, 2002; Showman and Guillot, 2002). If this energy is to penetrate deeper and affect the planetary evolution, it must be transferred in some other fashion, such as by atmospheric motions as suggested in Guillot and Showman (2002). Whether this is plausible depends on the depth to which atmospheric motions are affected by the upper layers. Burkert et al. (2005) use a two-dimensional (vertical-azimuthal) atmospheric model to investigate this and other effects of stellar irradiation, and find that insufficient energy is transported to deep within the atmosphere to explain the inflated radii of such planets within their model. They note, however, that their results are highly sensitive to the presence of grains in the model atmosphere, and do not account for full global circulation or factors such as the Coriolis force inducing latitudinal motion. Baraffe et al. (2010) and Fortney and Nettelmann (2010) indicate that this scenario is still under debate, with few studies investigating this effect in detail.

It has been found by Demory and Seager (2011) that, within their sample of Kepler planetary candidates, the measured radii appear independent of stellar flux below a limiting incident flux of approximately 2×10^8 erg s^{-1} cm^{-2}. They list several of the explanations that have been previously suggested to explain the anomalous radii of some hot Jupiters, and note that in light of the results, those most likely to be responsible for the inflation are those correlated to the strength of the incident stellar flux, probably in combination, with additional possibility for continuing tidal effects in the most close-in planets.

Further complicating matters is the issue of planetary migration: planets will probably not have formed as close to their stars as they are now observed, so will only have been subject to their current conditions for an unknown length of time. Specifically, gas giants are required to have accreted the majority of their material beyond the boundary within which temperatures in the initial protoplanetary disk are too high for the lighter elements to deposit into grains: the system's "snow line". A planetary embryo that forms inside the snow line is expected to be unable to accumulate the mass of lighter elements required to form a gas giant, and absent other influences, will become a rocky planet such as Earth or Mars. Only outside the snow line are sufficient quantities of light elements available for capture by a protoplanet to allow it to accrete into a gas giant. The gas giants observed to orbit within their system's predicted snow

line must then have migrated inwards during their evolution to reach their current positions, and may continue migrating to the point of destruction by the parent star, as described by, e.g., Davis and Wheatley (2009). Migration may result from several factors, such as the interaction between a young planet and the surrounding protoplanetary disk, or the interaction between multiple planets in the same system (such as the hypothesised former 2:1 mean motion resonance between Jupiter and Saturn). Massive planets in a protoplanetary disk may undergo what is termed Type II migration: as the increasingly massive planet clears a gap in the disk in the region of its orbit, its motion may become coupled to the viscous evolution of the disk. A large planet may also experience a phase of Type III or runaway migration. Planets that enter mean motion resonances with one another may accelerate the mutual rate of migration, or reverse it, or even eject one or more of the planets either out of the system or into the parent star. A recent review on the subject was carried out by Kley and Nelson (2012).

CHAPTER 3

Atmospheric Modelling

This chapter covers the area of standalone atmospheric modelling, without interior model input. As discussed in Chapter 2, Section 2.2, a wide variety of atmospheric modelling techniques have historically been used to study the atmospheres of Solar System bodies, and their use is now expanding to the approximation of likely conditions in the atmospheres of exoplanets. While the available population of known exoplanets displays a wide variation of conditions, this work focuses on the modelling of hot Jupiters.

Predicting the atmospheric circulation of such a foreign planetary environment as a gas giant less than 0.1 AU from its parent star is a challenging yet ultimately rewarding task, providing opportunities for both extending our understanding and providing observational advice. These planets serve as a unique testbed for the degree to which our models may accurately represent reality. Further, such modelling may be used to guide future observations: if the models predict detectable effects, or on the contrary a lack of effects detectable with current instrumentation, precious observing time may be assigned accordingly to gain the optimum scientific benefit.

To study the large-scale circulation of atmospheres, general circulation models have been developed and used for many years, from predicting the weather on Earth to modelling the circulation patterns on planets as distinct as Mars, Venus, and Jupiter. The extension of such models to exoplanetary work is a natural consideration, and a first step towards predicting the conditions that might one day be observed in a future era, and that shape the observations that can be made today.

Typically, only a few gross factors will be known for a transiting exoplanet. Its mass may be determined using the radial velocity technique (see discussion in Chapter 2, Section 2.1.1.2), and since transiting planets must have orbital planes approximately edge-on to the line of sight, $m_P \sin(i) \approx m_P$. The irradiation flux can be calculated using the planet's size and orbital distance, which may be determined from the orbital

period, combined with stellar type. The planetary radius calculated may also be calculated from the properties of the transit light curve, permitting further calculation of the average density and placing a rough restriction on the composition. This limited amount of information invites curiosity, particularly in the case of planets such as hot Jupiters that have no Solar System analogue. The region of parameter space occupied by hot Jupiters had not hitherto been explored, as such close-in giant planets appeared to defy the expectations of models of solar system formation. (Boss, 1995)

Already, measurements have been made that begin to shed light on some global-scale features of distant hot Jupiters. Some well-studied planets have proven amenable to transmission spectroscopy of their upper atmospheres, permitting molecular detections. However, a full atmospheric composition remains as yet beyond reach. Knutson et al. (2007) studied the lightcurve of HD189733 during half an orbit of its planet, and used this to gain an approximate large-scale temperature map of the planet, as discussed in Chapter 2. Although this map was latitudinally averaged and divided into only twelve longitudinal slices, the resolution was sufficient to detect an offset in the "hot spot" from the substellar point, a pattern predicted by atmospheric modelling. Snellen et al. (2010) carried out detailed measurements of the Doppler shift in the carbon monoxide absorption lines in the atmosphere of the planet HD209458b. After the shift due to the motion of the planet and star about their common centre of mass were subtracted, a residual blueshift was observed, indicating the motion of high-altitude winds in the planet's upper atmosphere. This effect, too, has been produced in atmospheric models, and provides a constraint against which to test the predictions of such models.

These relatively few constraints poorly inform the parameter space available to even a simple model. Complex atmospheric models are almost entirely unconstrained by the available information. In this situation, it is advisable to use the simplest form of model that is able to reproduce the gross physical processes. PUMA is such a model, incorporating only parametrisations of the most major factors governing the atmospheric flow.

In this chapter, the simple, freely available GCM PUMA is introduced and explained (Section 3.1), and giant planet experiments carried out to investigate the response of the model atmosphere to various likely scenarios. An intercomparison study is performed

in order to determine the degree of agreement or disagreement between PUMA and similar models also used to approximate close-in gas giant planets. Properties of the intercomparison 'standard' planet are then varied one at a time to investigate the effect of the changes thus made.

3.1. PUMA

PUMA is a three-dimensional global climate model (GCM) developed at the University of Hamburg (Fraedrich et al., 2005). It is a hydrostatic, shallow atmosphere model utilising the standard primitive equations of meteorology as previously described in Chapter 2, Section 2.2. For the purposes of modelling, the equations are reformulated in terms of vorticity ($\zeta = \nabla \times \mathbf{u}$) and divergence ($D = \nabla \cdot \mathbf{u}$). The vertical coordinate σ is defined in terms of pressure, rather than height: $\sigma = P/P_s$, resulting in a terrain-following (for those planets with terrain) coordinate system with $\sigma = 1$ at the bottom of the atmosphere and $\sigma = 0$ at the top. Model fields are represented horizontally in terms of the spherical harmonics Y_n^m, where n is the total wavenumber and m the zonal wavenumber, and the model resolution thus determined by the highest wavenumber represented in a given run. The triangular truncation $|m| \leq n$ is used, and each resolution is denoted by T[$n_{\max}$]: T21, for example, has maximum wavenumber $n = 21$.

In the non-dimensionalised vorticity, divergence, and sigma form, as used by the model, the primitive equations become

$$\frac{\partial}{\partial t}(\zeta + f) = \frac{1}{1-\mu^2}\frac{\partial F_v}{\partial \lambda} - \frac{\partial F_u}{\partial \mu} + P_\zeta \tag{3.1.1}$$

$$\frac{\partial D}{\partial t} = \frac{1}{1-\mu^2}\frac{\partial F_u}{\partial \lambda} + \frac{\partial F_v}{\partial \mu} - \nabla^2\left(\frac{U^2+V^2}{2(1-\mu^2)} + \Phi + T_0 \ln(p_s)\right) + P_D \tag{3.1.2}$$

$$\frac{\partial \Phi}{\partial \ln(\sigma)} = -T \tag{3.1.3}$$

$$\frac{\partial}{\partial t}\ln(p_s) = -\int_0^1 D + \mathbf{u}\cdot\nabla \ln(p_s)\, \mathrm{d}\sigma \tag{3.1.4}$$

$$\frac{\partial T'}{\partial T} = -\frac{1}{1-\mu^2}\frac{\partial (UT')}{\partial \lambda} - \frac{\partial (VT')}{\partial \mu} + DT' - \dot{\sigma}\frac{\partial T}{\partial \sigma} + \kappa\frac{T}{p}\omega + \frac{J}{c_p} + P_T \tag{3.1.5}$$

where $f = 2\Omega\sin(\phi)$ is the Coriolis parameter, Ω being the planetary rotation rate and ϕ being the latitude, $\mu = \sin(\phi)$, and λ is the longitude. U and V are related to the horizontal wind components $\mathbf{u} = (u, v)$ by $U = u\cos(\phi)$, $V = v\cos(\phi)$. Φ is the geopotential, and T the temperature, with $T' = T - T_0$ the temperature deviation from reference temperature T_0. p_s is here the surface pressure and p the pressure, and $\kappa = R/c_P$ where R is the specific gas constant and c_P the heat capacity at constant

pressure. J is the diabatic heating rate, and F_u and F_v are given by

$$F_u = V(\zeta + f) - \dot{\sigma}\frac{\partial U}{\partial \sigma} - T'\frac{\partial}{\partial \lambda}(\ln(p_s))$$
$$F_v = -U(\zeta + f) - \dot{\sigma}\frac{\partial V}{\partial \sigma} - T'(1-\mu^2)\frac{\partial}{\partial \mu}(\ln(p_s))$$

Lastly, the terms P_ζ, P_D, and $J/c_p + P_T$ represent in each equation the model parametrisations of friction, heating, and the hyperdiffusion, each of which is discussed in more detail below. They have the following forms:

$$P_\zeta = \frac{\zeta}{\tau_F} + H_\zeta \tag{3.1.6}$$
$$P_D = \frac{D}{\tau_F} + H_D \tag{3.1.7}$$
$$\frac{J}{c_p} + P_T = \frac{T_R - T}{\tau_R} + H_T \tag{3.1.8}$$

The H terms represent the hyperdiffusion, discussed below. T_R is the restoration temperature, towards which the model relaxes with timescale τ_R, and τ_F is the frictional timescale. Each timescale may be set to a unique value for each model level.

Equations 3.1.1 and 3.1.2 are the vorticity and divergence representations of the momentum equation, respectively. Equation 3.1.3 is the hydrostatic equilibrium approximation. The continuity equation becomes Equation 3.1.4, and the thermodynamic equation is Equation 3.1.5. Each of these equations is non-dimensionalised by dividing The four prognostic equations used in the calculation for each timestep are Equations 3.1.1, 3.1.2, 3.1.4, and 3.1.5: these . In each timestep, the model performs Legendre and fast Fourier transformations to convert the fields into gridpoint representation, where the non-linear tendencies are applied; it then reverses the procedure, converting back into spectral space in order to perform the time step. A finite-difference scheme is used in the vertical. The vorticity, divergence, temperature, pressure, and time are non-dimensionalised by scaling them by the appropriate planetary parameters, as described by Fraedrich et al. (2007). Every n timesteps, where n is a value input to the model at the beginning of the run, the prognostic variables are written to an output file in re-dimensionalised spectral form, from which they can be processed by the post-processor Pumaburner to produce NetCDF or GrADS files of both these and derived quantities in grid point space for further manipulation or plotting.

PUMA was originally designed to model Earth, and has also been successfully used on other Solar System objects (e.g. Grieger et al., 2004). Over the course of this project, it has been modified for use on gas giants, in particular "hot Jupiters", which are expected to be tidally locked and thus have very specific and intense patterns of energy input, with all the inward radiation flux entering from one side of the planet. Tidal locking is a phenomenon in which the planet's rotation has become synchronised so that it completes one rotation in the time taken to complete one orbit, always presenting the same face to the star; the Moon, as a Solar System example, is tidally locked to the Earth. One side of the planet will then be extremely hot due to the permanent irradiation from the nearby (< 0.1 AU) star, while the other, facing into deep space, is cooler. PUMA utilises Newtonian cooling as a simple approximation of the processes of radiative heating and cooling. At every model timestep, the three-dimensional temperature field produced is adjusted by the temperature part of the parametrisation term P_T on timescale τ_R towards a predefined restoration state: a static temperature field T_R determined at the start of the run. This field is typically determined internally as a function of latitude and height, and in order to replicate the type of forcing expected for a "hot Jupiter" world, it was modified to accept as input a fully three-dimensional temperature field defined externally to the model. These fields are created prior to each run with parameters suited to the model resolution and the planetary configuration under study. If the field resolution is incorrectly specified, PUMA is programmed to throw an error and automatically stop, preventing the inadvertent misapplication of inapplicable temperature fields.

Friction is implemented in the simple form of Rayleigh friction applied in the vorticity and divergence equations, with timescale τ_F. Rayleigh friction is the simplest possible parametrisation of boundary layer drag, and, for an Earth model, is typically defined with a timescale on the order of ≈ 1 day at the lowest level, decreasing with increasing altitude. (James, 1994) Its timescale can be individually defined at each model level, allowing it to be customised to the experimental conditions.

A consequence of the model's efficient energy conservation is that energy that is initially generated at large scales tends to build up at high wavenumber (small scales), since it cannot be directly lost. In the real world, such energy cascades to ever smaller scales until it is lost in turbulence, but global atmospheric models have insufficient

resolution to reach these scales and must mimic its effects artificially. This energy is dissipated by employing a hyper-diffusion term in the equations for vorticity, divergence, and temperature. The strength of the hyper-diffusion is not well constrained by any physical parameters, and must be manually adjusted to the problem at hand. Thrastarson and Cho (2011) discuss in detail the problems with this factor, noting in particular that the short relaxation timescales frequently used in such studies often result in the use of high levels of dissipation in order to prevent model breakdown, which in turn may lead to areas of the simulation being over-damped. One way of investigating whether a simulation is over- or under-damped is to study the kinetic energy spectrum. In the over-damped case, the decrease in kinetic energy at high wavenumber (an example of which may be seen in Section 3.2.1.2, Figure 3.15) would continue to affect all wavenumbers, with less energy available at even the largest (low-wavenumber) scales. By contrast, an under-damped run would result in the high-wavenumber end of the spectrum flattening out instead of tailing off, where energy cascading to the small scale is blocked from going any further by the resolution limit and simply builds up.

PUMA is also particularly resilient to computational errors, to the extent that the model will continue to perform computations, albeit slowly, even while recording key variables as "NaN": not a number. Additional checks were therefore implemented in the code to detect model 'blow-up' beginning (as evidenced by global RMS values suddenly climbing by orders of magnitude) and halt the run.

By the limitations of the code alone, the atmosphere may cover any range of pressures; in principle, however, it is only valid as far as the shallow atmosphere approximation holds. (See discussion in Chapter 2, Section 2.2.1) While it is computationally possible to run the model outside this region of parameter space, the results will be physically meaningless due to the falsity of one of the key assumptions underpinning the model's construction.

3.2. Experiments

Atmospheric modelling experiments were carried out with PUMA, first to ensure the model performs as expected, then to model extrasolar planets. Early testing ensured that the modified model (as detailed in Section 3.1) still performs adequately when Earthlike parameters are entered, ensuring that code changes had not introduced unexpected and unphysical behaviour. Following this successful test, PUMA was then run with an externally supplied series of parameters in order to test its precise response against that of other models used in the field: an intercomparison test. The 'standard' planet provided by the intercomparison was then altered to investigate the effects of changing the rotation rate, both by increasing and decreasing it.

3.2.1. Hot Jupiter Intercomparison. Despite the many modelling studies of hot Jupiter planets (see discussion in Section 2.2), the growing field of exoplanetary atmospheric modelling has seen little work on standardised benchmark tests for its models, limiting understanding of the dependence of results on specific models and conditions. With spatially resolved observations as yet difficult to obtain, rendering it impossible to check model results against the conditions on existing planets, such a test is invaluable. To date, intercomparison work for hot Jupiter scenarios has been carried out by Menou and Rauscher (2009); Heng et al. (2011). Without such studies, it cannot be determined which elements of a given simulation are likely to correspond to conditions on the planet under study, and which are simply likely to be only artefacts of a specific model or set of conditions.

Intercomparison studies are routine in the more mature field of Earth-based atmospheric modelling, with the "dynamical core" tests that are suitable for the more simple exoplanetary models based on the work carried out by Held and Suarez (1994). Such a study defines the model parameters and resolutions to be used, including variables normally dictated by the experimenter, fixing as many conditions as possible in order to ensure that any variation in results is due primarily to the models themselves. Atmospheric models are complex and highly non-linear, and are often extremely sensitive to the input parameters and initial conditions given them. While variability is always to be expected, the wide spread of results even for similar cases further illustrates the importance of having fully-specified test case simulations from which differing model-dependent responses may be determined and analysed.

Although an intercomparison test for models of tidally locked gas giant planets has previously been suggested and carried out, the data provided were limited in terms of comparability. For example, the studies to date have been performed using primarily "snapshots": images of a model field at a single time. Even using the same model and conditions, it is unreasonable to expect any two such snapshots to look precisely identical between simulations. In addition to the random noise typically seeded at model initialisation, as the run continues for longer periods of time, minute differences in the way that the programs store and handle numbers will result in differences that are magnified over time, resulting in potentially quite different "snapshots" at any given timestep. While snapshot images are useful in many situations, for comparison purposes it is preferable to produce mean and standard deviation plots, which depict at a glance both the overall state and the variability of the flow (see, for example, Figure 3.3).

Here, the PUMA model is subjected to the intercomparison test defined by Heng et al. (2011) and detailed statistics produced to facilitate comparison, with both time means and the associated standard deviations displayed, removing the time dependence and providing a measure of the variability. Model runs have been analysed to determine the variability between resolutions, and the effect of resolution on the energy spectra studied. Superrotation is a robust and reproducible feature at all resolutions.

3.2.1.1. *Model Parameters.* In order to prepare a hot Jupiter planetary model with PUMA, the properties of the planet and its atmosphere must be specified. Some, such as the planetary radius, may be set to values acquired by observation, but others must be extrapolated from estimated conditions. The "surface" pressure is somewhat unique among these variables, as, for a gas giant, it is chosen so as to set a viable lower boundary for the model, and may be placed in any location for which the model assumptions are valid. For this study, it is located at a pressure of 1 bar.

The precise planetary parameters used to conduct this investigation are listed in Table 3.1, and were chosen by Menou and Rauscher (2009) to approximate values appropriate to HD 209458b. The model resolutions utilised, and their approximate equivalent grid spacings, are given in Table 3.2.

The temperature restoration field is a parameter of primary importance, and its form poorly constrained. Many variations on this crucial element of the model forcing

Parameter	Symbol	Value
Planetary radius / m	a	10^8
Rotation rate / 10^{-5} rad s^{-1}	Ω	2.1
Gravity / m s^{-2}	g_p	8.0
'Surface' pressure / bar	P_0	1.0
'Surface' temperature / K	T_surf	1600
Equator-pole temperature difference / K	ΔT_EP	300
Tropopause temperature increment / K	δT_stra	10
Tropopause height / 10^6 m	z_stra	2
Adiabatic lapse rate / 10^{-4} K m^{-1}	Γ_trop	2
Specific gas constant / J kg^{-1} K^{-1}	R_s	3779
Heat capacity / J kg^{-1} K^{-1}	c_p	13226.5

TABLE 3.1. Table of planetary parameters for the intercomparison study. Note that this rotation rate Ω corresponds to a planetary "day" of approximately 3.5 Earth days.

Abbreviation	Max Wavenumber	Levels	Equivalent Grid	Max Spacing / km
T42L15	42	15	128×64	4,910
T63L20	63	20	192×96	3,270
T85L20	85	20	256×128	2,450

TABLE 3.2. Table of abbreviations for the model resolutions utilised, together with approximate values for equivalent grid spacings for a planet of the radius studied, 10^8 m. T-numbers indicate the highest wavenumber stored in the triangular truncation; L denotes the number of levels in the vertical.

may be justified on physical principles, and suitable temperature distributions must be chosen with care. A simple distribution with high temperatures at the substellar point giving way smoothly to lower temperatures at the antistellar point and a maximum temperature difference diminishing with altitude is here chosen for correspondence with the previous intercomparison studies: following Menou and Rauscher (2009), the temperature restoration field is set up as defined by the equation

$$T_\mathrm{eq}(\lambda, \phi, \sigma) = T_\mathrm{eq}^\mathrm{vert}(\sigma) + \beta_\mathrm{trop}(\sigma) \Delta T_\theta(\lambda, \phi) \tag{3.2.1}$$

where

$$T_\mathrm{eq}^\mathrm{vert}(z) = T_\mathrm{surf} - \Gamma_\mathrm{trop} \left(z_\mathrm{stra} + \frac{z - z_\mathrm{stra}}{2} \right) + \sqrt{\left(\frac{1}{2} \Gamma_\mathrm{trop} [z - z_\mathrm{stra}] \right)^2 + \delta T_\mathrm{stra}{}^2} \tag{3.2.2}$$

$$\beta_\mathrm{trop}(\sigma) = \begin{cases} \sin\left(\frac{\pi}{2} (\sigma - \sigma_\mathrm{stra}) / (1 - \sigma_\mathrm{stra}) \right) & \sigma \geq \sigma_\mathrm{stra} \\ 0 & \sigma < \sigma_\mathrm{stra} \end{cases} \tag{3.2.3}$$

and

$$\Delta T_\theta(\lambda, \phi) = \cos(\lambda) \cos(\phi) \Delta T_\mathrm{EP} \tag{3.2.4}$$

T_{eq} represents the temperature produced by radiative-convective equilibrium, without winds or other factors: the purely vertical part of this structure is represented by $T_{\text{eq}}^{\text{vert}}$ and the purely horizontal part by ΔT_θ. The vertical element of the profile was chosen by Menou and Rauscher (2009) to match that calculated by Iro et al. (2005) for HD 209458b. Such radiative-convective equilibrium temperatures may also be computed analytically from first principles using models such as that of Guillot (2010), whose work has been extended to include the effects of scattering by Heng et al. (2012). A scaling factor β_{trop} is applied to steadily decrease the temperature difference between the dayside and nightside until it becomes zero above the tropopause, represented by σ_{stra} and z_{stra}. This results in a maximum temperature difference at the bottom of the model of $2\Delta T_{\text{EP}}$, or 600 K, from the substellar point to the antistellar point, which decreases with altitude until the horizontal part of the forcing profile is uniform at the tropopause. Similarly, the temperature increment at the tropopause is given by δT_{stra} (Menou and Rauscher, 2009). The dry adiabatic lapse rate is represented by Γ_{trop}, and the mean 'surface' temperature (temperature at the base of the model atmosphere) by T_{surf}, with the equator-to-pole temperature difference denoted by ΔT_{EP}. The base of the model atmosphere, P_0, is here defined at 1.0 bars (see Table 3.1), consistent with that used by Menou and Rauscher (2009). λ and ϕ are the longitude and latitude coordinates, respectively, and the σ-coordinate, which has a long history in atmospheric modelling due to the simplicity it engenders, is used throughout: $\sigma = P/P_s$, where P is the pressure and P_s the surface pressure. Levels spaced linearly in sigma are thus also linearly spaced in pressure, and therefore approximately exponentially spaced in height (pseudoheight $z = -H \ln(P/P_0)$, where H is the pressure scale height).

This setup produces temperature fields as shown in Figure 3.1, which shows the temperature forcing at a single sigma level, demonstrating the dayside hotspot and, with this forcing, nightside cold spot, and Figure 3.2, which demonstrates the longitudinally averaged, or "zonal mean", vertical profile.

3.2.1.2. *Results.* PUMA was set up according to the parameters specified in Section 3.2.1.1, and run for a total of 380 model days at each of the resolutions T42L15, T63L20, and T85L20 (see Table 3.2). In the results that follow, all time means are taken over the 350-day model period covering days 30-380. Throughout this section, the term "day" refers to planetary sidereal days (length approximately 3.5 Earth days) unless

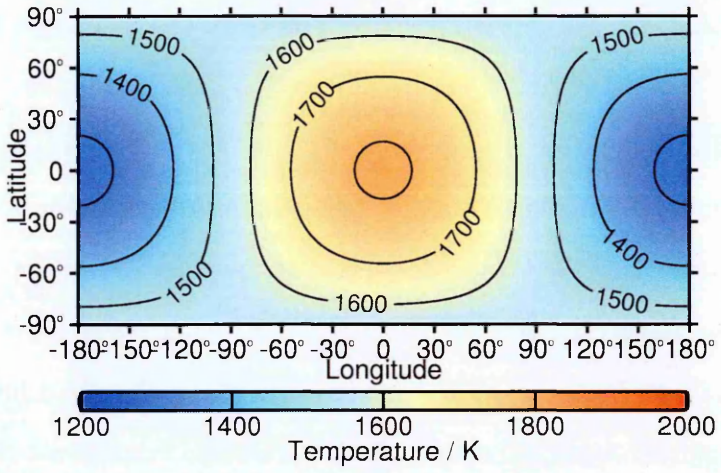

FIGURE 3.1. Thermal forcing profile in latitude and longitude at $\sigma = 0.7$, equivalent to a pressure of 0.7 bars. The substellar point is located at the centre of the image, (0,0). It may be noted that this forcing profile results in a "cold spot" on the nightside of equal magnitude to the dayside "hotspot".

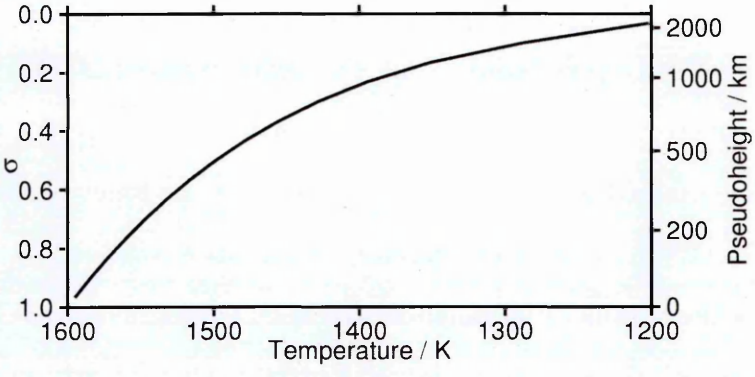

FIGURE 3.2. Zonal mean thermal forcing profile. The longitudinal averaging causes the day-night temperature differences to cancel out, resulting in the averaged value being everywhere the same for a given value of σ.

explicitly stated otherwise. The run length of 350 days was chosen to correspond to the study by Heng et al. (2011), encompassing sufficient time to gain an understanding of the nature of the flow while balancing the limitations of computation time. The initial 30 days are considered a spinup period, allowing the model to settle into an equilibrium state following initialisation to avoid spurious signals in the results: close study of the model statistics global root mean square vorticity and global root mean square divergence indicates that, under these conditions, PUMA reaches a stable state in 30 model days or fewer. See Figure 3.14 for an example plot of these statistics.

In the following discussion, the atmospheric properties investigated are shown as two-dimensional plots in the form of either a slice through the atmosphere at a specified sigma level, or a longitudinally averaged vertical and latitudinal plot. Contours in the temperature plots represent standard deviation, while in other cases, they follow the values of the displayed field. Where vectors are shown, they denote wind strength and direction. All line graphs denote either local values or global model statistics.

Figure 3.3 shows the time mean temperature fields and associated standard deviation contours for runs of varying resolution, on the sigma level closest to $\sigma = 0.7$. This value was chosen to conform with the other intercomparison tests for hot Jupiters previously performed in the literature (Menou and Rauscher, 2009; Heng et al., 2011), and demonstrates a visually distinctive pattern of atmospheric flow. Due to the linear level spacing, only the T42L15 run had a level at precisely this sigma value, with the 20-level runs having their nearest level at $\sigma = 0.725$. The comparison between the T42 and other runs is therefore not as direct as that between T63 and T85, which are taken on the same level in the atmosphere. The magnitudes of mean temperature and standard deviation are both approximately consistent between runs, increasing slightly with increased resolution, showing good agreement between all runs on the final mean temperature values. The standard deviation increases overall with the resolution of the run, the higher resolution runs demonstrating higher variability. In particular, it may be noted that the 15K standard deviation contour towards the poles is absent from the T85L20 run. The maximum mean temperature is 1698 K at T42, 1705 K at T63, and 1709 K at T85, with corresponding maximum standard deviations of 67 K, 64 K, and 66 K respectively.

Studying these plots together with the information contained in the zonal mean zonal wind plots of Figure 3.8, it becomes clear how the temporally-averaged chevron patterns of temperature are produced. Between approximately $\pm 30°$ latitude, the strong eastward wind advects warm air from the hotspot to the east and into the nightside (beyond $\pm 90°$ longitude), producing the tip of the chevron, while outside this latitude band, the weaker westward winds draw warm air in the other direction, generating the offset from $0°$ longitude seen in the two lobes.

The greatest variance is found in two equatorially symmetric regions centred on approximately $\pm 30°$ N and $100°$ E of the substellar point (0,0), where the strong

equatorial jet (a powerful, high-velocity wind at the equator: the strong, relatively localised eastward wind on average occurring between ±30° latitude shown in Figure 3.8) has carried warm air past the terminator to the cool nightside, rendering the temperature contrast much greater and so making its north-south fluctuations most apparent. The simple chevron pattern shown by the average temperature field is on a state of constant flux from timestep to timestep, as demonstrated by the "snapshot" temperature plots shown in Figure 3.4. These display a weaving behaviour governed primarily by the motion of the equatorial jet, which displays peak zonally averaged windspeeds of up to 1,200 ms^{-1}.

"Snapshot" plots at T42L15 corresponding to those in Figure 3 of Menou and Rauscher (2009), and to the top row of Figure 6 of Heng et al. (2011) are shown in Figure 3.4. Here, the temperature is displayed in colour, and the horizontal wind velocity as vectors. The same general features can be seen, with a strong equatorial jet and weaker reverse flow beyond ±30° N. Although the winds appear similar in distribution and proportion, Menou and Rauscher (2009) do not provide a vector scale, requiring reference to be taken from Figure 3.5 and compared to Figure 4 of that paper, which displays a snapshot of zonal mean zonal wind.

A snapshot of the T42L15 zonal mean zonal wind is shown in Figure 3.5, for comparison with Figure 4 of Menou and Rauscher (2009). It can be seen that the maximum and minimum zonally averaged wind speeds are similar, with the winds of Menou and Rauscher (2009) peaking at 1,264 ms^{-1} in the direction of positive longitude and at -768 in the reverse flow. However, there are once again distinct differences in configuration, such as the return flow being strongest in the northern hemisphere rather than the southern. Without time-averaged plots for comparison, it cannot be determined whether this is an artefact of the snapshots or a persistent difference in the results.

While the mean state of the model is robust, replicable from run to run, the precise state at any given moment is not, and somewhat different temperature distributions and forms for the equatorial jet may be observed even at the same moment in identically started runs. This is due to the high non-linearity of the model and the resulting sensitivity of its evolution. Although snapshot plots are intuitively informative and provide an instant impression of the atmospheric condition, they are thus of only limited use in the standardised comparisons required of an intercomparison test. It

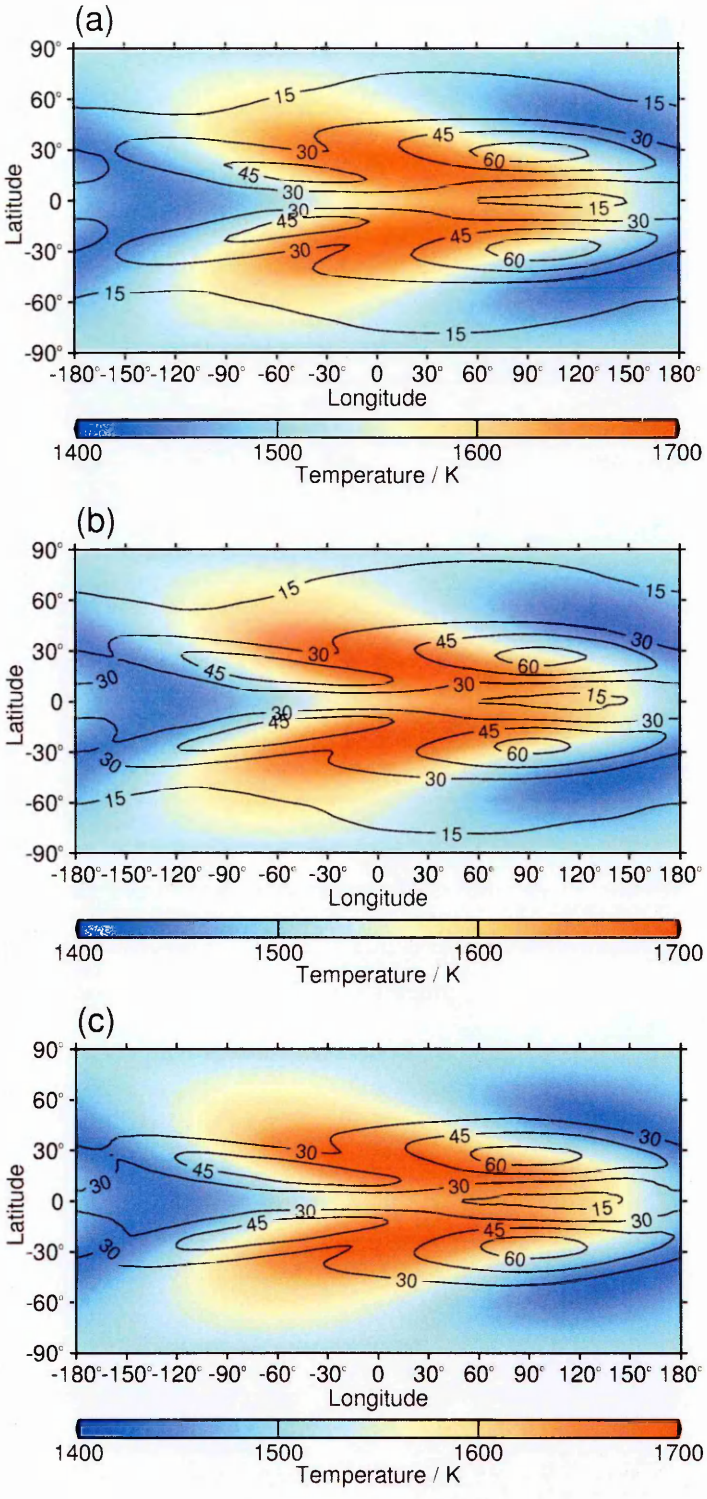

FIGURE 3.3. Temporally averaged plots of mean temperature overlaid with standard deviation contours in Kelvin. The substellar point is at (0,0). (a) T42L15 at $\sigma = 0.7$, (b) T63L20 at $\sigma = 0.725$, (c) T85L20 at $\sigma = 0.725$.

also cannot be guaranteed that any one snapshot was not taken during an unusual state of the flow, and may not be accurately representative of the typical state.

The time-averaged zonal mean temperature fields and their associated standard deviation contours are shown in Figure 3.6. It should be noted that the temperature

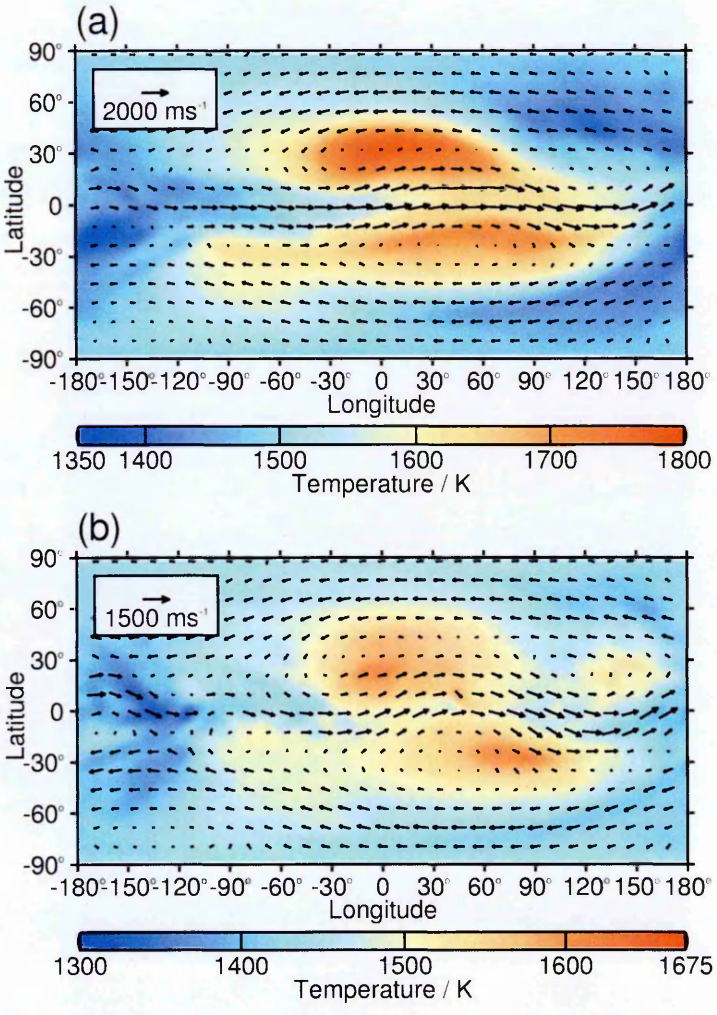

FIGURE 3.4. "Snapshot" of temperature overlaid with wind vectors at (a) $\sigma = 0.7$, (b) $\sigma = 0.37$. Produced for comparison with Figure 3 of Menou and Rauscher (2009), they show distinct similarity in nature, but differing features, as expected.

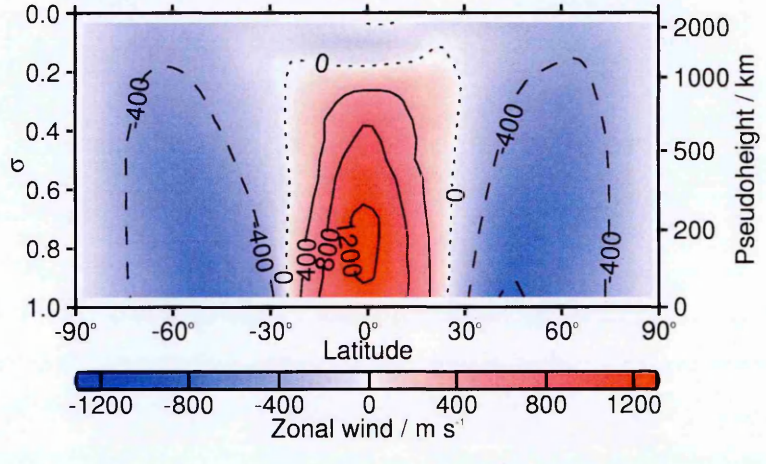

FIGURE 3.5. "Snapshot" of zonal mean zonal wind strength, with contours. Red shading and solid contours indicate wind directed towards positive longitude (towards the reader); blue shading and dashed contours the reverse. Produced for comparison with Figure 4 of Menou and Rauscher (2009), it again shows overall similarity with differing features.

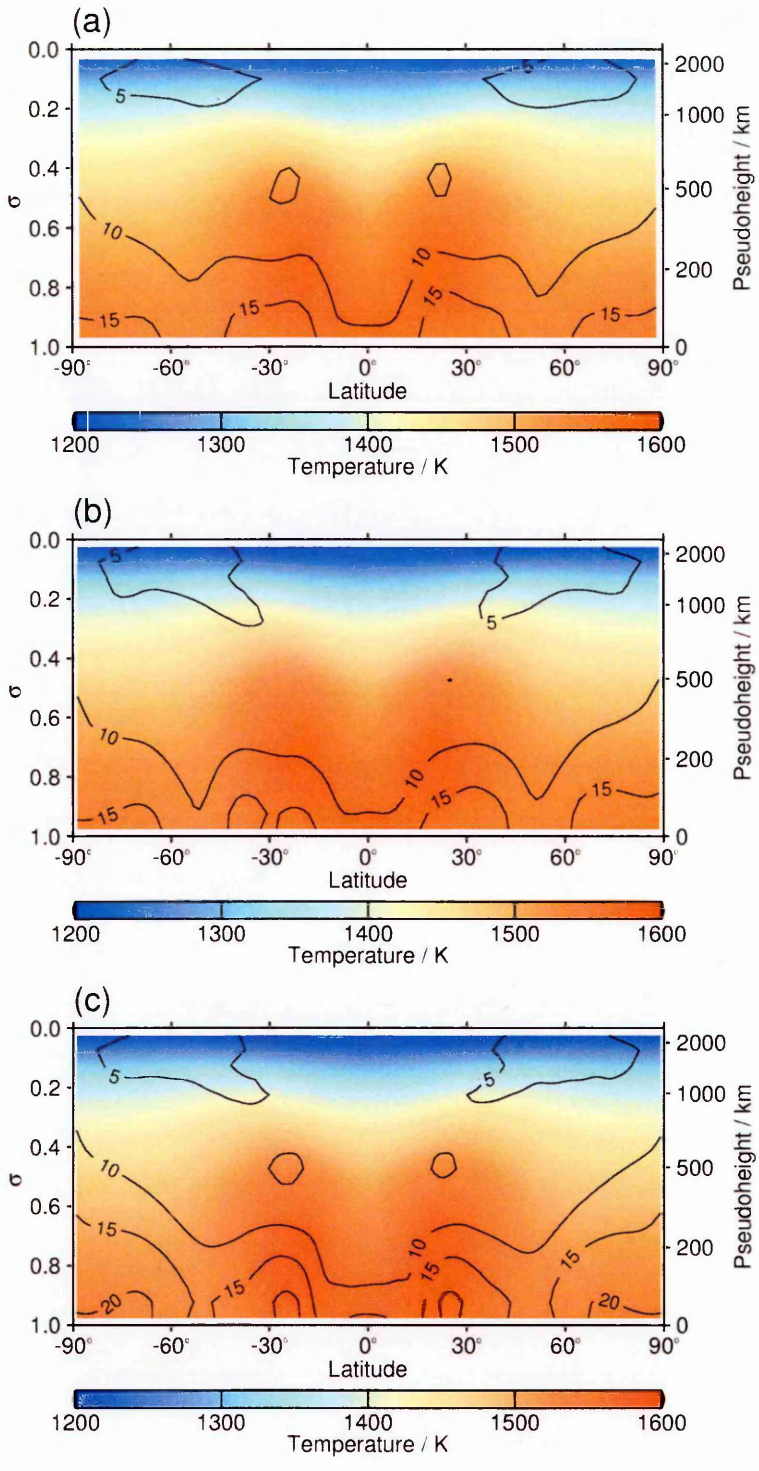

FIGURE 3.6. Time-averaged zonal mean temperature plots at the differing resolutions. Colour denotes temperature; contours denote standard deviation in Kelvin. (a) T42L15, (b) T63L20, (c) T85L20.

scale is substantially different to that of the time-averaged temperatures in Figure 3.3, due to the different range encompassed. The most notable departure from the simple vertical profile of the forcing state (Figure 3.2) is the appearance of two "hotspots" between $\pm 40°$ N and corresponding in location to the temperature peaks observed in Figure 3.3. These plots demonstrate the greatest difference in standard deviation between runs, with the location of the contours differing noticeably, particularly at the

top and bottom of the model domain. To some extent, this may be due to the limited vertical resolution of the runs. Towards the poles and below approximately $\sigma = 0.6$, all runs are distinctly cooler than those of Heng et al. (2011) figure 6, which show temperatures in these regions of almost equal magnitude to those at the equator.

By subtracting the time mean temperature field from the known forcing state and dividing through by the restoration timescale, plots of the heating rate resulting from the forcing may also be derived for each run, shown in Figure 3.7. This figure demonstrates clearly that net cooling is experienced in the equatorially symmetric regions between 0° and ±45° N, while net heating is experienced in the poleward regions. Heating is seen in all regions below $\sigma = 0.9$, as well as between ±30° N above $\sigma = 0.2$. The twin warm regions noted in Figure 3.6 correspond to the regions of cooling seen in Figure 3.7. As the resolution increases, the cooling regions grow broader and the heating regions stronger, particularly towards the base of the model.

The time-averaged zonal mean zonal wind results are shown in Figure 3.8. As previously noted, a strong superrotating (moving faster than possible in solid-body rotation; see discussion on page 58) jet is found at the equator, confined on average to the region between ±25° N and below $\sigma = 0.2$, with weaker return flow outside this region. The jet is unbounded at the frictionless base of the model. This wind rotates in the same sense as the planet, but distinctly faster, and redistributes warm gas from the dayside to the nightside as well as cooler gas from the nightside back to the dayside, where it is heated once more. This cycle produces the tip of the warm chevron shape seen in Figure 3.3, together with the intrusion of cool gas into the dayside at its western end. In all cases, peak windspeeds are approximately 1200 m s^{-1} at 0° N, $\sigma = 0.8$, with precise maximum and minimum values of 1220, -687 m s^{-1} at T42L15, 1200, -693 m s^{-1} at T63L20, and 1179, -698 m s^{-1} at T85L20. These values are comparable to those obtained by Heng et al. (2011) with their spectral model in the 'shallow hot Jupiter' case, and the pattern corresponds well to those of both Menou and Rauscher (2009) and Heng et al. (2011). Differences of order 1% are noted in these results under variation of resolution and hyperdiffusion.

Several representative areas of the T42L15 run were chosen to study the time evolution of local temperatures and wind speeds, similar to figure 5 of Menou and Rauscher (2009), and these results are shown in Figure 3.9. For the polar areas, all locations

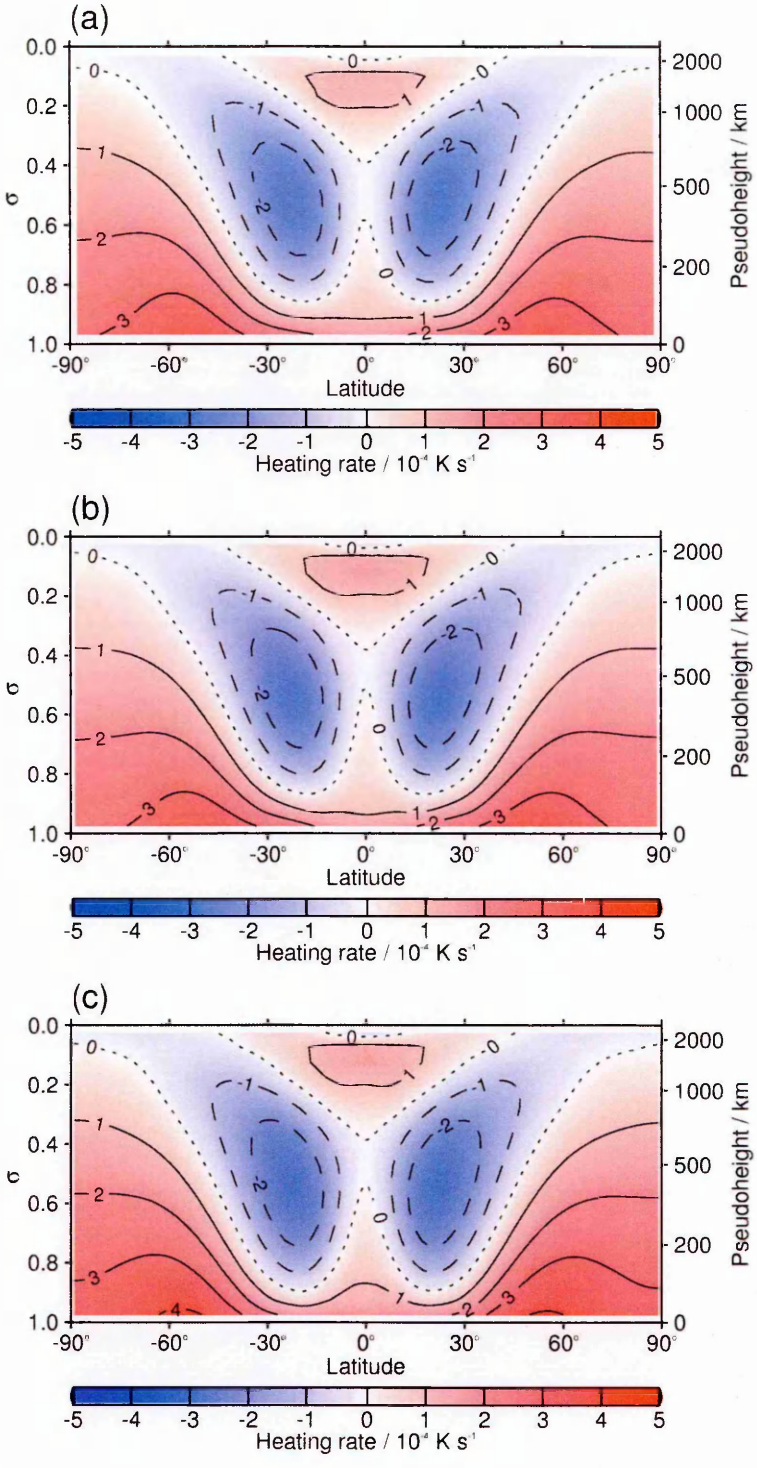

FIGURE 3.7. Time-averaged zonal mean heating rate plots. Note the units of 10^{-4} K s^{-1}. (a) T42L15, (b) T63L20, (c) T85L20

on the longitude circles of ±87.9° N were averaged, while equatorial locations were averaged between latitudes of ±4.2° N and over longitudes ±2.8° from the central coordinate. This area averaging both permits greater reproducibility, and also aids in avoiding model-specific coordinate issues, such as the presence/absence of a model grid point at ±90° N. Data were sampled ten times per day for all runs. Extremely high variability was recorded between individual records, and the data were smoothed using

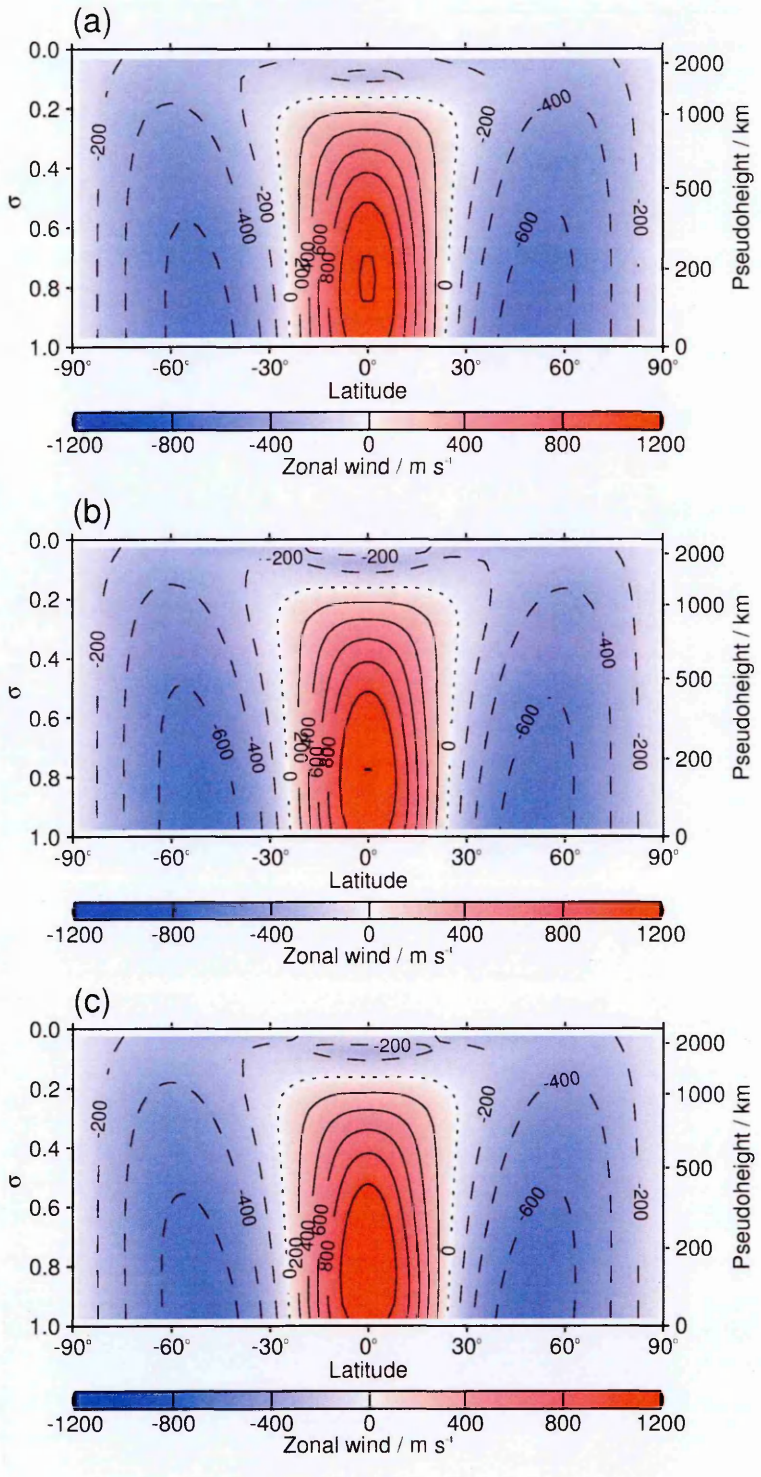

FIGURE 3.8. Time-averaged zonal mean zonal wind. Solid contours and red shading indicate wind directed towards the reader; dashed contours and blue shading the reverse. (a) T42L15, (b) T63L20, (c) T85L20

a simple boxcar function of width 1 day (11 records) to better display overall trends. Such variability demonstrates the requirement for frequent sampling, as daily sampling may miss high-frequency features altogether, or produce spurious signals through aliasing.

The streamfunction demonstrates both the circulation of the flow and the direction of that circulation. Figure 3.10 displays the time-averaged streamfunction and its stan-

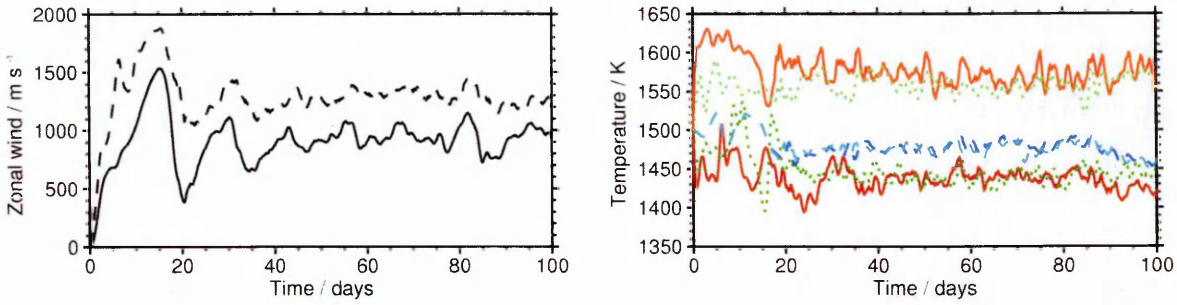

(a) (b)

FIGURE 3.9. Representative plots of (a) zonal wind, with the solid line the zonal mean wind at the equator and the dotted line the equatorial maximum; (b) temperature. The light and dark red lines represent the temperature at the sub- and anti-stellar points, respectively; the light and dark green dashed lines temperatures at the east and west limbs, respectively; and the blue and dark blue dashed lines show temperatures at the north and south poles, respectively.

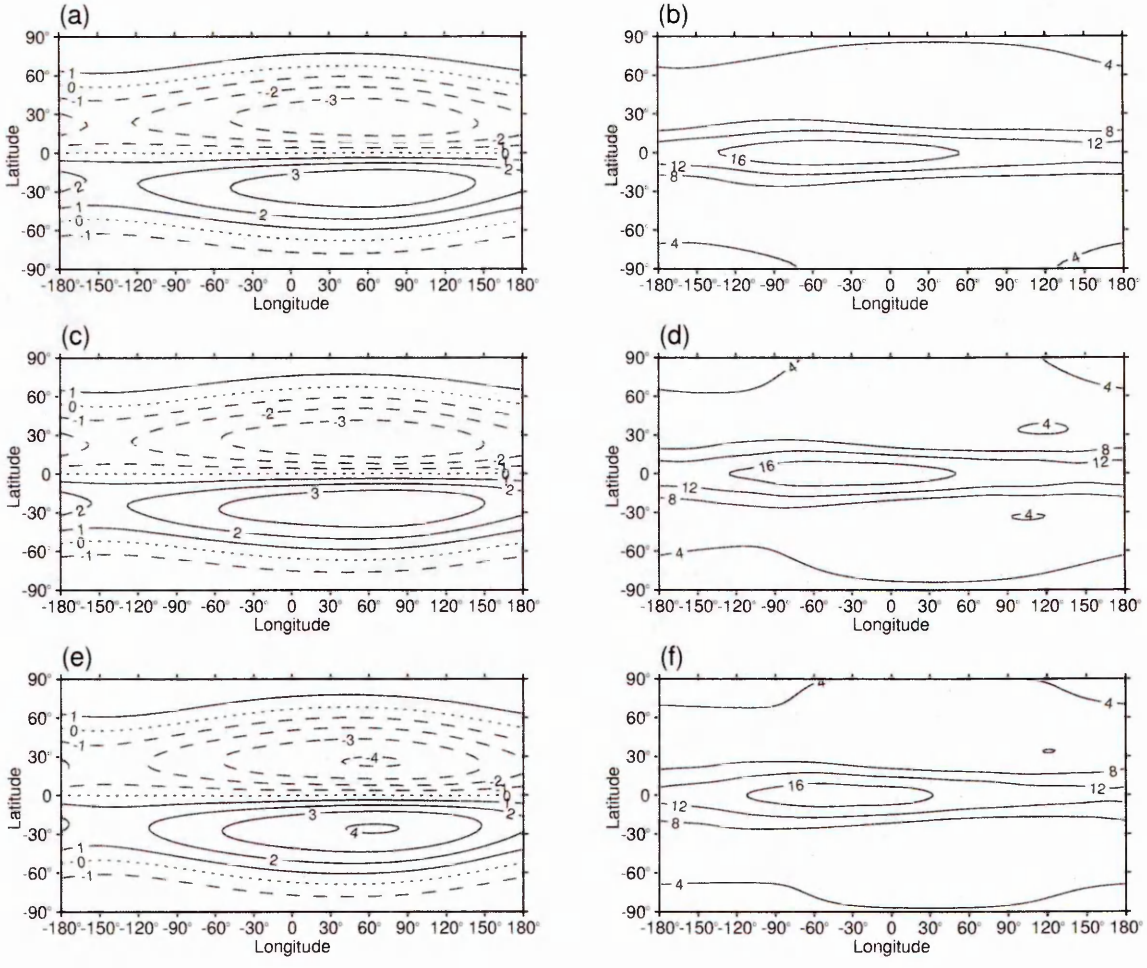

FIGURE 3.10. Streamfunction mean (left) and standard deviation (right) for (a) and (d) T42L15 at $\sigma = 0.7$; (b) and (e) T63L20 at $\sigma = 0.725$; (c) and (f) T85L20 at $\sigma = 0.725$. Mean contours: 10^{10} m^2s^{-1}; standard deviation contours: $10^9 m^2s^{-1}$.

dard deviation on the sigma level closest to $\sigma = 0.7$, with positive contours indicating clockwise circulation, and negative anticlockwise. It can be seen that there are two major circulation features, situated symmetrically about the equator approximately 60° E of the substellar point, while the greatest variability is found on the equator, around 60° W of the substellar point. The circulation at this level strengthens slightly with increasing resolution, with the maximum value of the streamfunction just exceeding 4×10^{10} m^2 s^{-1} at T85L20.

The effects of increased resolution are most clearly shown in Figure 3.11, which displays vorticity ($\zeta = (\nabla \times \mathbf{u})_z$; a measure of the local rotation at each point within the fluid) for the T85L20 and T42L15 runs, again on the nearest available sigma level to $\sigma = 0.7$. Vorticity is one of the quantities directly calculated by PUMA, and pro-

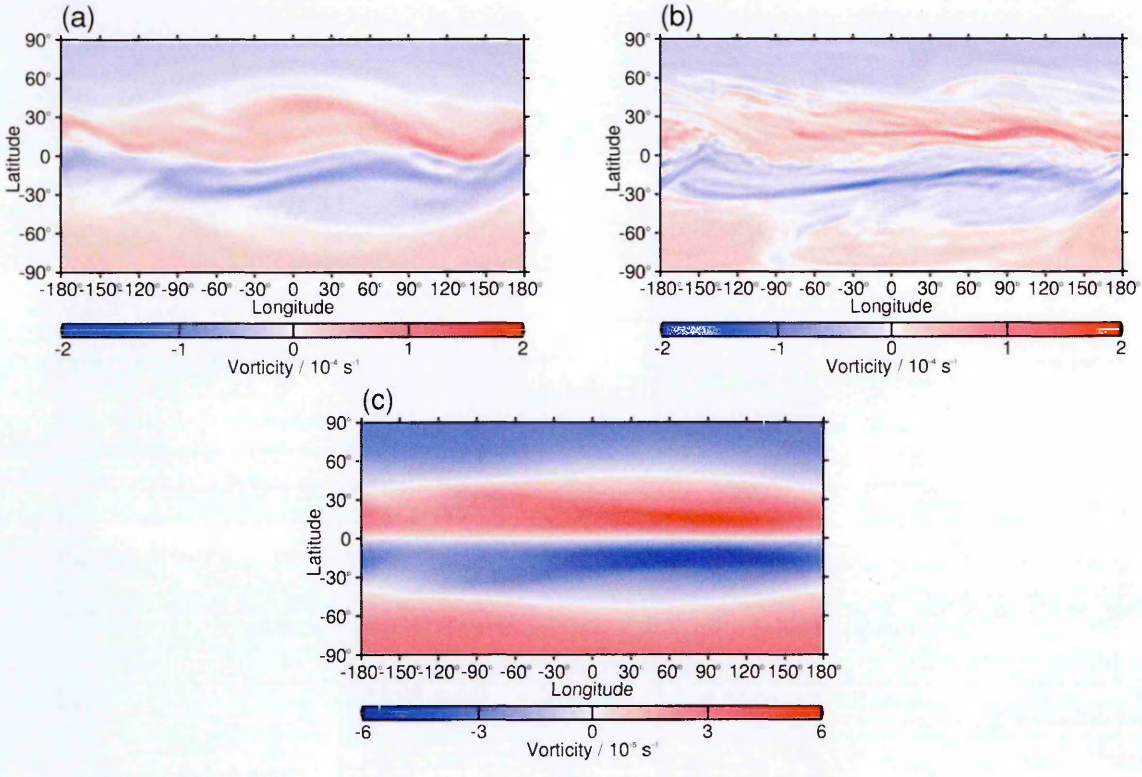

FIGURE 3.11. Vorticity day=100 snapshots and time mean for the T42L15 and T85L20 runs. (a) T42L15 day-100 snapshot at $\sigma = 0.7$; (b) T85L20 day-100 snapshot at $\sigma = 0.725$; (c) T85L20 time mean at $\sigma = 0.25$. Note the change in scale in this image.

vides a detailed picture of small-scale flow structure that cannot be as readily seen in plots such as wind speed. The third plot of Figure 3.11 shows a time mean, almost indistinguishable from the time means of other resolutions. Although the overall flow pattern is broadly similar across resolutions, as demonstrated in the previous figures, much smaller scales can be discerned in the T85L20 run, with long, thin 'streamers' of

high-magnitude vorticity visible that are washed out at lower resolution. The benefit of high-resolution runs is rendered clearly visible.

The mean meridional circulation is shown in Figure 3.12. This is a measure of

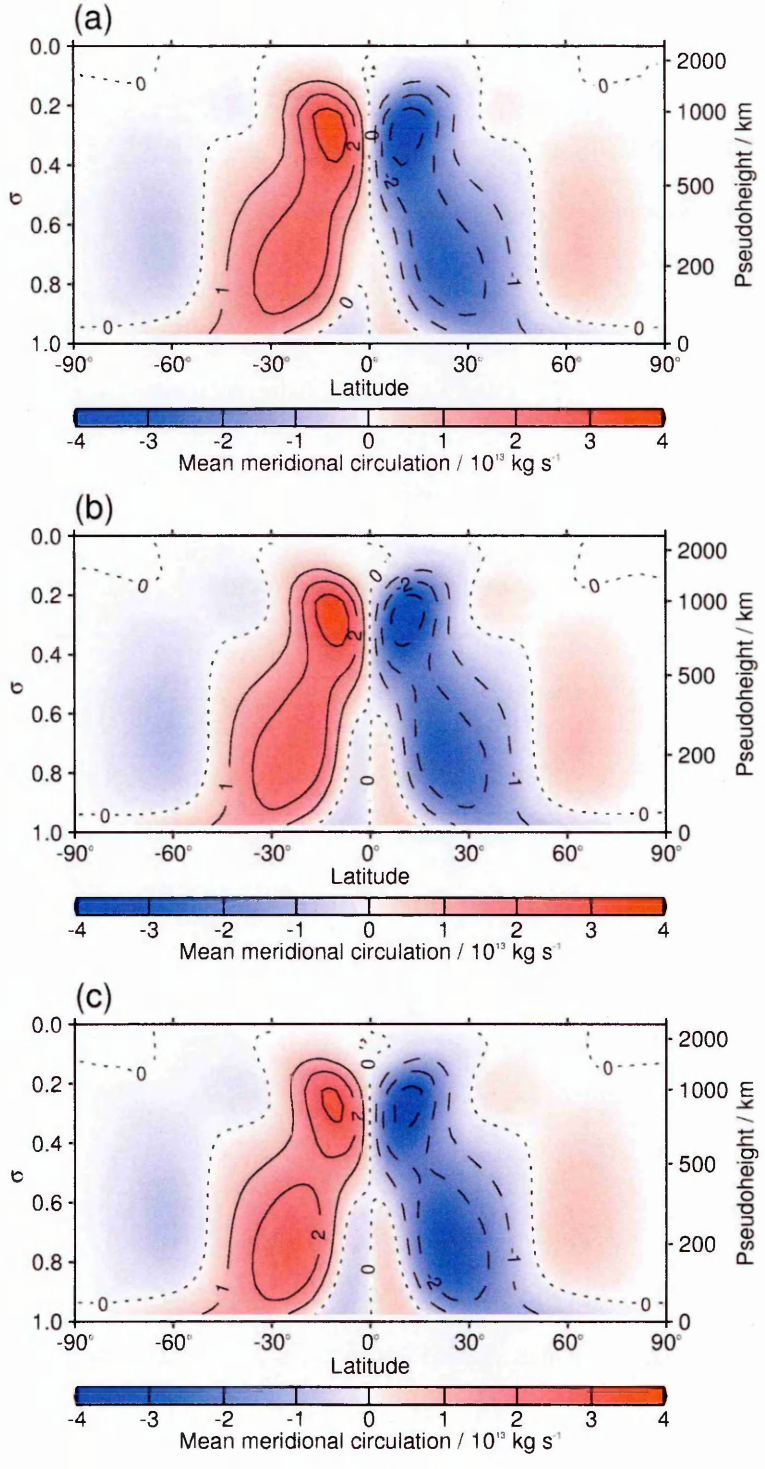

FIGURE 3.12. Mean meridional circulation. Positive contours correspond to circulation in a clockwise sense; negative contours to anticlockwise circulation. (a) T42L15, (b) T63L20, (c) T85L20.

the mass of gas circulating about a given point. Positive contours indicate clockwise circulation, and negative anticlockwise; a typical MMC plot for the Earth would show positive contours between 0°N and 30°N, illustrating clockwise circulation in which air

rises over the equator and descends further towards the north, followed by the inverse between 30°N and 60°N, and a further clockwise circulation between there and the pole. Similarly, the inverse pattern is seen in the Southern hemisphere. It can be seen that there are here two main circulation features, in which air descends over the equator (as expected from Showman and Polvani, 2011) and rises between ±30°N and ±60°N. The equatorial circulation contracts and weakens slightly with increasing resolution, with the two distinct peaks at different altitudes becoming more obvious.

Figure 3.13 shows the local superrotation index, which is a measure of the degree to which the angular momentum of each element of the atmosphere exceeds that which it would have in solid-body rotation. The local superrotation index s is defined by

$$s = \overline{m}/(\Omega a^2) - 1 \tag{3.2.5}$$

where $\overline{m}$ is the axial angular momentum per unit mass of the atmosphere derived from the zonal mean zonal wind $\overline{u}$, the longitudinal average of the zonal (eastwest) component u of the wind field (Lewis and Read, 2003). Ω is the planetary rotation rate in rad s^{-1}, and a the planetary radius. In general, the axial angular momentum per unit mass is given by

$$m = \Omega a^2 \cos^2(\phi) + ua\cos(\phi) \tag{3.2.6}$$

where ϕ is the latitude.

A global superrotation index S can also be calculated by integrating over the whole atmosphere:

$$S = \left(\int \int \int (ma^2 \cos(\phi)/g) \mathrm{d}\lambda \, \mathrm{d}\phi \, \mathrm{d}p \right) / M_0 - 1 \tag{3.2.7}$$

where g is the acceleration due to gravity, λ is the longitude, and p is the pressure. M_0 is the value obtained by performing the same volume integral with an atmosphere at rest with respect to the planet: if the atmosphere is at rest, $S = 0$.

A westerly wind (blowing west-to-east) over the equator cannot be created from an atmosphere initially at rest simply by moving air parcels from other regions of the atmosphere, since the maximum angular momentum available is that at the equator. The existence of superrotation ($s > 0$) is thus a signature of eddy processes occurring in the atmosphere, transporting angular momentum equatorward. A detailed study of superrotation under hot Jupiter conditions can be found in Showman and Polvani

(2011). Only the T85L20 run is displayed, as the results for each run are visually identical. The maximum value lies between 0.56 and 0.57 in each case, while the minimum is -1 at the poles.

Detailed study of the angular momentum budget over the course of each run reveals that the global superrotation index begins at $S = 0$, as expected from the model's initialisation state of zero wind. It then climbs over the first 15 days to a value of 0.033 ± 0.003 in each simulation, indicating that angular momentum is not fully conserved, and additional energy has been imparted to the atmosphere. With no diurnal tides, surface friction, or topographical features to provide this extra momentum, it is likely to have been acquired through model dissipation.

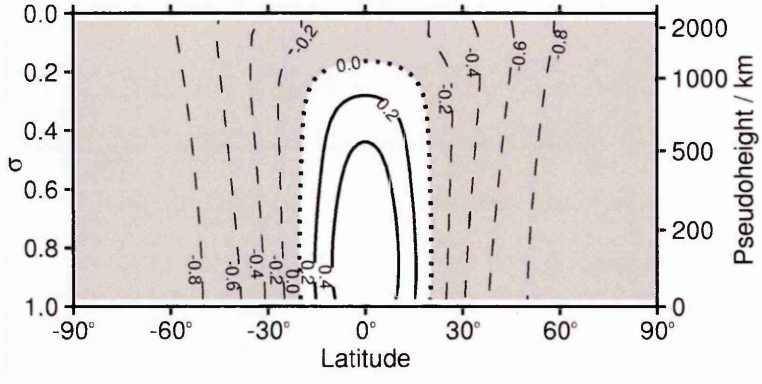

FIGURE 3.13. Time-averaged local superrotation index at T85L20.

The time evolution of the global statistics RMS (root mean square) vorticity ($\zeta = (\nabla \times \mathbf{u})_z$) and RMS divergence ($D = \nabla \cdot \mathbf{u}$) over the initial 400 days of the T42L15 run are presented in Figure 3.14. After between 25 to 30 days, a stable state is reached and the observed variability ceases to change. The same pattern is observed at all resolutions, although the mean values differ between them.

Finally, the kinetic energy spectra for the different resolution runs are displayed in Figure 3.15. Notably, low (large-scale), even (symmetric) wavenumbers have much higher amplitudes than their odd-valued counterparts, due to the highly equatorially symmetric, large-scale nature of the thermal forcing and final state. The dotted line has a slope of -3, which is the slope expected from an enstrophy-cascading range in two-dimensional turbulence. The majority of the spectrum lies closely parallel to this line, demonstrating that this regime holds over most modelled scales. This quasi-two-dimensional regime is to be expected from the scales reachable by these studies, as the

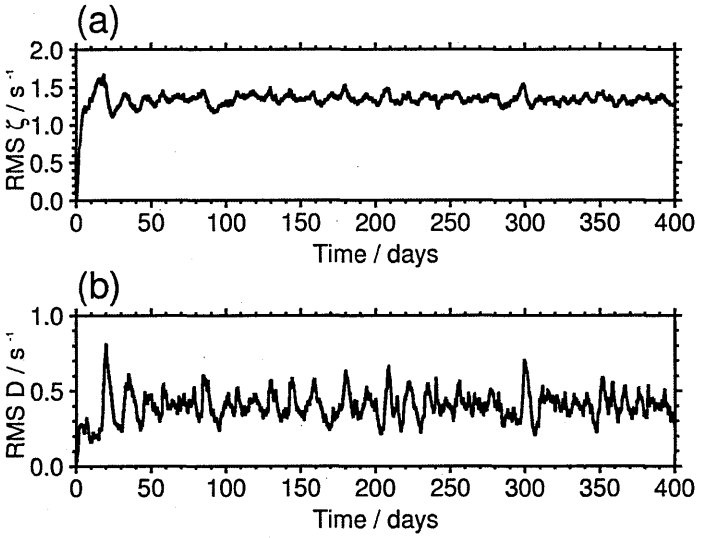

FIGURE 3.14. Global statistics for T42L15. (a) Global RMS vorticity; (b) global RMS divergence.

smallest resolved scale even at maximum resolution, T85, is still on the order of 10^3 km, with flow on this scale strongly constrained by the effects of planetary rotation and atmospheric depth, rather than fully three-dimensional turbulence (Houghton, 1986). Higher wavenumbers correspond to smaller scale features, and the greater kinetic energy present at higher wavenumbers in the higher resolution runs thus results in the greater detail and higher extrema seen most clearly in the vorticity plots of Figure 3.11. In each case, the spectrum tails off sharply towards the run's wavenumber cutoff, with a slope of around -15. This sharp decrease near the cutoff is not linked to physical expectations and is a result of the model diffusion. While diffusive processes do naturally occur, the limitations of modelling require that they must be represented at progressively larger scales (lower wavenumbers) as the model resolution decreases, to avoid an unphysical build-up of energy at the smallest resolved scales. In a true system, this energy would continue to cascade down to ever smaller scales and eventually be dissipated; the model system, however, cannot reach such small scales, and since it conserves energy efficiently, must have additional dissipation applied.

3.2.2. Varying the Rotation Rate of a Hot Jupiter. In extension to the intercomparison previously presented, the effect of varying further parameters is also tested. In this section, the planetary rotation rate is approximately doubled, and approximately halved, in order to study the effects. All other parameters are held constant, including the absolute timescale of the forcing.

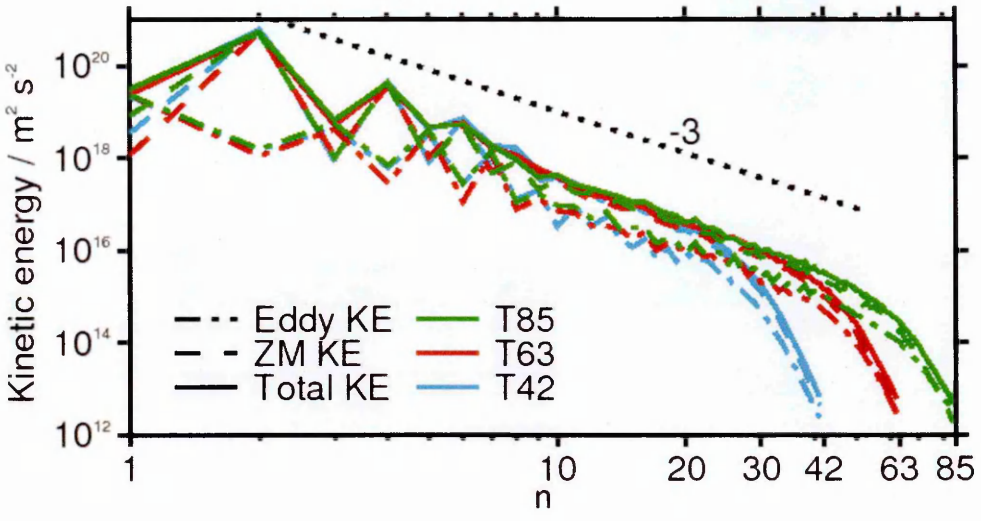

FIGURE 3.15. Kinetic energy spectra for all runs. The spectra have been averaged over all levels and over a period of 10 days. The blue lines denote the spectrum of the T42L15 run, the red lines T63L20, and the green lines T85L20. The total energy spectrum is shown as a solid line, with the zonal component as dashed and the eddy as dash-dotted. The dotted line is a reference line with a slope of -3.

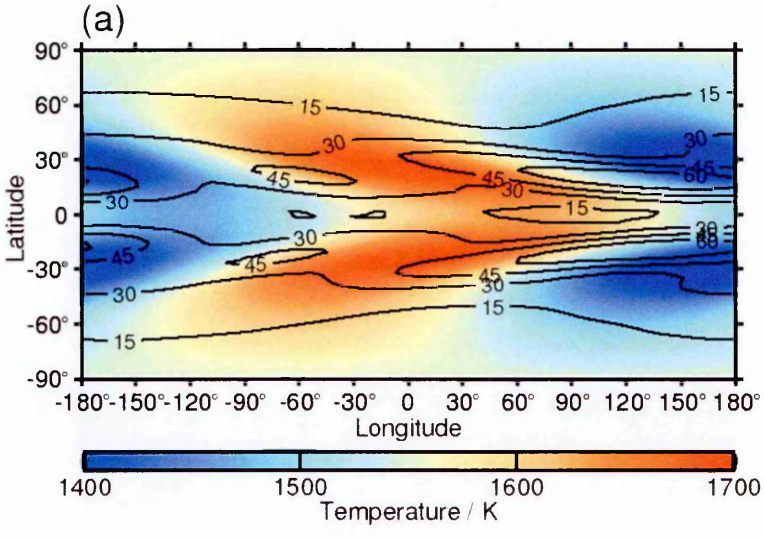

FIGURE 3.16. Temperature mean (colour) and standard deviation (contour) for the 2-day rotator.

Figures 3.16 and 3.17 show the mean and standard deviation of the temperature field on the $\sigma = 0.7$ model layer for the 2-day and 6-day rotation rate planets, respectively. Compared to the original intercomparison planet with its 3.5-day rotation period, the high-temperature chevron is stretched in the fast rotator, and almost absent in the slow rotator, where the shape becomes more similar to a slightly offset hotspot. The pattern of variation is similarly elongated and compressed, with distinctly higher polar variability in the slow rotator combined with lower maximum variability. The

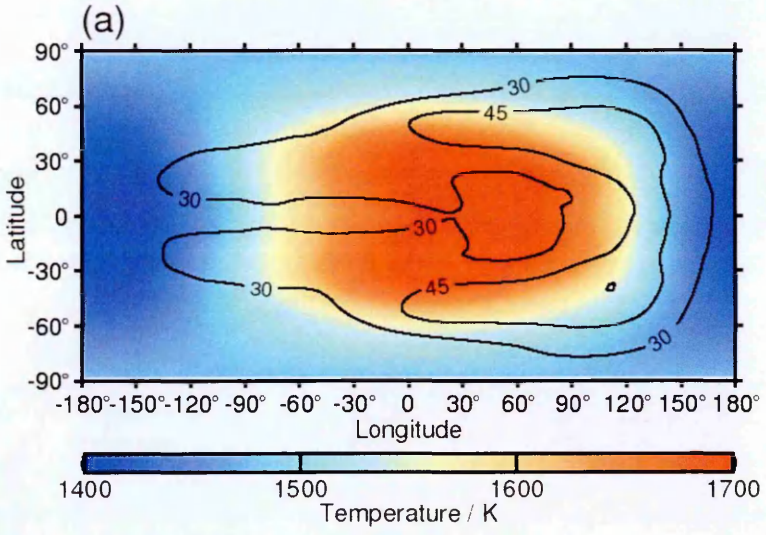

FIGURE 3.17. Temperature mean (colour) and standard deviation (contour) for the planet with a 6-day rotation period.

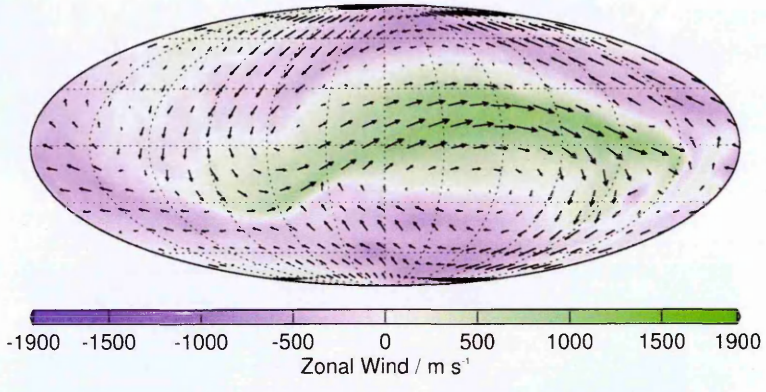

FIGURE 3.18. Snapshot of zonal wind strength (colour) and full wind vectors for the 6-day rotator at the end of the model run.

fast rotator is less variable towards the poles, with its maximum variability confined to $\pm 30°$ of the equator. Taken together with the zonal wind patterns in Figure 3.21, it appears that the equatorial jet meanders to a lesser extent over time. The high momentum of the winds in general engenders lesser scope for variability.

The snapshot plot of the wind shown in Figure 3.18 demonstrates the lesser constraints on the wind field in the slowly rotating model. A vortex has formed in the southern hemisphere, towards the equator, and winds flow directly over both poles, in contrast to the previous examples. Here the air flow in both eastward and westward directions distinctly crosses the equator, again contrasting with the previous models in which a strong equatorial jet dominated the flow.

Figures 3.19 and 3.20 show the mean and standard deviation of the zonal mean temperature field for the 2-day and 6-day rotation period planets, respectively. The faster planet has distinctly warmer poles and much less average temperature variation,

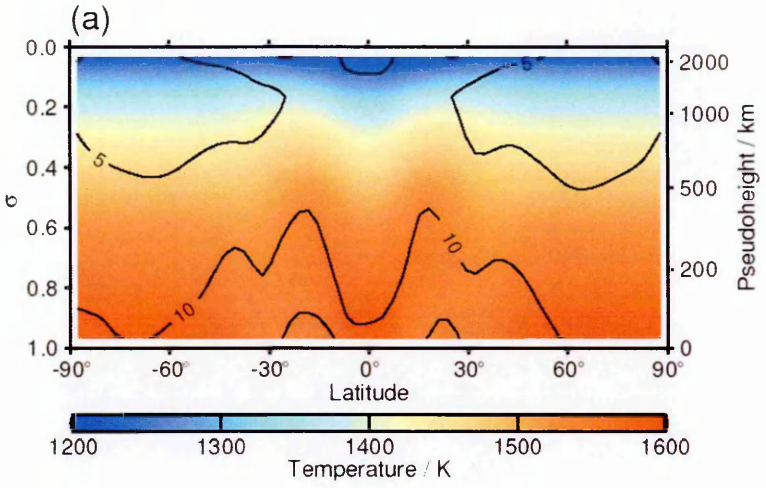

FIGURE 3.19. Temperature zonal mean temperature and standard deviation for the 2-day rotation period planet.

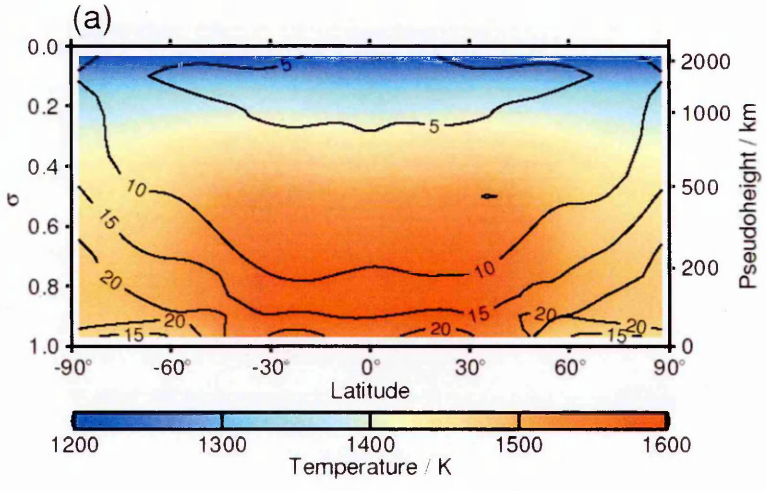

FIGURE 3.20. Time-averaged zonal mean temperature and standard deviation the the 6-day rotator.

with a faint v-shape of high temperature centred on the equator. The slow rotator has poles 100K cooler, with the forced hotspot much more visible, and displays distinctly greater variation in the standard deviation, particularly deep in the atmosphere and towards the poles.

Figures 3.21 and 3.22 show the time-averaged zonal mean winds for the 2-day and 6-day rotation period planets, respectively. The faster rotator develops much stronger winds higher into the atmosphere, with a strong superrotating jet between $\pm 25°$ N reaching a maximum time-averaged speed of approximately 1,700 m s^{-1}. By contrast, the maximum value reached by the time-averaged eastward wind in the 6-day rotator is only 440 m s^{-1}, and the westward winds exceed it in magnitude, reaching westward speeds of up to 590 m s^{-1}.

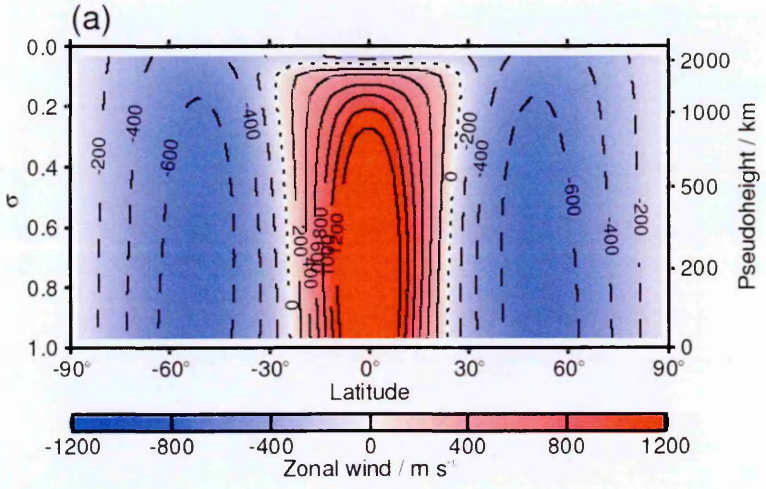

FIGURE 3.21. Temporally averaged zonal mean zonal wind for the rapidly rotating planet.

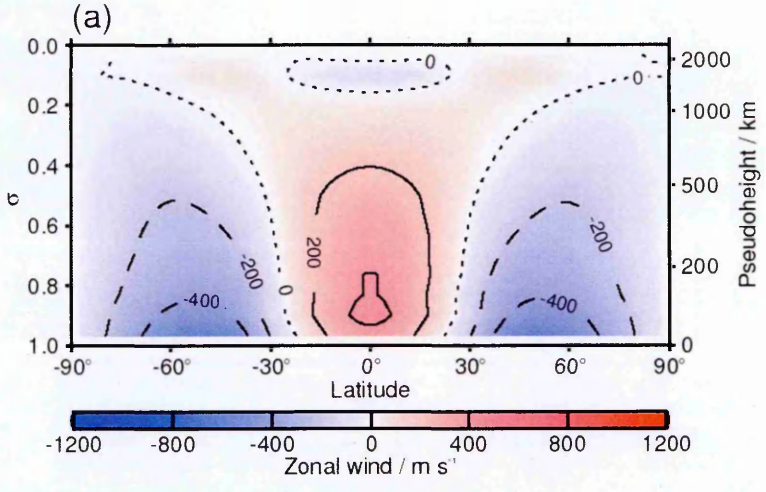

FIGURE 3.22. Temporally averaged zonal mean zonal wind for the slowly rotating planet.

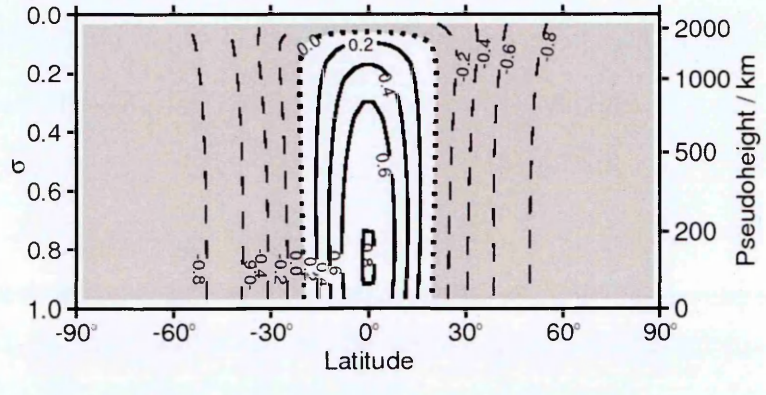

FIGURE 3.23. Time-averaged local superrotation index for the rapidly rotating planet.

Figures 3.23 and 3.24 show the superrotation index for the 2-day and 6-day rotation period planets, respectively. As is expected from the results above, the fast rotator

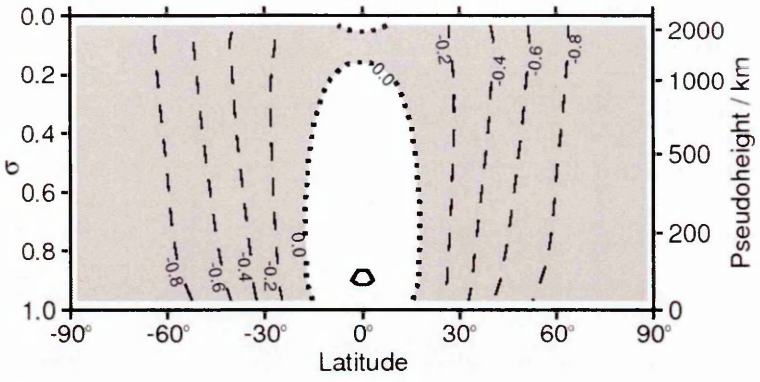

FIGURE 3.24. Time-averaged local superrotation index for the 6-day rotator.

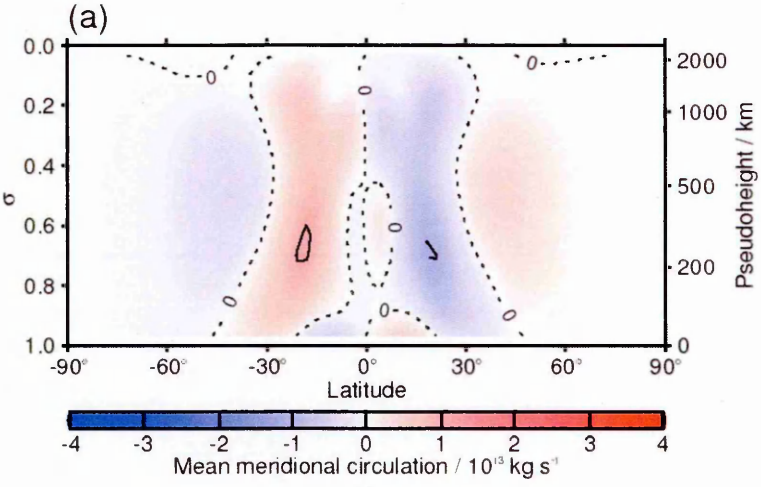

FIGURE 3.25. Mean meridional circulation for the planet with a 2-day rotation rate. The scale is chosen for direct comparison with the slow rotator, Figure 3.26.

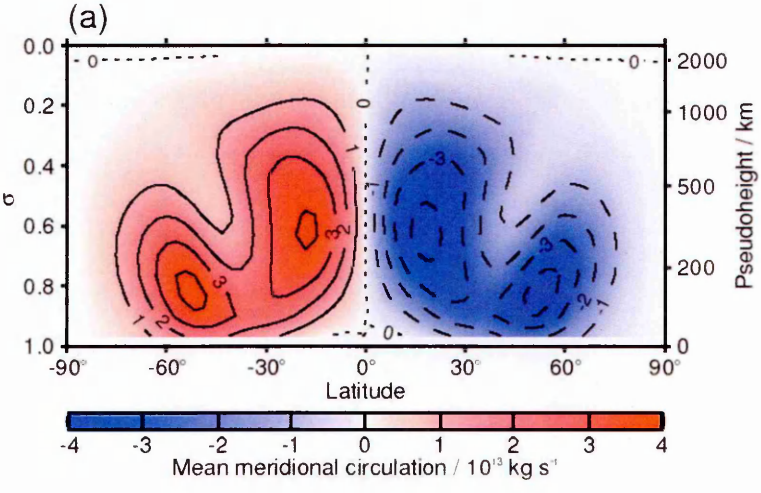

FIGURE 3.26. Temporally averaged mean meridional circulation for the planet with a period of 6 Earth days.

displays strong equatorial superrotation, while the slower planet shows only low levels of superrotation.

Figures 3.25 and 3.26 show the time-averaged mean meridional circulation for the 2-day and 6-day rotation period planets, respectively. Both planets, as with the primary intercomparison planet, show descending air over the equator, but are in other respects dissimilar. The slow rotator has a strong circulation that is uniformly clockwise in the southern hemisphere and anticlockwise in the northern, with two strong cells appearing to detach from one another in each hemisphere. By contrast, the fast rotator has much weaker circulation, and northern (southern) hemisphere circulation that is clockwise (anticlockwise) beyond approximately 40° N (40° S).

3.3. Discussion

The simple GCM PUMA is found to be a useful tool for hot Jupiter modelling scenarios. As a simple model, it is able to reproduce the large-scale dynamics of atmospheres in regions where its basic assumptions hold, without the complex requirements of a more realistic representation. Its code is highly resilient to numerical issues, to the extent that it proved useful to insert additional instability checks (see page 41) in order to limit the potential output to sensible results: as discussed by Thrastarson and Cho (2011), numerically stable models may continue to run well into regions with no physical meaning. These may be regimes dominated entirely by numerical noise, such as displayed in Figure 1(i) of Thrastarson and Cho (2011), or even, in the case of PUMA, results composed entirely of "NaN": not a number.

The hot Jupiter intercomparison simulation performed in Section 3.2.1 demonstrates amply the need for time mean plots in this field for the purposes of direct comparison. The snapshot plots commonly presented, while visually interesting and informative, cannot accurately capture the long-term state of the planetary atmosphere, since the high variability results in significant deviations from the average in any given snapshot. Mean and standard deviation plots, collected over an extended period of time, are preferable for model comparison, as they allow the overall similarities and differences of the long-term flow to be determined with ease. Another argument against the use solely of snapshot plots is that the individual weather features of a given planet cannot be predicted by this form of loosely-constrained modelling, only the types of features that may be observed. Due to the non-linearity of atmospheric modelling, no two model runs will reach the same state after the same period of time, as even minute differences may be rapidly magnified. With temporal averages, however, it becomes possible to predict typical variations in fields such as temperature, and areas of both high and low variability. Snapshots can then be used as an augmentation to provide an illustration of the sort of behaviour that results from moment to moment.

In the case of this somewhat hypothetical planet, a model based on HD 209458b, the results show a consistent pattern at all resolutions. While higher resolutions of T63 and T85 are able to capture more fine detail, the overall flow appears accurately represented at T42. This resolution, equivalent to a 64×128 grid in latitude and longitude, results if translated in a point spacing of approximately 4.9×10^3 km at the

equator, on a planet 10^5 km in radius or 6.3×10^5 km in circumference. While large, this scale appears suited to capturing the broad-scale nature of the relatively simple flow.

This flow is dominated by a high-strength superrotating wind at the equator, which is predicted to extend below the 1-bar pressure at which the model base was situated, as seen from Figure 3.8 (a)-(c). Above and poleward, it is surrounded by a weaker counterrotating wind. These plots have been averaged twice: once in longitude and once in time, and the equatorial jet as seen from moment to moment displays a thinner, stronger pattern that weaves north and south, bounded between approximately $\pm 30°$, as illustrated in Figure 3.4 (a) and (b). This high-strength wind and the vortices that result on either side of it tracks the point of highest equatorial temperature eastward, while towards the poles, it is advected westward. On average, an equatorially symmetric chevron shape is produced, shown in Figure 3.3 (a)-(c). The equator itself no longer hosts the warmest or coolest points, as the forcing alone would dictate (see Figure 3.1): these are migrated to, on average, symmetric pairs of locations $\pm 30°$ N off the equator for the hottest points, and approximately $\pm 40°$ N for the coolest. At any given moment, however, snapshot plots will show one of these regions to be significantly warmer than the other. Faster (slower) rotation rates are found to result in faster (slower) equatorial winds, but an opposite effect is noted in the overturning mean meridional circulation, which becomes much stronger in the slow rotator, with one cell occupying each hemisphere.

CHAPTER 4

Interior Modelling

The nature of a gas giant planet is dependent on its evolution. Many exoplanets demonstrate unexpected characteristics, such as radius inflation, that can only be explained by studying their evolutionary history. Composed primarily of hydrogen and helium, gas giant planets are similar to low-mass stars, and in fact exist on a continuum with brown dwarfs, the exact demarcation between the two groups still not unanimously defined (in this work, it is the $13M_{\mathrm{J}}$ deuterium-burning mass limit). Numerical models have been used with great success to study the evolutionary behaviour of stars and giant planets, and as such are the tool of choice for this purpose.

In this chapter, one interior structure model used is introduced, explained, and tested, and giant planet experiments carried out to investigate the effects of variables such as metallicity, core mass, and external irradiation on the evolution of gas giant planets. Section 4.1 covers the basics of the stellar/giant planetary code MESA (Modules for Experiments in Stellar Astrophysics). MESA was chosen as it is an open-source model with an active community engaged in both using and upgrading the code, and in particular has recently been extended to explicitly cover the modelling of giant planets. Technical information on the model may be found in Section 4.1.1, covering: the equations of stellar structure; the method in which they are solved; and the input physics, covering from the equation of state to atmospheric boundary conditions. Initial model tests are documented in Section 4.1.2.

Experiments carried out with MESA are detailed in Section 4.2. Giant planets are simulated throughout their lifespans, with and without external irradiation, and with various metallicities and core masses. Section 4.2.1 analyses the evolution of isolated (non-irradiated) Jupiter-mass planets with varying metallicity and core mass, while Section 4.2.2 adds stellar irradiation to a selection of these planets to investigate the differences in development thus produced. Finally, Section 4.3 analyses the results collected in all experiments, drawing them together to synthesise general conclusions.

4.1. MESA

MESA, Modules for Experiments in Stellar Astrophysics, is a complex Fortran-90 suite of tools which can be used for one-dimensional simulations of stars and self-gravitating gaseous objects throughout their lifespan, and across a broad range of masses (Paxton et al., 2011). Of particular relevance to this project is its ability to model low-mass objects down to the mass of Jupiter or even smaller, to a limit of approximately $0.1M_J$ (Paxton et al., 2013).

4.1.1. Technical Information. As a massive, isolated, self-gravitating body, a star may be reasonably assumed to be spherical for the purposes of modelling. Departures from a spherical shape may be caused by rotation and/or magnetic fields in an isolated star, but the energy associated with these factors is typically much smaller than the gravitational binding energy of the object (Prialnik, 2000). This simplification permits modelling to be carried out in one dimension only, along a radial line from the centre to the outer edge of the star. If local thermodynamic equilibrium is also assumed within the star, all thermodynamic properties may then be uniquely calculated in terms of the density, temperature, and composition at each point on the radial line at a given time.

The variety of scales related to the processes that determine the structure of stars is enormous, from the atomic all the way up to the size of the star itself, and the relevant timescales similarly vary by many orders of magnitude. To model the evolution of a star over its full size and lifetime, further simplifications need to be introduced, parametrising the small-scale and short processes. The state of the stellar material is parametrised through the use of pre-calculated equation of state (EOS) tables, covering the full range of temperature and pressure to be encountered in such systems. Nucleosynthesis is input via a nuclear network, which specifies the rates of many nuclear reactions under a variety of conditions. Opacities required for calculating radiative diffusion and electron conduction are also largely covered by pre-calculated tables.

Though convection is a very important element of stellar evolution, it is an inherently three-dimensional turbulent process operating on much shorter timescales than the evolution of stars and planets, and must also be simplified. The treatment used in MESA is the mixing length theory (see, for example, Weiss et al., 2004, and references

therein), with an option for an alternate convection scheme described by Henyey et al. (1959).

Using radial distance from the centre, r, as the independent variable, the equations of stellar structure are as follows (Carroll and Ostlie, 1996):

$$\frac{dP}{dr} = -\rho g \tag{4.1.1}$$

$$\frac{dm}{dr} = 4\pi r^2 \rho \tag{4.1.2}$$

$$\frac{dL_r}{dr} = 4\pi r^2 \rho \epsilon \tag{4.1.3}$$

$$\frac{dT}{dr} = -\frac{3}{4ac}\frac{\kappa\rho}{T^3}\frac{L_r}{4\pi r^2} \tag{4.1.4}$$

$$\frac{dT}{dr} = -(1-\frac{1}{\gamma})\frac{\mu m_H}{k}\frac{Gm}{r^2} \tag{4.1.5}$$

Here, P is the pressure, m the mass coordinate (denoting mass enclosed: it is 0 at the centre of the object and M, the total mass, at the edge), r the radius coordinate, ρ the density at radius r, T the temperature, and L_r the luminosity due to the energy generated within the sphere of radius r. g is the local acceleration due to gravity at radius r, $g = GM/r^2$ Further, κ is the Rosseland mean opacity and ϵ the energy generation rate per unit mass. This may contain terms due to nuclear burning and/or to gravitational contraction. If the object undergoes expansion, the gravitational term will of course be negative. G is the gravitational constant, c the speed of light, $\gamma = C_P/C_V$ the ratio of specific heats, and the radiation constant $a = 4\sigma/c$, where σ is the Stefan-Boltzmann constant. Finally, μ is the mean molecular weight, and m_H is the mass of a hydrogen atom: μm_H is the average particle mass.

Equation 4.1.1 is the equation of hydrostatic equilibrium. The assumption of hydrostatic equilibrium is justified by the observation that stars are, relatively speaking, static throughout the better part of their evolution, and is a primary assumption of stellar modelling. Equation 4.1.2 is the continuity equation, expressing the conservation of mass throughout the star. Equation 4.1.3 describes the energy generation within the star. Finally, Equations 4.1.4 and 4.1.5 are the equations of energy transfer through radiative diffusion and (adiabatic) convection, respectively. Energy transport switches between these two forms depending on the local conditions: if a fluid parcel always at the pressure of its surroundings will continue rising (or sinking) following a small

vertical displacement, convection will prevail, whereas radiative transport dominates when the resultant forces on such a parcel tend to restore it to its original location.

For a hydrogen-helium giant planet, the main constituents are very similar to those of a star. However, no energy is generated through nuclear fusion, with the main energy source becoming gravitational contraction, and a small solid core may exist at the planet's centre. In addition, the equation of state needs to be extended to regions of temperature and pressure not typically experienced in stars, and external irradiation may need to be taken into account. With these modifications, the same basic equations and types of model remain broadly applicable for such gas giant planets, and in particular, MESA has recently been extended to cover planetary masses down to $0.1 M_{\rm J}$, as described by Paxton et al. (2013).

4.1.1.1. *Model Initialisation.* For creation of a planetary-mass object, the desired final mass and radius are input, and MESA iterates the values of central pressure and specific entropy until it succeeds in constructing a model of this mass and radius in hydrostatic balance with an adiabatic temperature profile. This procedure works well down to $0.1 \mathrm{M_J}$, and is sufficiently flexible to permit a range of initial radii to be used for a given mass (Paxton et al., 2013).

It is also possible to create a planetary-mass object using the star construction routines, by forming a low-mass star in the pre-main-sequence stage and manually subtracting mass from it, but this method is time-consuming and prone to instability. After each mass subtraction, the object must be "relaxed" to an equilibrium state before the next subtraction can be performed, and stable solutions may not be found if too much mass is removed in a single step.

4.1.1.2. *Equation Solver.* The evolutionary module solves the equations of stellar structure based on the scheme by Henyey et al. (1959). The equations of stellar structure are replaced by second-order difference equations, which are solved, together with the appropriate boundary conditions, using a Newton-Raphson solver. The interior boundary condition is typically at $r = 0$, but may be located at non-zero radius and with non-zero enclosed mass in the case where a core has been added to the object. At this location, the radius, luminosity, and velocity are specified. At the outer boundary, the boundary conditions are determined by the atmosphere module, as discussed in Section 4.1.1.4.

In order to model the star or planet, it is split into small radial cells, the number and width of which may be adjusted automatically during the run to optimise the use of computational resources. The star is modified according to the processes underway, e.g. by redistribution of elements, appropriate coefficients determined, and the model then solves for a new structure and composition. If a solution cannot be reached, the timestep is decreased and the model retries, until either a solution is found or the timestep becomes unacceptably small, causing MESA to stop.

4.1.1.3. *Input Physics.* The MESA model utilises a series of lookup tables for the equation of state, the opacity, nuclear reaction rates, and some atmospheric boundary options. The majority of fundamental physical constants are taken from the CODATA recommended values of Mohr et al. (2008), with solar values (mass, radius, age, and luminosity) taken from Bahcall et al. (2005).

The equation of state data are based on the OPAL EOS (Rogers and Nayfonov, 2002) and extended by the SCVH (Saumon et al., 1995), HELM (Timmes and Swesty, 2000), and PC (Potekhin and Chabrier, 2010) equations of state. Figure 4.1, taken from Paxton et al. (2011), demonstrates the regions in which each EOS is applicable. At high ($Z > 0.04$) metallicity, HELM and PC cover the entire EOS range, since OPAL/SVCH are not formulated for these metallicities. Additional tables for Z = 0.2 and Z = 1.0 have been added using the code of MacDonald and Mullan (2012) for the case of partial ionisation (Paxton et al., 2013), since HELM assumes full ionisation throughout. Additionally, code hooks are provided for the incorporation of user-specified EOS data.

Nuclear reaction rates are provided from a variety of sources, listed in Paxton et al. (2011) and updated in Paxton et al. (2013). In the gas giant case, thermonuclear reactions are negligible or absent, and no heating or composition changes are effected by this method, with energy sources and sinks arising due only to gravitational contraction and expansion.

Opacity tables are calculated by combining the OPAL radiative opacities (Iglesias and Rogers, 1993, 1996), and at low temperature either Ferguson et al. (2005) or Freedman et al. (2008), with the electron conduction opacities of Cassisi et al. (2007). Some of the opacity table regions are shown in Figure 4.2.

Convection in the object is handled using the mixing length theory, with two options: either standard (Weiss et al., 2004) or the modified variant used by Henyey et al.

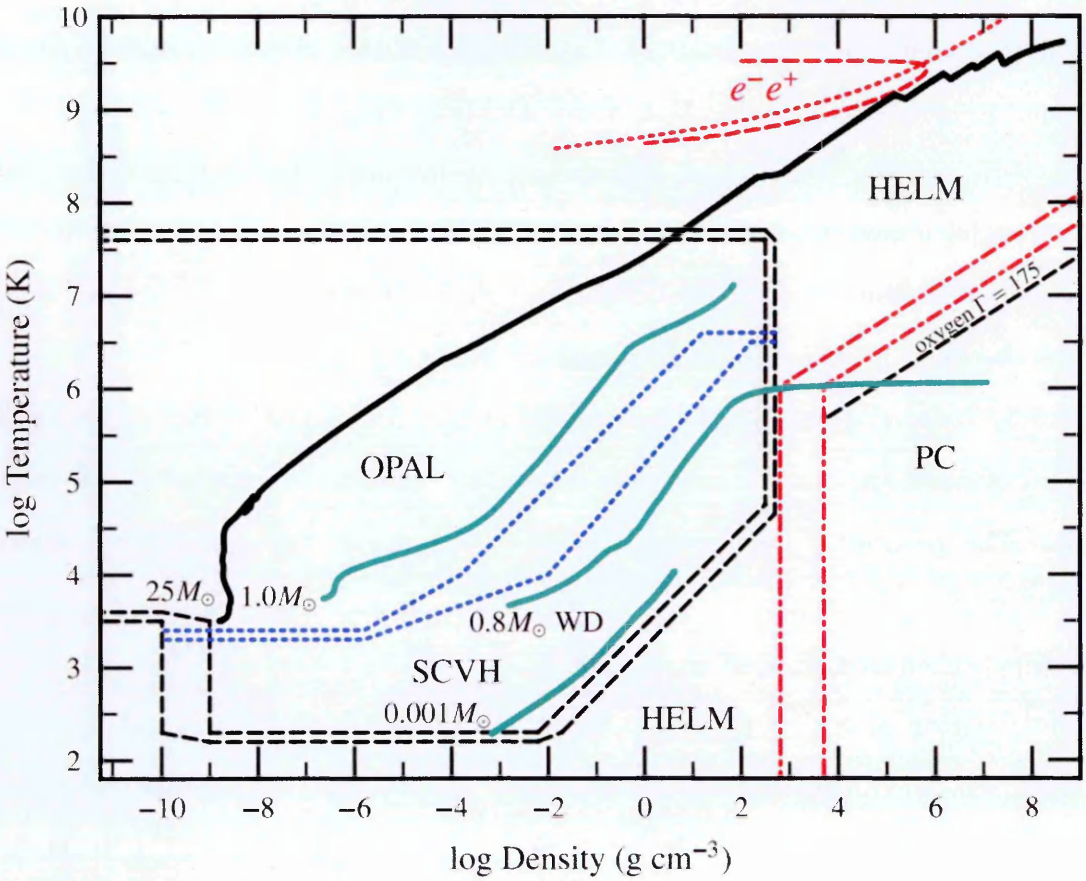

FIGURE 4.1. Equation of state region plot for MESA, taken from figure 1 of Paxton et al. (2011). The black dashed lines represent the edge and blending region of the combined OPAL+SCVH EOS, while the blue dotted lines indicate the region of blending between OPAL (above) and SCVH (below). The PC blending area is outlined by the red dot-dashed lines, with PC below and to the right, and HELM provides the remainder of the plot. The solid lines indicate the stellar profiles for a variety of objects, labelled in all cases at the left-hand end of the line. Of particular note is the $0.001M_\odot$ profile, which is of the order of masses studied in this work. The dotted red line indicates the region in which the number of electrons per baryon is doubled due to pair production, and the first adiabatic exponent $\Gamma_1 \left(\equiv \left(\frac{d\ln(P)}{d\ln(\rho)}\right)_{\rm ad}\right) < 4/3$ to the left of the dashed red line.

(1965). The mixing length is a defined average length over which a convective element is assumed to travel before losing its identity and mixing with its surroundings. There is then a parametrisation for overshoot mixing, which accounts for the effects at convective boundaries, where a convective parcel, having a momentum due to its previous motion, overshoots the region in which it would have been stable, resulting in a layer in which mixing continues to occur immediately outside the boundaries of zones that meet the criteria for convection. Semiconvection and thermohaline mixing have been more recently implemented, as described by Paxton et al. (2013).

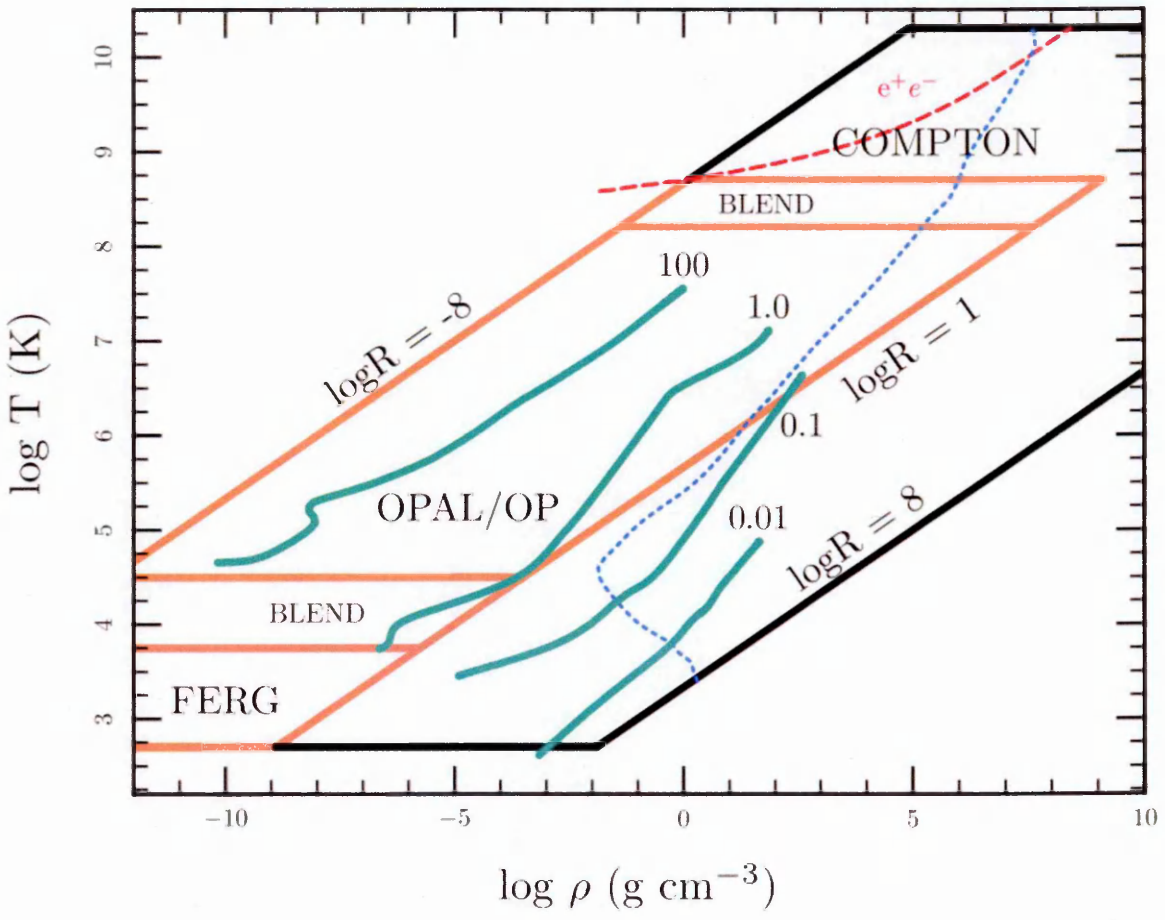

FIGURE 4.2. Opacity region plot for MESA, taken from figure 2 of Paxton et al. (2011). The orange-bounded regions are those in which input tables for radiative opacities exist, while the black-bordered region is that in which algorithms are used to derive the total opacity. The different labels in orange regions denote the source of the opacity tables used or where the tables are blended together: OP refers to the opacities of Seaton (2005), which may be used in place of the OPAL tables, while FERG indicates the opacities of Ferguson et al. (2005). To the right of the dashed blue line, the opacities are dominated by electron conduction. The dashed red line is the line above which the number of electrons and positrons produced by pair production exceeds the number of electrons produced by ionisation. Profiles of simulated objects of differing masses are again shown as turquoise lines, each labelled with the relevant mass. Further options for opacity have since been added, introducing both updates and an option to switch between Ferguson et al. (2005) and Freedman et al. (2008) at low temperatures. (Paxton et al., 2013).

MESA also has the ability to add an inert core to the centre of the object, as described in Paxton et al. (2013). This core has a specified mass, radius (or density), and luminosity, and is not evolved at any point in the model run, essentially an alternate inner boundary condition. Due to the relatively high density of a solid rock/ice core, its presence can have a significant impact on the radius of the planet for a given planet mass.

4.1.1.4. *Atmospheric Boundary Conditions.* Of particular relevance to this project are MESA's available atmospheric boundary conditions. These describe the outer boundary for the model during its evolution. Atmospheres both with and without irradiation may be specified, using a variety of prescriptions. Three sets of atmospheric tables are provided, one suitable for the evolution of stars, one for brown dwarfs and giant planets, and one calculated for white dwarf atmospheres. Another atmospheric option is to carry out direct integrations of the hydrostatic balance equation:

$$\frac{dP_{\text{gas}}}{d\tau} = \frac{g}{\kappa} - \frac{a}{3}\frac{dT^4}{d\tau}$$

This is done using one of two available relations between T and τ, the optical depth: either that of Eddington (1926), $T^4(\tau) = 3T_{\text{eff}}^4(\tau + 2/3)/4$, or Krishna Swamy (1966).

There is a further option to use the constant opacity solution of radiative diffusion, specifying τ_s and optionally κ_s, which will otherwise be calculated iteratively, using the initial value of P_s and a guess at κ_s typically based on the value in MESA's outermost cell. This option is also used as a fallback in the case that the model leaves the range covered by the supplied tables, or the integrative procedure described fails.

Also included is the grey irradiated atmosphere model formulated by Guillot (2010) and in part based on the work of Iro et al. (2005). Using this prescription, the outer boundary of the interior model is imposed at a specified pressure, rather than a specified optical depth. The pressure adopted must be sufficiently high that absorption of irradiation in the atmosphere is fully accounted for. This irradiated atmosphere model is of particular relevance to the implementation of PUMA results, discussed in Chapter 5.

In addition, MESA contains the option to apply a surface energy generation rate $\epsilon = F_\star/4\Sigma_\star$ due to external irradiation. $F_\star$ is the dayside flux from the star, while $\Sigma_\star$ is the mass column depth, with energy only generated where $\Sigma(r) \leq \Sigma_\star$, effectively specifying the maximum depth into the atmosphere to which stellar irradiation can penetrate. This construction mimics the deposition of energy into the outer layers of the object by the radiation received from its parent star. This option is specified by two variables determining respectively the incident flux and the column depth at which this flux is expected to be fully absorbed.

Further, code hooks are present for the addition of user-defined heating or atmospheric model routines.

4.1.2. Model Tests. In order to ensure the correct operation of the model, some simple tests were carried out, evolving a variety of models and comparing them to standard expectation to confirm that MESA functions as expected on the current system.

4.1.2.1. *Low-Mass Objects.* Brown dwarfs spend their lifetimes cooling and contracting. While deuterium fusion begins in the cores of these objects, sustained hydrogen fusion is not possible, and not enough power is generated to maintain them against gravitational collapse. Brown dwarfs thus share some characteristics with main sequence stars, and some with planets: in order to model gas giant planets as a believable part of this continuum, MESA must be able to model brown dwarfs. The upper limit for the mass of a brown dwarf is approximately $75M_J$, dependent on metallicity: at solar metallicity the hydrogen-burning minimum mass (the mass above which sustained hydrogen fusion becomes possible in the core) is $0.072M_\odot$, increasing for lower metallicities. (Chabrier and Baraffe, 2000) Below approximately $13M_J$, no nuclear burning takes place in any appreciable quantity, and the object is (in this thesis) considered a planet.

4.2. Experiments

4.2.1. The Evolution of Isolated Jupiter-Mass Objects. All planets in this section are derived from a set of three Jupiter-mass objects with differing metallicities: $Z = 0.01$, $Z = 0.02$, and $Z = 0.03$, all with helium fraction $Y = 0.25$. The three original low-mass base objects were created using the MESA "create_initial_model" routine described in Section 4.1.1.1, which creates a model of the specified mass and radius with an adiabatic temperature profile and constant entropy, assuming no nuclear burning takes place. Other than their metallicity, these models are created with identical setup parameters, with an initial radius of 1.85 R_J. They were relaxed for 50 model steps, a procedure permitting the model to adjust to better suit its specified beginning or alternate parameters before full evolution begins, then saved at an early age after 25 evolution steps so that they remain at almost zero age. These three initial models (**M01**, **M02**, **M03**) are then used as starting points for all further operations.

As a first task, the base models **M01**, **M02**, and **M03** were evolved without further change from their saved states to the age of 4.5 Gyr, the approximate age of the Solar System, both to ensure that these starting models were stable over long-term evolution and to provide base data points with which to compare planets with added massive cores.

To each of the base models, a series of core masses were added, each at a constant density of 10 g cm^{-3}. This procedure required: first, removal of mass from the planet equivalent to the core mass to be added; second, a specific inert core mass to be applied in the centre of the planet; and third, the radius of the core specified. The core is considered inert and does not interact with the rest of the planet, nor is it evolved in any way: following creation, the core remains unchanged throughout evolution, providing a replacement inner boundary condition at non-zero r. The core masses used were 1, 5, 10, 20, 30, and 40 $M_\oplus$. The full suite of models is shown in Table 4.1.

	$0M_\oplus$	$1M_\oplus$	$5M_\oplus$	$10M_\oplus$	$20M_\oplus$	$30M_\oplus$	$40M_\oplus$
Z = 0.01	M01	M01c01	M01c05	M01c10	M01c20	M01c30	M01c40
Z = 0.02	M02	M02c01	M02c05	M02c10	M02c20	M02c30	M02c40
Z = 0.03	M03	M03c01	M03c05	M03c10	M03c20	M03c30	M03c40

TABLE 4.1. Table of the abbreviatons for all models studied in the section by metallicity and core mass.

With these models constructed, all were again evolved to the age of 4.5 Gyr. Comparisons of the results may be seen in Figures 4.3 to 4.7, each of which is separately analysed in detail below.

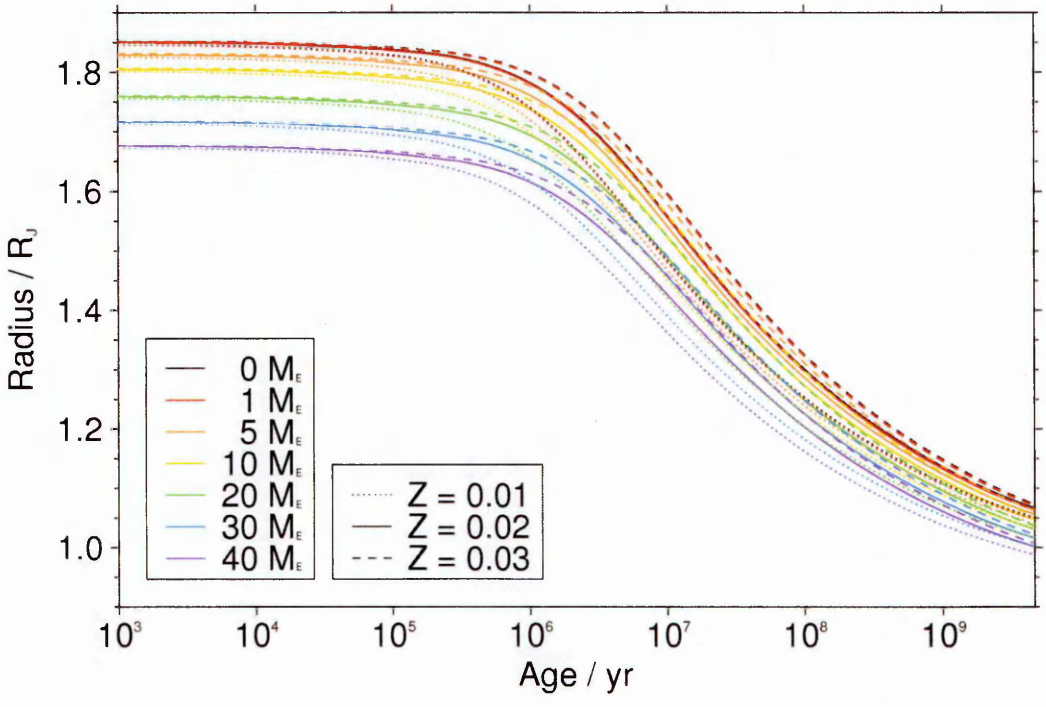

FIGURE 4.3. Comparison of the radius evolution of all core-only planets, with the 'base' planets for comparison. Linestyle indicates metallicity, colour core mass. Note that the X-axis is logarithmic to better display the evolution. The planets with zero core mass evolve essentially identically to their $1M_{\oplus}$ core mass counterparts of the same metallicity, with the result that, while both lines were plotted in all cases, the black solid, dashed, and dotted lines are essentially hidden by their red counterparts.

4.2.1.1. *Radius Evolution.* Figure 4.3 shows the evolution over time of the radius of all evolved planets. In all cases, the lower metallicity planets start at almost identical radii to other planets of the same core mass, but begin to contract earlier and more rapidly than their higher metallicity counterparts. Lower-metallicity planets will typically have lower atmospheric opacities, permitting radiation to be lost more rapidly than from an otherwise identical high-metallicity planet and thus increasing the rate at which the planet is able to cool. The difference becomes less pronounced as the planets age and the higher-metallicity planets 'catch up' to an extent, but remains clear up to the final age of 4.5 Gyr, resulting in a typical difference of 0.01 - 0.02 R_J.

The different core masses result in different initial radii, with a larger core producing a lower overall planet radius at all times. This behaviour is expected, as the cores are far denser (10 g cm^{-3}) than the average density of the planets in which they reside, thus increasing each planet's average density. This difference, too, continues to 4.5 Gyr, producing a drop in radius of around 0.01 R_J per 10 $M_\oplus$ of core mass. Only three models reach the true radius of Jupiter in 4.5 Gyr: the 30 and 40 $M_\oplus$ core mass models with $Z = 0.01$, and the $40M_\oplus$ core mass model with $Z = 0.02$. Jupiter is believed to have a core mass of between 0 and 18 $M_\oplus$ (Nettelmann, 2011), and a metallicity of $Z = 0.03$ to $Z = 0.13$ (Bagenal et al., 2006). Its potentially higher metallicity would delay cooling in this scenario, resulting in a larger planet at the age of the Solar System if only these factors are taken into account.

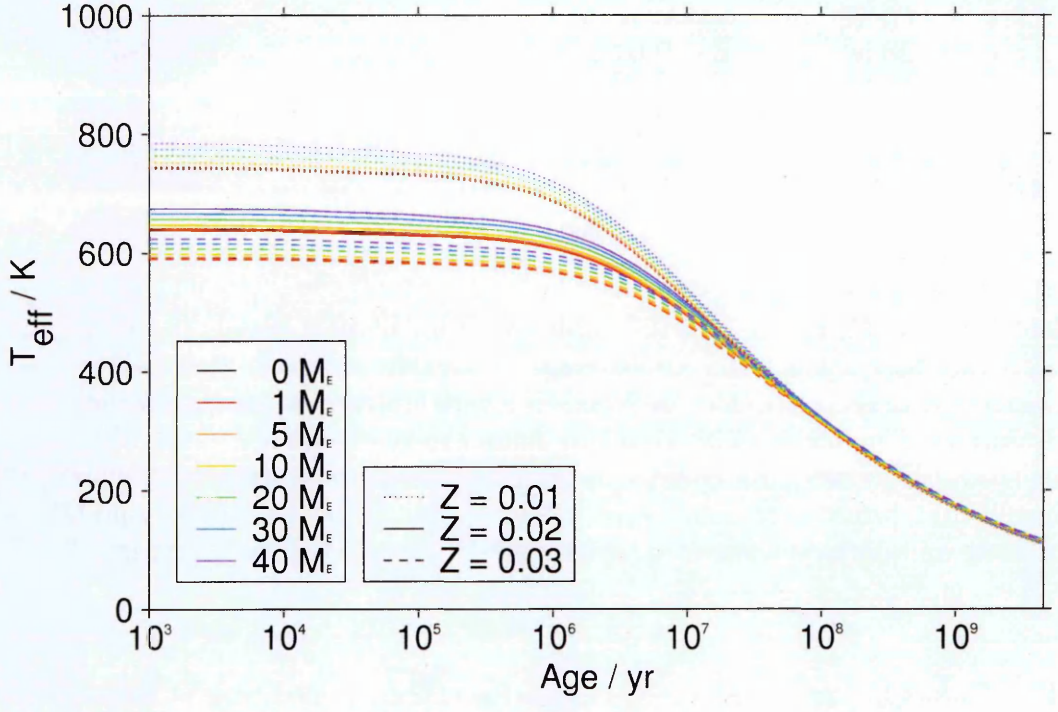

FIGURE 4.4. Comparison of the effective temperature evolution of the core-only planets. Note that the X-axis is logarithmic in order to better display the temporal evolution.

4.2.1.2. *Temperature Evolution.* Figure 4.4 shows the evolution of the effective temperatures T_{eff} of the planets as they evolve. Here it can clearly be seen that the planets are separated mainly by metallicity, rather than core mass. The higher the metallicity, the lower the temperature at early times, though all converge to the same temperature of approximately 115 K by the age of 4.5 Gyr. Planets with higher core mass start out

at higher temperatures, with a maximum initial difference, at a given metallicity, of a few tens of Kelvin. Convergence begins around the age of 10^6 years as the planets begin to cool, and all have converged to almost identical evolutionary tracks between 10^7 and 10^8 years. Before the planets reach 0.1 Gyr in age, they are all but indistinguishable in temperature despite their different initial conditions. Close inspection shows that the higher metallicity planets' T_{eff} decreases slower than that of the low metallicity planets, so that the metallicity order is reversed after around 0.1 Gyr.

Notably, it is clear that regardless of the initial planetary specification, from no core to one of 40 Earth masses, all planets converge to the same temperature to within a few degrees. This degree of convergence implies that the final temperature state of the planet is robust to the initial conditions of both metallicity and core size, and is likely to be highly reproducible.

Since the core does not interact with the external planet, it is not expected to provide a contribution to the ultimate planetary effective temperature, as it can be neither a source nor a sink for heat. The early temperature effect of the core is expected to stem from the way it is added: by first removing an equivalent mass of planetary material from the object early on, then replacing it with an inert object of specified mass and radius (or density). Since all added cores were given the same density of 10 g cm^{-3}, the massive cores occupy proportionally less of the volume of the planet than the mass they are replacing, requiring greater gravitational contraction and subsequent release of heat in the adjustment sequence.

Cooling begins long after the planetary adjustment sequence (not shown on the graph, which displays evolution only from 1,000 years onwards), and is expected to be unaffected by it. The lower metallicity planets begin to cool earlier, and more rapidly, than their higher metallicity counterparts. As the increase in cooling speed is gradual, it is difficult to determine a precise time to designate as the 'start'; however, it is clear that the higher the metallicity, the later a given cooling gradient is reached. The mass of the core has very little effect on the time of cooling, with metallicity being clearly the primary factor.

As the initial heat remaining from formation is radiated away, and the core provides no heat, the means of generation must be gravitational contraction of the planet.

Throughout their lives, these isolated (free from any external influence) gas giant planets simply cool and contract, as is expected. Although these planets are already seen to be somewhat larger than Jupiter at 4.5 Gyr, they are also cooler rather than warmer. Jupiter itself has an average temperature of approximately 125 K (Cole and Woolfson, 2002), which is ten degrees warmer than these evolved planets despite their higher radii, a difference on the order of 8%.

In view of the high degree of convergence between the models, it can reliably be stated that these simple, isolated planetary models, in which only core mass and metallicity are varied and planet-specific factors are not taken into account, do not accurately reproduce the effective temperature of Jupiter. Effective temperature is, however, a robust result against variation of both core mass and metallicity at the age of 4.5 Gyr.

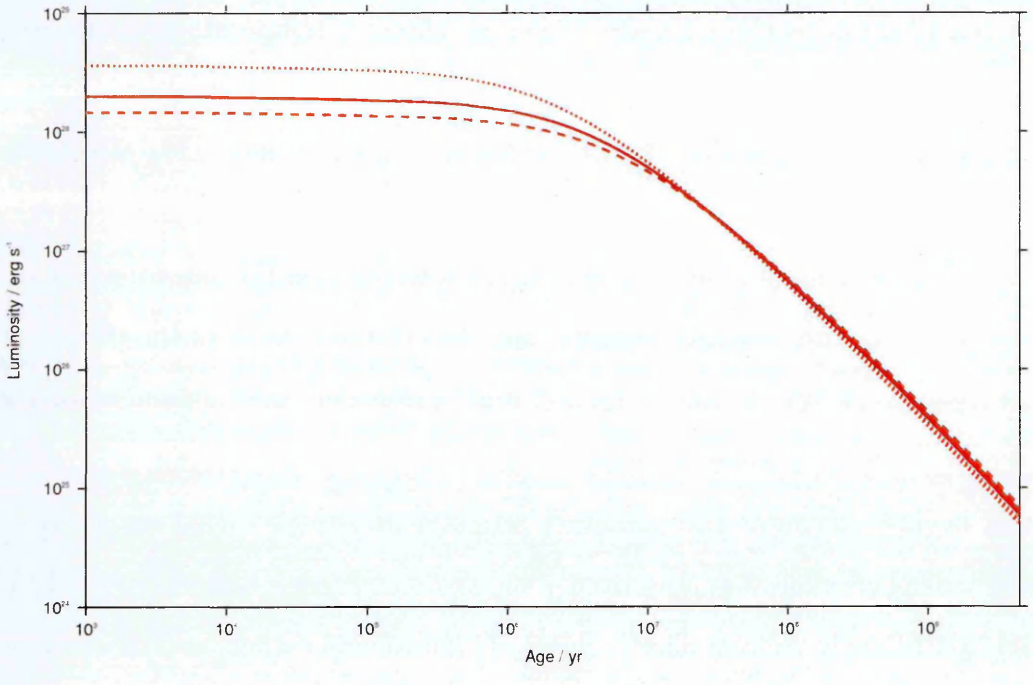

FIGURE 4.5. Comparison of the luminosity evolution of the core-only planets.

4.2.1.3. *Luminosity Evolution.* Figure 4.5 displays the luminosity evolution of the test planets throughout their lifetimes. Almost no variation due to core mass is visible even at late times; the primary difference is between the different metallicity planets. The lower the planetary metallicity, the higher the luminosity at early times; however, these planets' luminosities decrease more rapidly than their higher-metallicity counterparts, so that by the age of 10^8 years, the low metallicity planets are less, rather than

more, luminous. Comparing the radii, temperatures, and luminosities of these planets and recalling the Stefan-Boltzmann law:

$$L = 4\pi R^2 \sigma T_{\text{eff}}^4 \tag{4.2.1}$$

where L is the luminosity, R is the radius, T_{eff} the effective temperature, and σ the Stefan-Boltzmann constant, it is expected that the smaller planets would be somewhat less luminous than their larger counterparts.

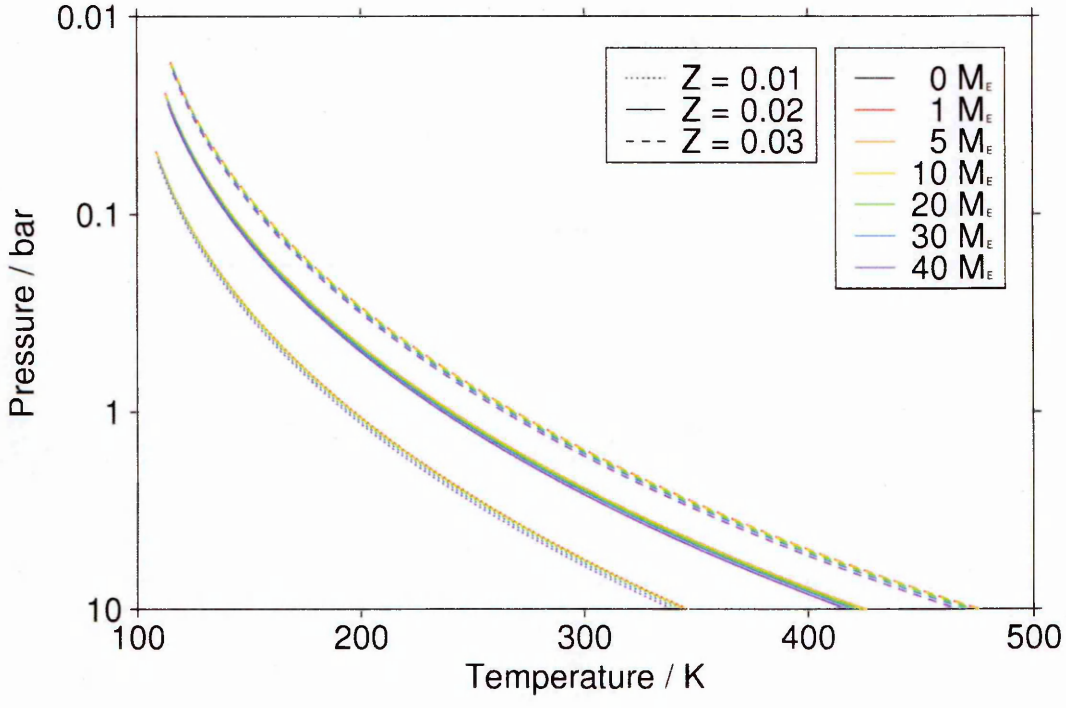

FIGURE 4.6. Comparison of the temperature-pressure profiles of all planets at 4.5 Gyr, from 10 bars to the top of the atmosphere. Models are identified in the same fashion as in previous plots, and the Y-axis is logarithmic in pressure.

4.2.1.4. *Temperature-Pressure Profiles at 4.5 Gyr.* The final temperature-pressure profiles for each model at the age of 4.5 Gyr are shown in Figures 4.6 and 4.7. Although the planets have very similar effective temperatures, the lower metallicity planets have temperatures of up to 100 K lower at a given pressure than their high-metallicity counterparts. Core mass has almost no effect on the final temperature-pressure profiles, with the lowest core mass planets perhaps fractionally warmer, at a given pressure, than the higher core mass ones. All planets at a given metallicity approach essentially the same deep adiabat in the interior, but nowhere do the differing metallicity planets

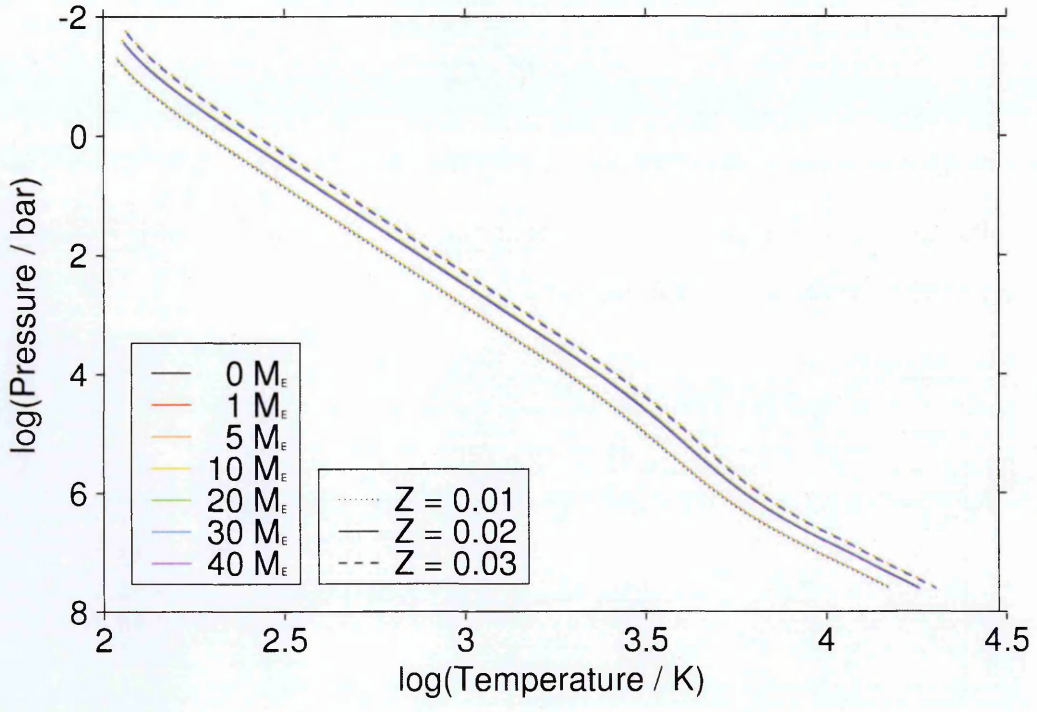

FIGURE 4.7. Comparison of the full temperature-pressure profiles for all planets at 4.5 Gyr.

approach one another: the lower metallicity models are everywhere cooler than their higher metallicity counterparts.

This series of studies on generic, isolated, Jupiter-sized planets does not take into account the effects of irradiation, a quantity vital to the understanding of hot Jupiters. However, they do provide a demonstration that the MESA stellar evolution code performs as expected on giant planets, and serve as a baseline for the study of such planets, as seen below.

4.2.2. Irradiated Jupiter-Mass Planets. Hot Jupiters are, by definition, in receipt of immense amounts of radiation from their parent stars. The typical flux at Mercury, orbiting at 0.39 AU, is 9.1×10^6 erg s^{-1} cm^{-2}, whilst the well-known hot Jupiters HD189733b, HD209458b, and WASP-12b receive, respectively, 4.7×10^8, 9.7×10^8, and 9.4×10^9 erg s^{-1} cm^{-2}. This strong irradiation heats the planets' atmospheres to over a thousand Kelvin, and may be a contributing factor in explaining the inflation of their radii (see, e.g. Arras and Bildsten, 2006). MESA's inbuilt routines for adding external irradiation were tested and run on the varying metallicity and core mass cases of Section 4.2.1. In each case, the saved model with core addition

(if used) completed was taken immediately prior to the main evolution stage, and a new step added to apply an irradiated atmospheric boundary condition, in this case implementing the $T(\tau)$ relation of Guillot (2010), as discussed in Section 4.1.1.4, with a variety of equilibrium temperatures, before continued evolution. As in Guillot (2010), these equilibrium temperatures $T_{\rm eq}$ are determined from planetary distance and stellar type using the relation

$$T_{\rm eq} = T_* \sqrt{\frac{R_*}{2D}} \tag{4.2.2}$$

where T_* is the stellar effective temperature, R_* the radius of the star, and D the orbital separation.

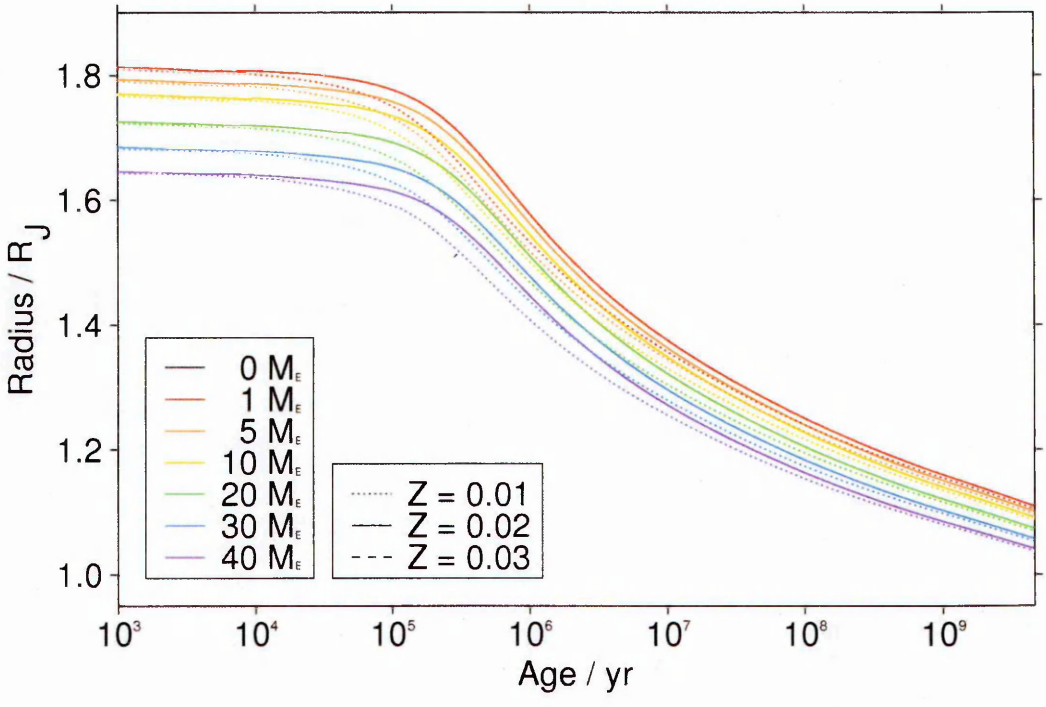

FIGURE 4.8. Comparison plot of the radius evolution of the Jupiter-mass planets with varying core masses, subject to a single value of stellar irradiation resulting in an equilibrium temperature of 1,000 K. For a solar-temperature ($T_{\rm eff}$ = 5780K) star, this corresponds to an approximate distance of 0.07 AU. The x-axis is logarithmic in time to better display the evolution.

4.2.2.1. *Radius Evolution.* While the main focus of this study is to investigate and compare the effects of irradiation, it is also useful to provide direct comparisons to the results previously obtained. Figure 4.8 displays the full suite of models evolved in the previous section, identified in identical fashion. It can immediately be seen from Figure 4.8 that none of the heavily irradiated planets reach Jupiter's radius in

4.5 Gyr, even at high core masses, with the lowest radius reached just under $1.04R_J$ and the highest approximately $1.11R_J$. As before, the lower metallicity planets begin to cool and contract earlier, but the difference at late times between them and their higher metallicity counterparts is less pronounced. The higher irradiation conditions unquestionably lead to larger planets: the lowest radius reached at this time by the non-irradiated planets (shown in Figure 4.3) is just under $0.99R_J$. This difference is similar in magnitude, if smaller, to the spread due to core mass, and the radius ranges of irradiated and non-irradiated planets overlap in the region of high core mass irradiated planets and low core mass non-irradiated planets. Although the planets are larger at the end of evolution, their evolutionary paths follow very similar routes to their non-irradiated counterparts, and no new differences open between those with different metallicities and cores.

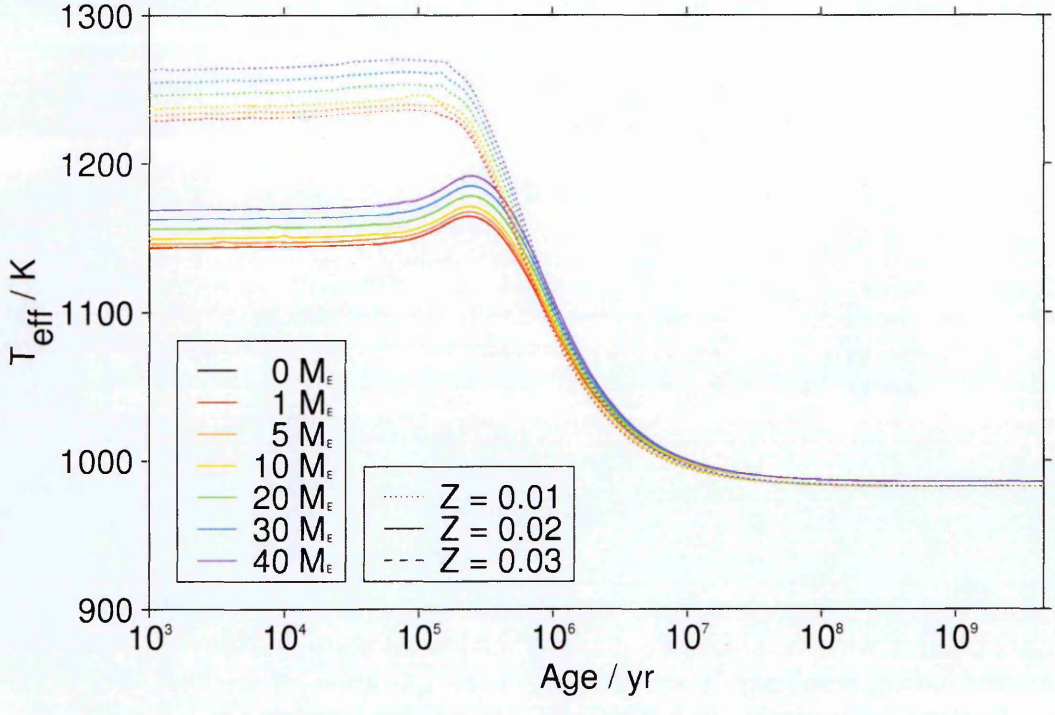

FIGURE 4.9. Effective temperature evolution of the Jupiter-mass planets with varying core masses, subject to stellar irradiation. Dotted lines denote planets with Z=0.01, solid lines planets with Z=0.02.

4.2.2.2. *Temperature Evolution.* Figure 4.9 displays the effective temperatures of the irradiated planets. With added irradiation, the effective temperatures of the planets are much higher at all times than their isolated counterparts. The initial $\approx$ 100 K difference between lower and higher metallicities is maintained, and again, the sets of

planets all converge to very similar final temperatures of approximately 985 K at 4.5 Gyr. Higher core mass planets again start at higher temperatures than the lower core mass planets of identical opacity, but this difference is essentially erased by the time the planets reach 10^7 years. Once again, the lower metallicity planets cool faster and slightly further than the higher metallicity ones, such that they have a marginally lower effective temperature at the end of evolution.

The initial increase in temperature currently shown is an indication that the planets still retain their earlier characteristics from the setup stage, and are undergoing continued adaptation to their new conditions before reaching a smooth cooling curve at around 5×10^5 yr. This is approximately of the same order as the Kelvin time, the relaxation time for departures of the object from thermal equilibrium, which for these models is on the order of 10^6 years at the time radiation is added. The additional energy source forces the planets out of their original, non-irradiated states, requiring them to reach a new equilibrium. Once this is found, evolution continues as normal.

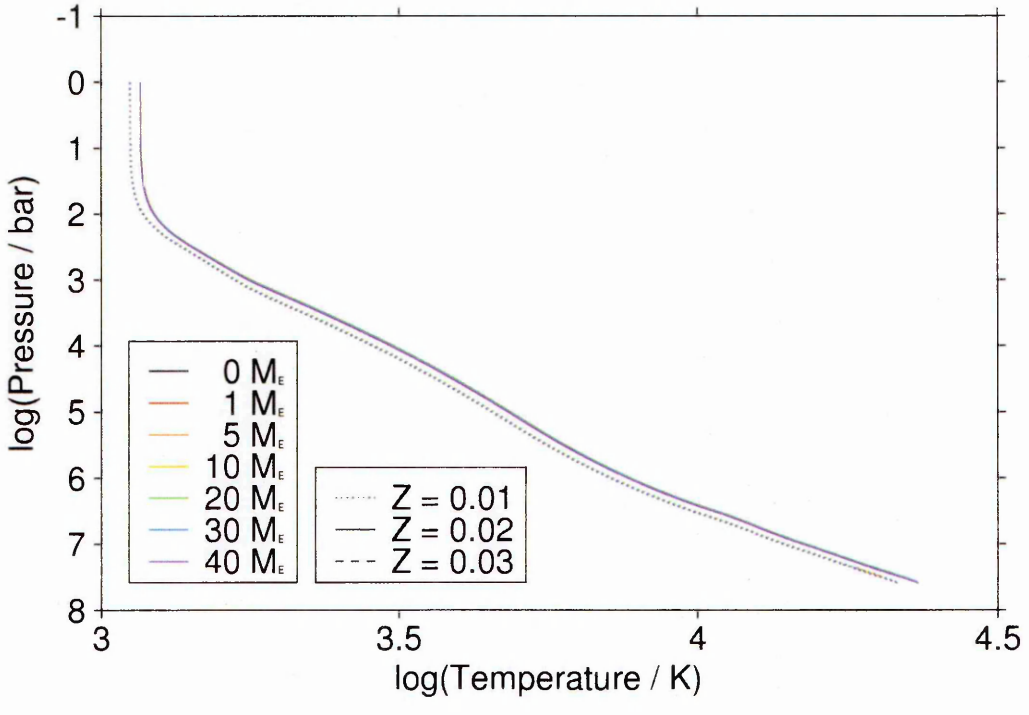

FIGURE 4.10. Full temperature-pressure profiles at 4.5 Gyr for the irradiated planets, covering the entire planetary interior.

4.2.2.3. *Temperature-Pressure Profiles at 4.5 Gyr.* Figure 4.10 shows the full temperature-pressure profiles of the irradiated planets, from the top of the model to the edge

of the core. The base of the atmosphere is here imposed at a pressure of 1 bar in all cases. An isothermal region immediately below this is a basic feature of the atmospheric model, implementing the work of Guillot (2010). The temperature-pressure profiles are essentially identical in shape on a log-log graph, with the lower metallicity planets everywhere cooler than those of higher metallicity. Under these conditions, a 'surface' temperature-pressure plot down to 10 bar such as that of Figure 4.6 displays essentially purely isothermal behaviour. The difference between the different metallicities is less pronounced than that of the non-irradiated planets, and while the final temperatures are similar in magnitude, they are higher at all depths, as expected given that these planets are able to lose less heat.

4.3. Discussion

MESA is found to be successful at modelling the evolution of giant planets without further modification, although it does not reproduce the poorly-understood highest-radius planets. Indeed, these planets, such as HD 209458b, are a subject of ongoing discussion, as discussed in Section 2.3, and are prime candidates for an alternate investigation. It is still unclear what mechanism or mechanisms cause such large radii in these planets, and so it is as expected that MESA has no mechanism that can cause this. An interesting alternate line of enquiry would be to study and attempt to produce physically representative model code for such mechanisms as appear plausible, but this is well outside the scope of this project.

Identical-mass planets modelled at different metallicities and core masses show different radial evolutionary histories, but converge towards similar end results with increasing age. In essence, the long cooling span of these planets serves to blur or eliminate their individual origins, although differences due to metallicity, which is a permanent factor in the composition of the planet, are more pronounced later as compared to core mass, which has less effect as the planet contracts and grows more dense, causing the density contribution of the core to become less relatively significant. The differences in effective temperature at the start have almost completely vanished by around 5×10^7 years, and all planets, whether irradiated or otherwise, remain at very similar effective temperatures thereafter.

On irradiation, the effect of metallicity on the final radius is reduced. The planets cool more slowly, as the incoming energy is added to the planetary budget with the overall effect of retaining more energy later. However, the final effective temperature is now slightly lower for the lower-metallicity planets, as such an atmosphere is more transparent to incoming and outgoing radiation.

It is shown to be possible to fine-tune the setup characteristics of a model to reproduce a specific planet. However, even with the final radius, the mass, and irradiation all specified by observation, metallicity and core mass are degenerate to a certain extent, and further parameters are also available for variation. This degeneracy notwithstanding, it is still possible to constrain the parameters of any given planet, particularly if the assumption of the simplest possible setup is made. Irradiation and mass are

always uniquely constrained by knowledge of the planet to be modelled, provided it is transiting.

It is also possible to identify sections of the planetary profile more closely by their disparate properties. Radiative and convective zones (zones which are dominated by one or the other as a means of energy transport) for example, can be picked out using model flags or simply through inspection: convection occurs where the true temperature gradient is greater than the adiabatic temperature gradient. While the isolated planets are all purely convective, the irradiated ones have an outer radiative layer, where radiation rather than convection is the primary means of conveying energy through the structure. The composition is also available throughout the model profile, although it is less striking compared to the evolution of a star, which fuses its lighter elements into heavier ones, a planet's overall composition does not change.

CHAPTER 5

Connecting the Interior and Neutral Atmosphere

This chapter investigates the potential for overlap of atmospheric and interior modelling, since the atmospheres and interiors of exoplanets are of necessity codependent. The two different types of model cannot be directly interlinked: three-dimensional atmospheric modelling covers processes that occur on a short timescale, and typically covers periods on the order of no more than hundreds of days; one-dimensional interior modelling of necessity parametrises these short-period processes into a vastly simplified version that is able to be modelled without too great a computational demand over periods of billions of years. To that extent, it may thus seem that the two types of model are fundamentally incompatible. However, instead of directly computationally linking the models, it is feasible to derive information from the output of one model for use in the setup of the other, providing information on the boundary conditions or other parameters of use to the run. The goal of this study is to investigate to what extent that is the case under current limitations.

This work finds that it is both plausible and potentially useful to utilise information derived from an interior model to constrain the conditions of the atmospheric problem.

The potential for the dependence of PUMA on selected MESA output conditions is investigated in Section 5.1. The potential for PUMA results to inform the outer boundary condition of MESA models is investigated in Section 5.2. Section 5.3 studies the result of using interior, then atmospheric modelling to study the known hot Jupiters HD 209458b, HD 189733b, WASP-12b, WASP-7b, and WASP-46b. Finally, Section 5.4 brings together and analyses the observed results.

5.1. The Atmosphere as Influenced by the Interior

Processes occurring in the deep interior of a planet operate on vastly different timescales to those high in its atmosphere. Even in Earth-based atmospheric modelling, coupling an atmospheric model to an oceanic model is extremely difficult, requiring extreme simplification of one of the two components. However, just as with the ocean and atmosphere of Earth, the interior of a gas giant will affect its outermost layers.

The MESA runs described in Chapter 4 provide the basis for a suite of PUMA runs positioned at various points in planetary evolution. Since modelling migration is beyond the scope of this project, the planets are assumed to have migrated early in their evolution and then reside in the same orbit throughout. Migration is typically expected to take place on the order of roughly 10^5 years or less (Baruteau and Masset, 2013), a similar timescale to that required for MESA to adapt to changed irradiation conditions, rendering this assumption believeable. Suites of PUMA runs are set up based on the MESA planets at both late and early times, choosing sample planets of selected masses and core sizes in order to cover the available parameter space most efficiently.

In the following section, the suite of planets irradiated to a T_{eff} of 1,000 Kelvin are investigated. These planets are given a correspondingly slower rotation rate of 6 days to reflect the likelihood that they are further from their stars. While it is also possible that the host star may be significantly dimmer, this is essentially unconstrained in this study. To reflect the decreased irradiation, the difference between the equatorial and pole forcing temperatures is also reduced to 200 Kelvin. In each case, the gravity, surface temperature, and radius of the planet are specified by the MESA parent model in question. All base models are

Designation	Metallicity	Core Mass / $M_\oplus$
m01c01	Z = 0.01	1
m01c10	Z = 0.01	10
m02c01	Z = 0.02	1
m02c10	Z = 0.02	10
m03c10	Z = 0.03	10

TABLE 5.1. Table of runs used by the atmospheric models and the corresponding short run designations.

As in Chapter 3, temporally averaged horizontal diagnostics are produced on sigma levels, as well as temporally averaged zonal mean diagnostics. Though they differ in

scale, with the maximum temperature contrast only 100K and the standard deviation correspondingly reduced, the diagnostics on the level $\sigma = 0.7$ are essentially visually identical to those produced during the intercomparison study of Chapter 3.

Figures 5.1, 5.2, 5.3, 5.4, and 5.5 thus show the mean and standard deviation of temperature at the higher level $\sigma = 0.37$, corresponding to a pressure of roughly 370 mbar and closer to where radiation is likely to emerge from the atmosphere. The distinctive chevron shape produced in the lower atmosphere is no longer as apparent at this altitude, with the superrotating jet supporting a cool equator and a pair of hotspots to either side, centred in all cases at roughly ±50° N, 170° E. The temperature variation is also much lower, covering a range of less than 100 Kelvin in all cases, and the standard devation is on the order of 10 Kelvin. The substellar point is here at (0,0), but the coolest point at this level is now at −80° E, more than 90° offset from the location of the 'cold spot' in the forcing.

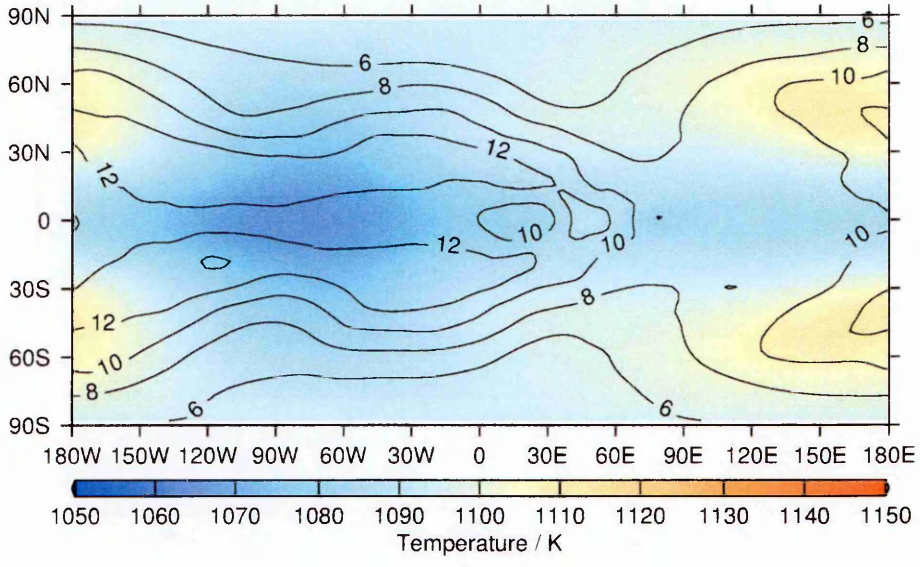

FIGURE 5.1. Temperature mean (colour) and standard deviation (contour) at $\sigma = 0.37$ for the 1% metallicity, $1M_\oplus$ core mass planet.

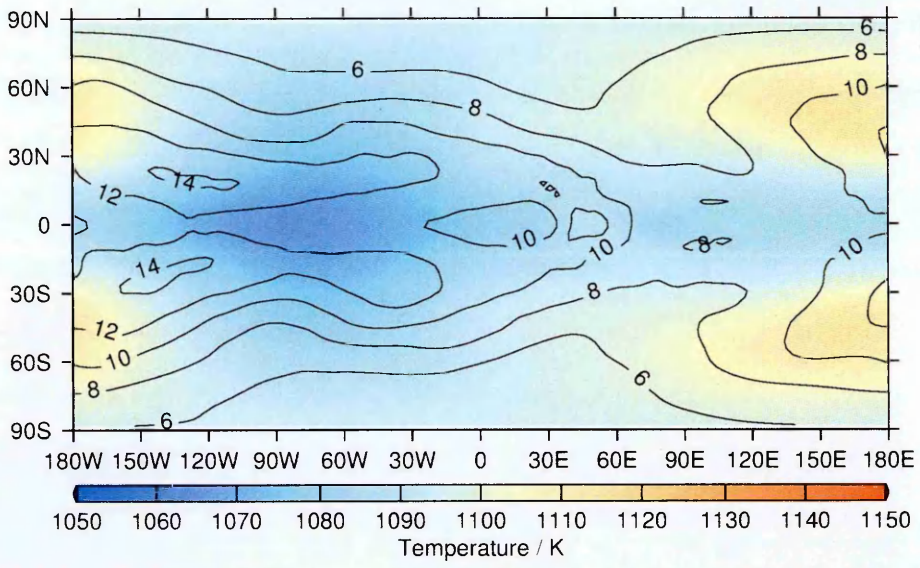

FIGURE 5.2. Temperature mean (colour) and standard deviation (contour) at $\sigma = 0.37$ for the 1% metallicity, $10M_\oplus$ core mass planet.

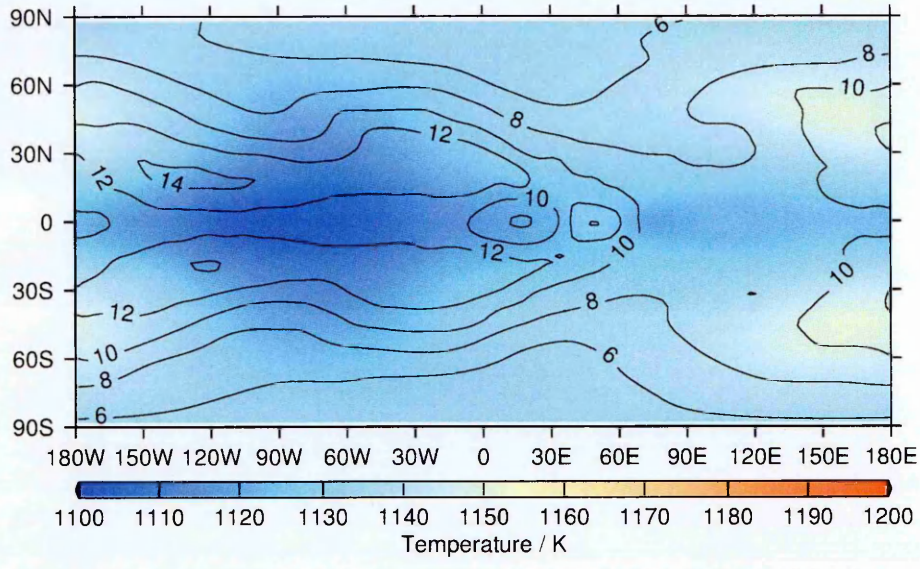

FIGURE 5.3. Temperature mean (colour) and standard deviation (contour) at $\sigma = 0.37$ for the 2% metallicity, $1M_\oplus$ core mass planet.

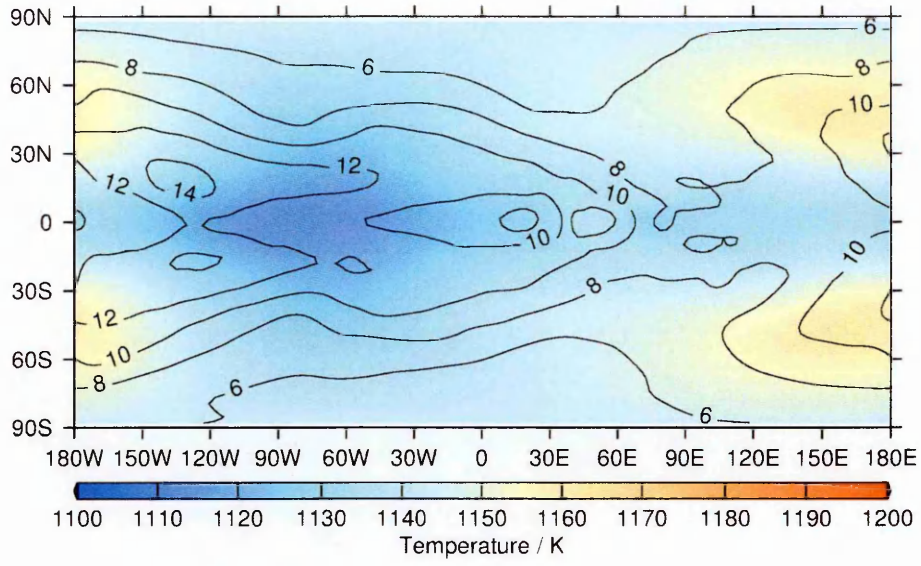

FIGURE 5.4. Temperature mean (colour) and standard deviation (contour) at $\sigma = 0.37$ for the 2% metallicity, $10M_\oplus$ core mass planet.

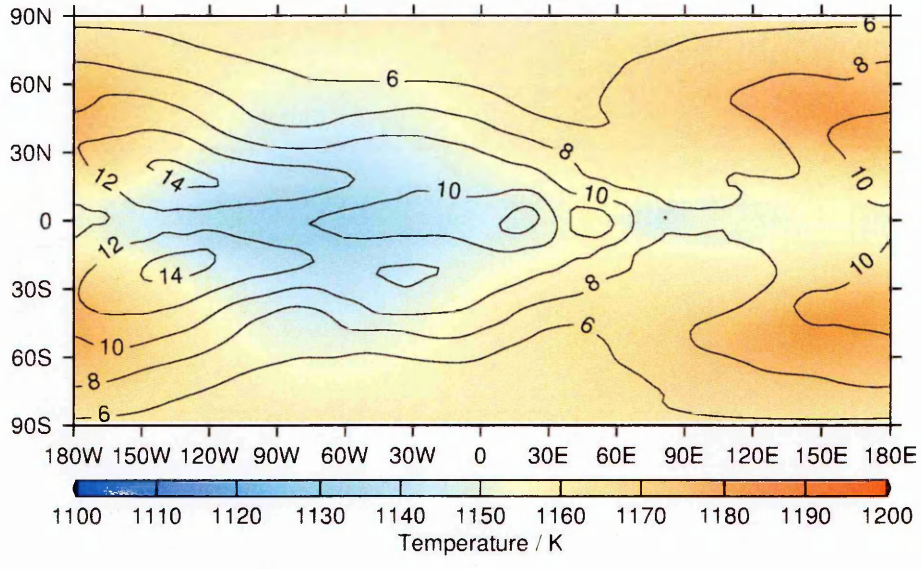

FIGURE 5.5. Temperature mean (colour) and standard deviation (contour) at $\sigma = 0.37$ for the 3% metallicity, $10M_\oplus$ core mass planet.

Figures 5.6, 5.7, 5.8, 5.9, and 5.10 demonstrate the temporally averaged zonal mean temperatures for the different planets. The warmest temperatures occur in a band between roughly $\sigma = 0.7$ and $\sigma = 0.4$, with a dip in the pattern at the equator, where the peak temperatures are found at around $\sigma = 0.9$. The greatest variability is found over the poles and low in the atmosphere in the equatorial region. Although heating plots are not shown here, they can quite simply be deduced from inspection by comparison of the plotted temperatures with a simple vertical temperature distribution decreasing with altitude (beginning at the run-specific surface temperature and following a curve similar to that of Figure 3.2). In general, they are very similar to one another, with cooling (the model temperatures are warmer than the forcing) over the equator and in the mid-altitudes on either side, and heating elsewhere.

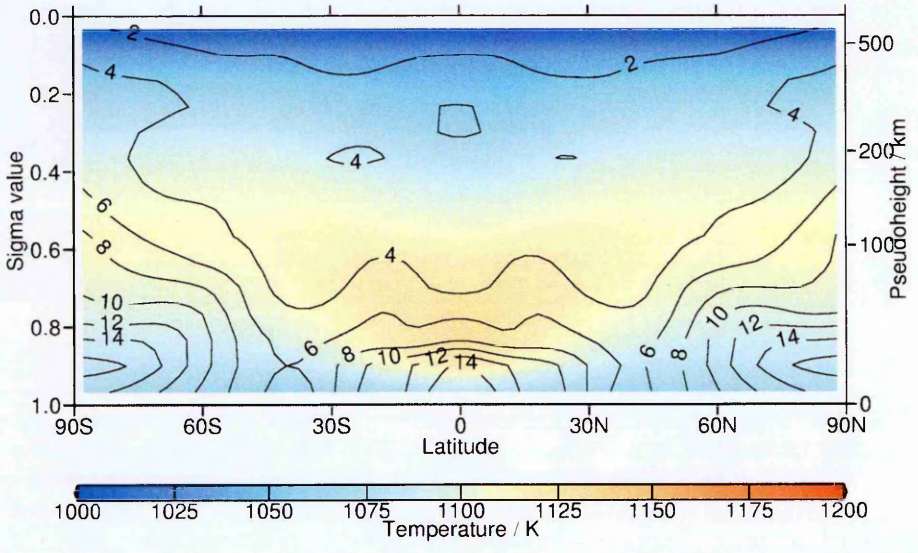

FIGURE 5.6. Temporally averaged zonal mean temperature (colour) and standard deviation (contour) for the 1% metallicity, $1M_{\oplus}$ core mass planet.

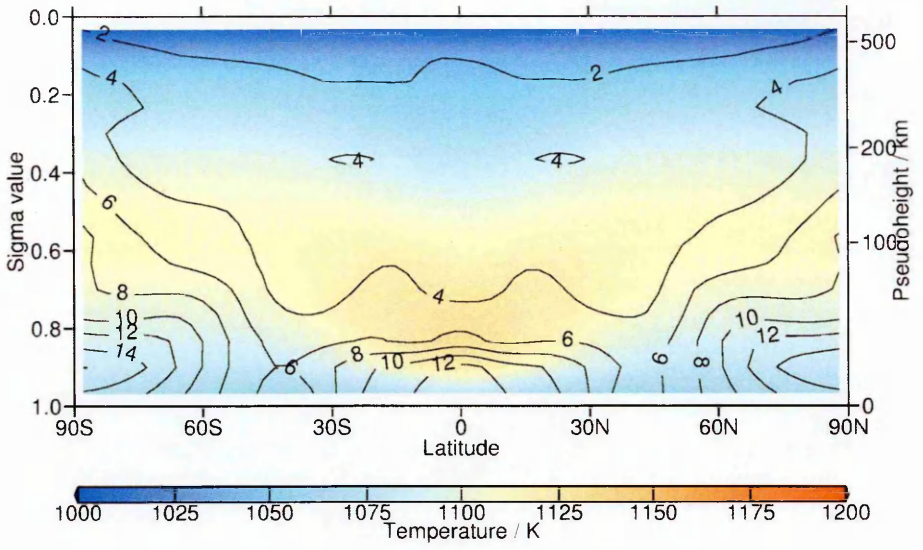

FIGURE 5.7. Temporally averaged zonal mean temperature (colour) and standard deviation (contour) for the 1% metallicity, $10M_{\oplus}$ core mass planet.

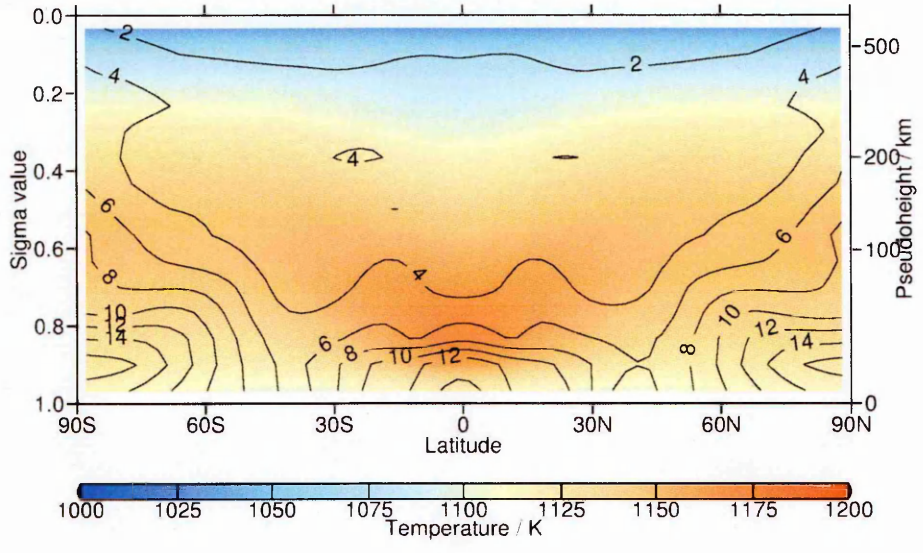

FIGURE 5.8. Temporally averaged zonal mean temperature (colour) and standard deviation (contour) for the 2% metallicity, $1M_{\oplus}$ core mass planet.

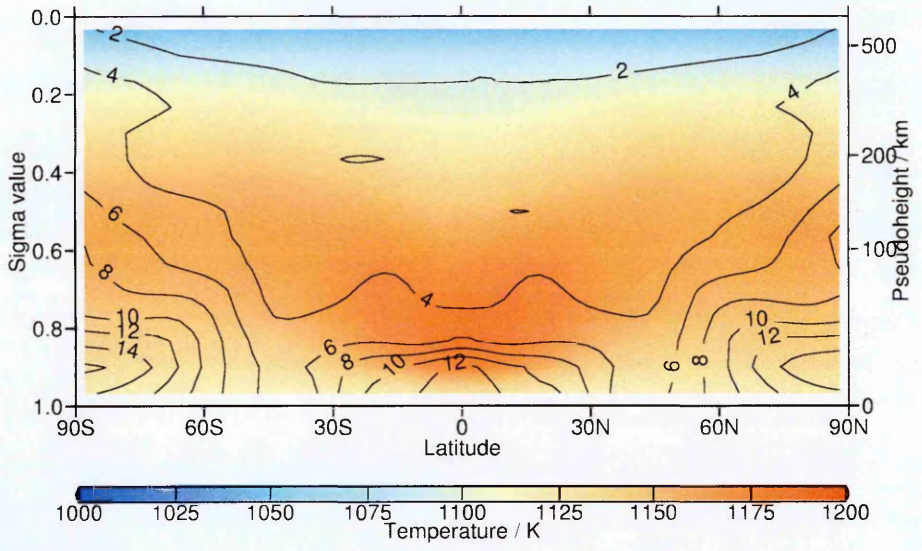

FIGURE 5.9. Temporally averaged zonal mean temperature (colour) and standard deviation (contour) for the 2% metallicity, $10M_{\oplus}$ core mass planet.

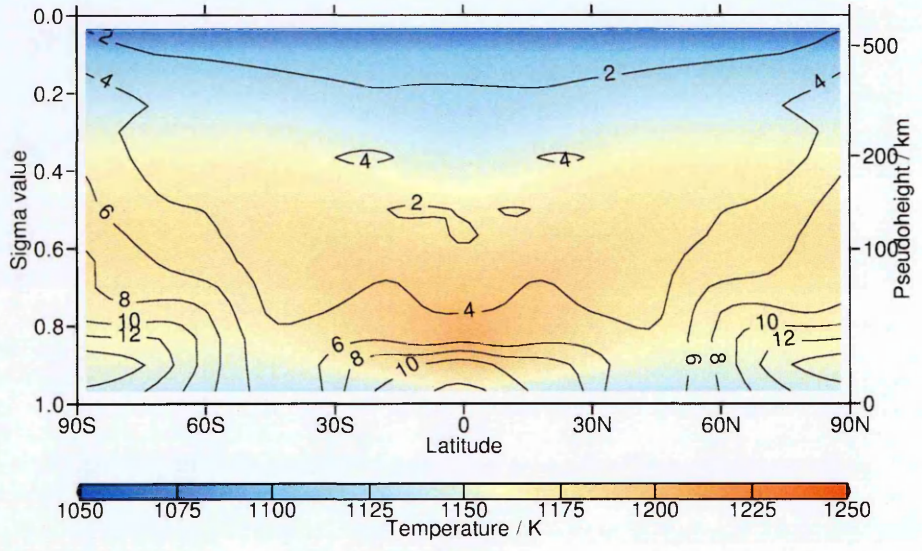

FIGURE 5.10. Temporally averaged zonal mean temperature (colour) and standard deviation (contour) for the 3% metallicity, $10M_{\oplus}$ core mass planet.

Figures 5.11, 5.12, 5.13, 5.14, and 5.15 display the time-averaged zonal mean zonal wind for each planet. In each case a superrotating jet is clearly apparent, reaching speeds of almost 500 m s^{-1}, but it does not descend deep into the atmosphere and is largely closed at the bottom of the model. By contrast, the weaker return flow of gas from the nightside to the dayside, surrounding the jet, is not so bounded, with westward velocities above 100 m s^{-1} at the base of the model between $\pm 30° - 60°$ N in all cases. The lower metallicity planets also demonstrate a strong return flow at high altitude above the superrotating jet, as seen in, for example, Figure 5.12, a feature less apparent in higher-metallicity, warmer planets such as that in Figure 5.15.

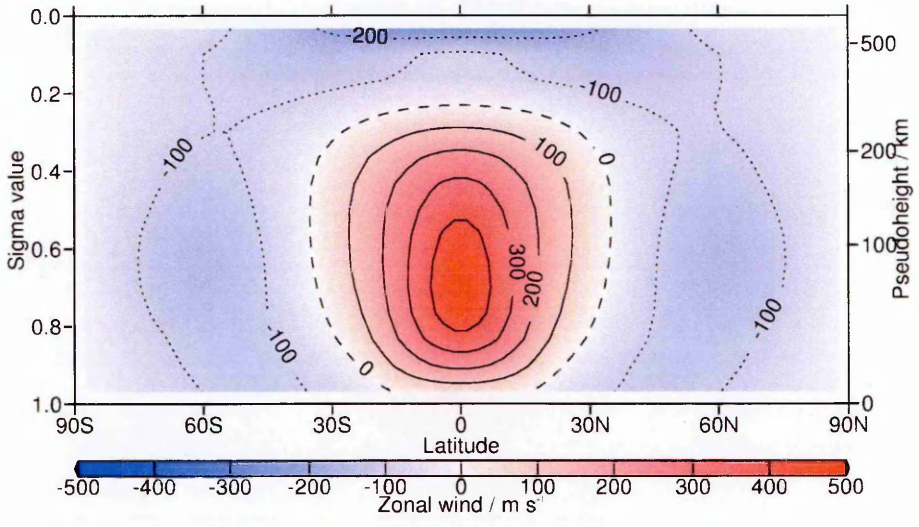

FIGURE 5.11. Temporally averaged zonal mean zonal wind for the 1% metallicity, $1M_\oplus$ core mass planet. Solid lines indicate eastward wind (out of the page); dotted lines indicate westward wind.

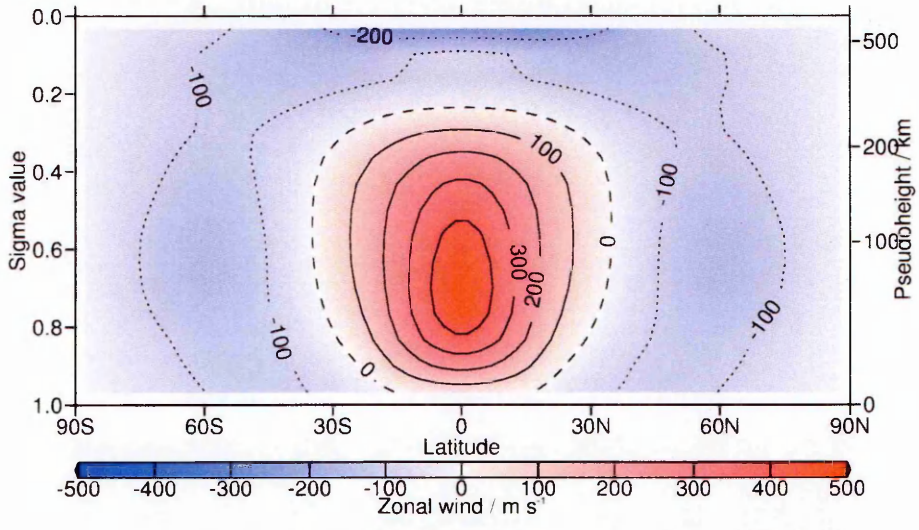

FIGURE 5.12. Temporally averaged zonal mean zonal wind for the 1% metallicity, $10M_\oplus$ core mass planet. Solid lines indicate eastward wind (out of the page); dotted lines indicate westward wind.

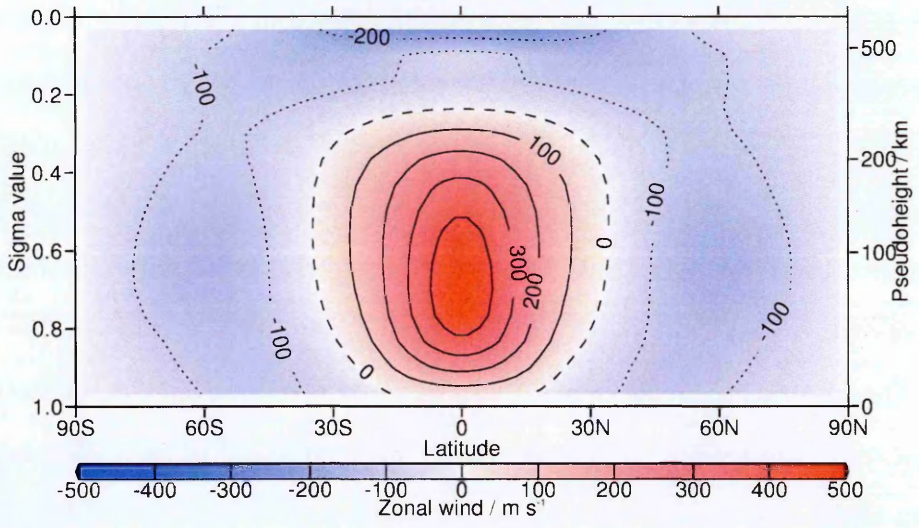

FIGURE 5.13. Temporally averaged zonal mean zonal wind for the 2% metallicity, $1M_{\oplus}$ core mass planet. Solid lines indicate eastward wind (out of the page); dotted lines indicate westward wind.

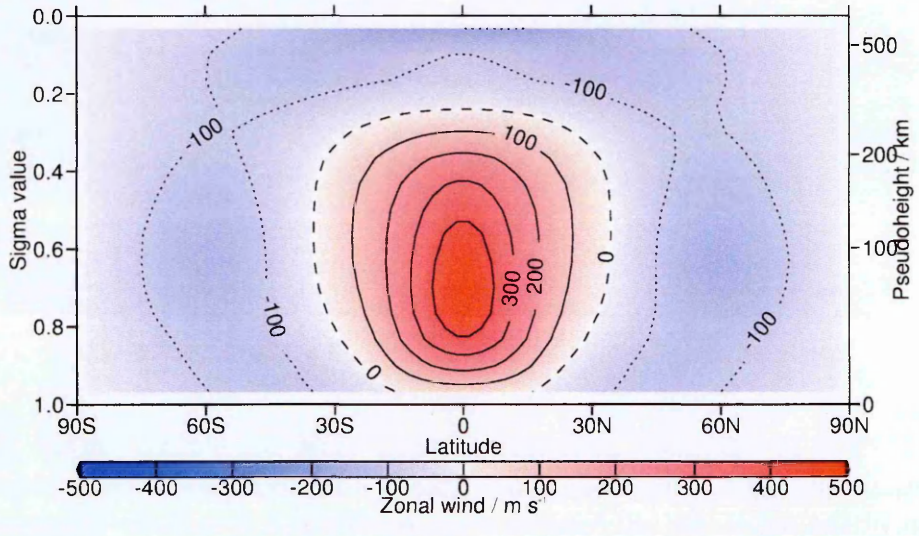

FIGURE 5.14. Temporally averaged zonal mean zonal wind for the 2% metallicity, $10M_{\oplus}$ core mass planet. Solid lines indicate eastward wind (out of the page); dotted lines indicate westward wind.

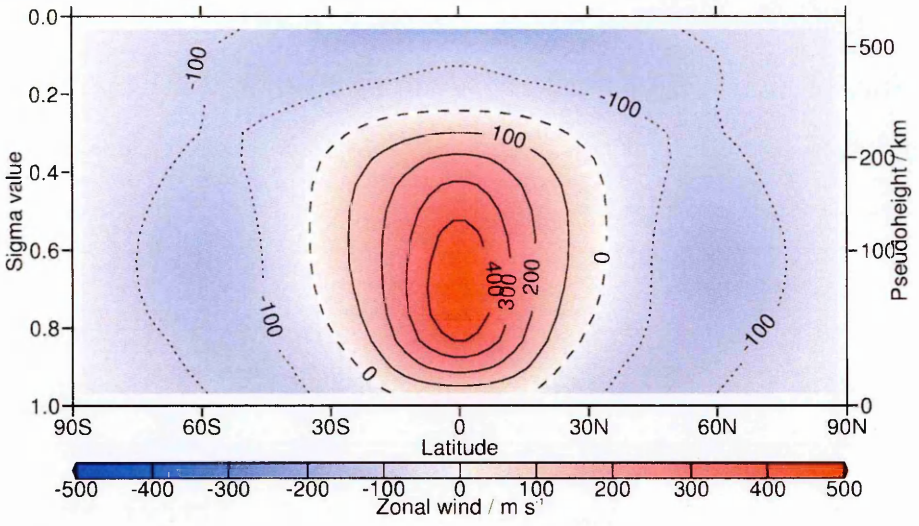

FIGURE 5.15. Temporally averaged zonal mean zonal wind for the 3% metallicity, $10M_{\oplus}$ core mass planet. Solid lines indicate eastward wind (out of the page); dotted lines indicate westward wind.

The meridional circulation is very similar for all planets, as demonstrated by the close similarity of Figures 5.16 and 5.17. A pair of small overturning cells exist below $\sigma = 0.6$ and between $\pm 30°$ latitude, with air sinking over the equator and rising at $\pm 30°$ The rest of the atmosphere occupied by a larger pair that rotate in the opposite sense, with air rising over the equator and sinking towards the poles. This pattern, while common to all of these simulated planets, is distinctly different to that observed in Section 3.2.1.

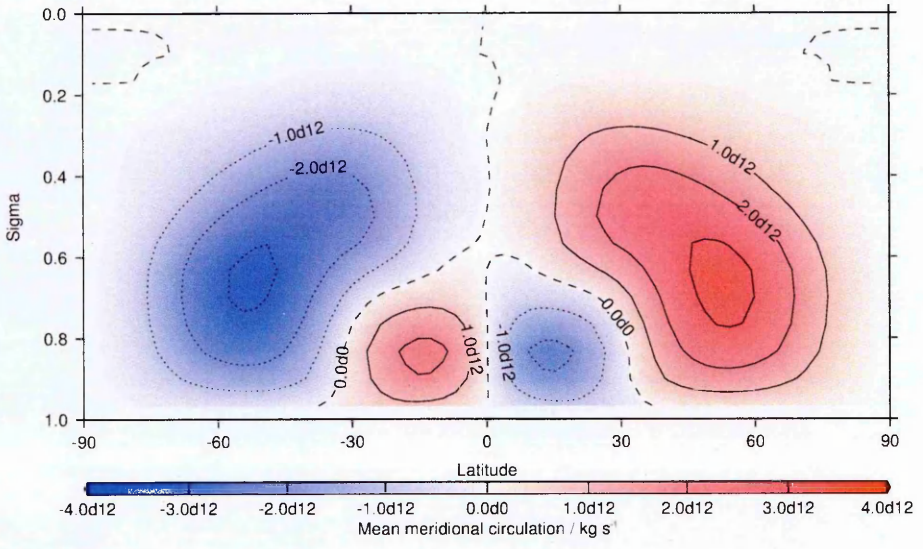

FIGURE 5.16. Temporally averaged mean meridional circulation for the 2% metallicity, $10M_\oplus$ core mass planet. Positive (solid) contours indicate clockwise circulation, negative (dotted) the opposite.

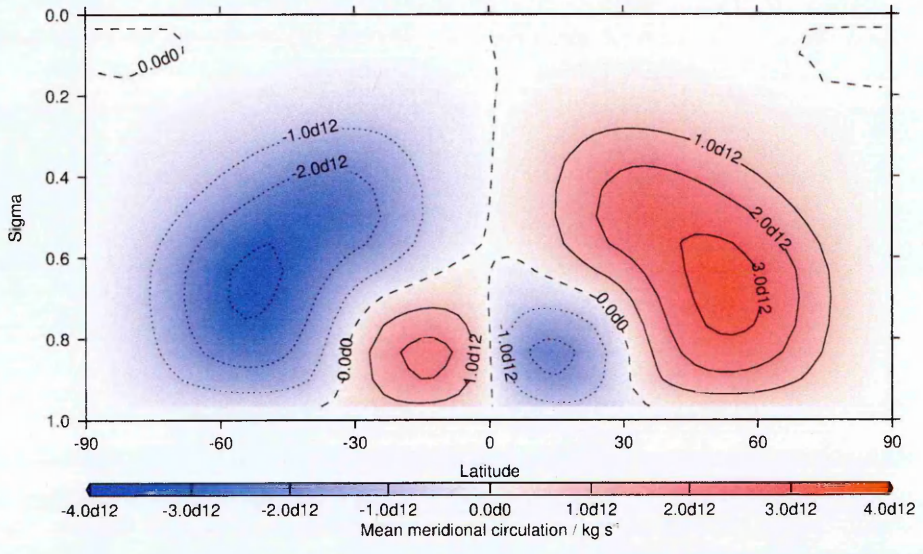

FIGURE 5.17. Temporally averaged mean meridional circulation for the 3% metallicity, $10M_\oplus$ core mass planet. Positive (solid) contours indicate clockwise circulation, negative (dotted) the opposite.

When observed over the course of a model run, the winds follow a chaotic yet predictable pattern. Though the variability at any moment is unpredictable, the overall

variation of the global circulation passes repeatedly through essentially similar cycles. Initially, the equatorial jet will be strong and almost straight, as illustrated in the initial snapshot of Figure 5.19, and the wind and temperature states smooth and almost equatorially symmetrical. Over the following six or seven planetary days, a pair of large vortices form and grow (upper-right image, particularly of Figure 5.20, until the vortices and to an extent the equatorial jet itself disrupt. The jet resumes its initial position over the next few planetary days, finally returning to an almost equatorially symmetric state from which the process begins again. The full sequence is illustrated in Figures 5.18 (temperature), 5.19 (wind), and 5.20 (vorticity), and returns to a state similar to its initial configuration after roughly 15 planetary days. This series of events, taking place over multiple days and thus multiple orbits, will potentially produce different patterns from orbit to orbit if the planet's temperature or winds are being observed.

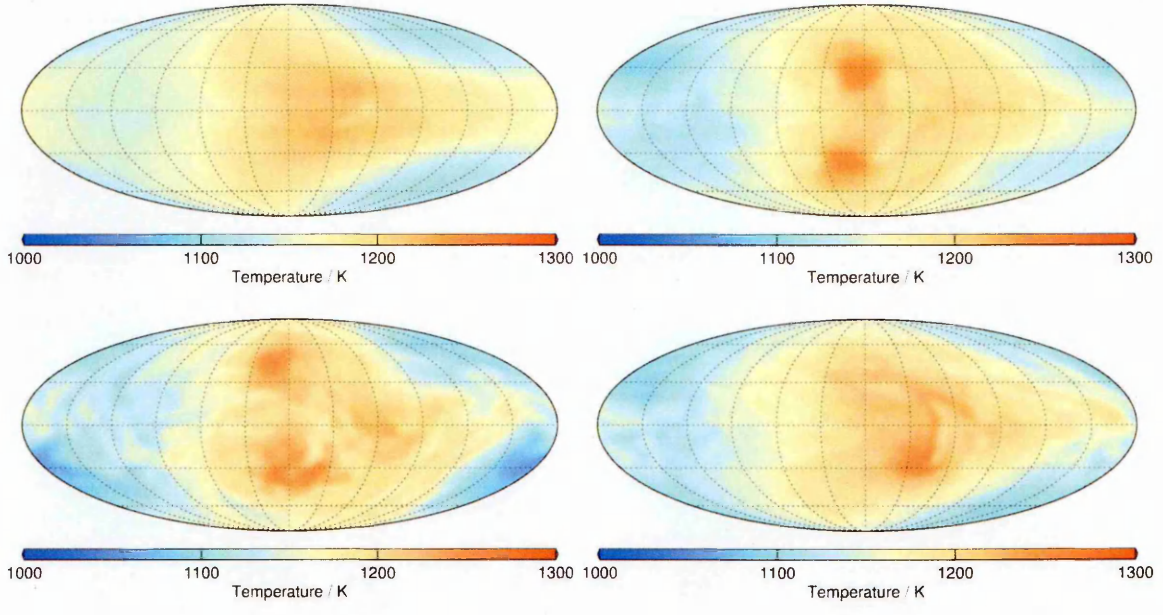

FIGURE 5.18. $\sigma = 0.7$ temperature plots at a point following run stabilisation. Left to right: the temperature at the beginning, arbitrarily designated (planetary) Day 1; the temperature at Day 6; Day 7; and Day 10, at which point the circulation is growing calmer again.

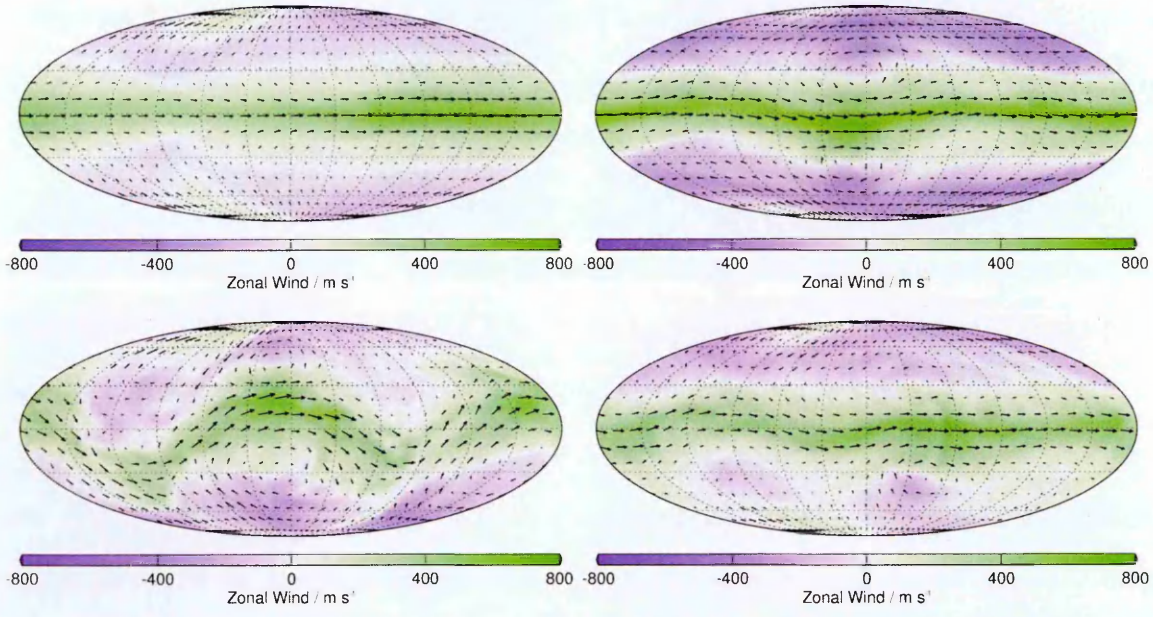

FIGURE 5.19. $\sigma = 0.7$ vector wind (arrows) and zonal component (colour) at a point following run stabilisation. Left to right: the wind at the beginning, arbitrarily designated (planetary) Day 1; the wind at Day 6; Day 7; and Day 10, at which point the circulation is growing calmer again.

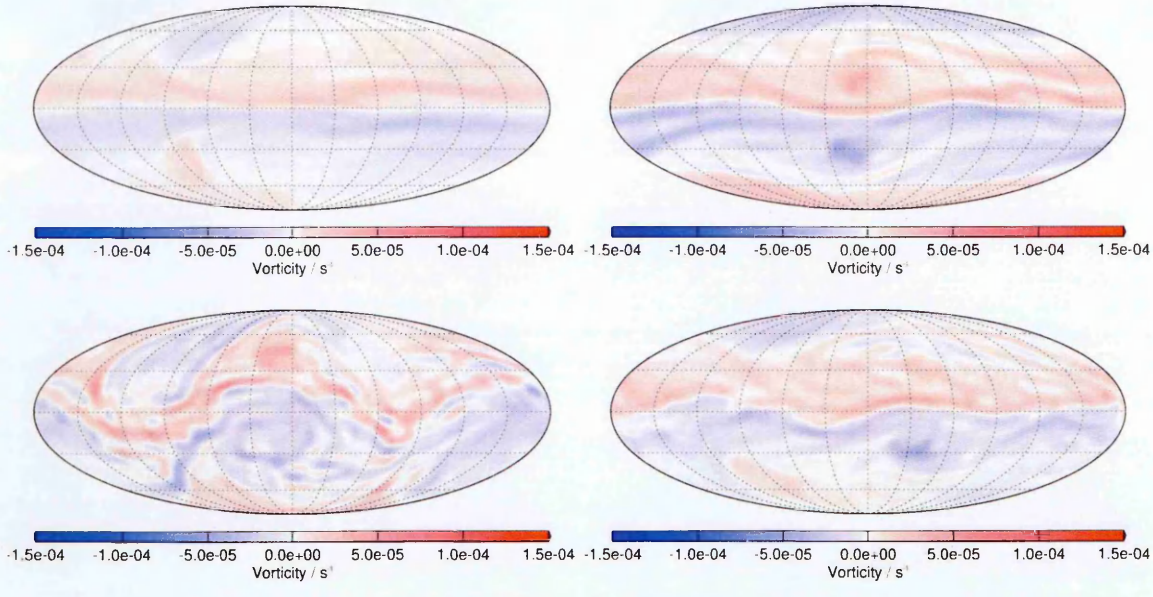

FIGURE 5.20. $\sigma = 0.7$ vorticity at a point following run stabilisation. Left to right: the vorticity at the beginning, arbitrarily designated (planetary) Day 1; the vorticity at Day 6; Day 7; and Day 10, at which point the circulation is growing calmer again.

5.2. Insight into the Interior from the Atmosphere

The atmospheric model runs described in Chapter 3 are analysed to provide the outer boundary conditions for a suite of MESA runs. These runs utilise base models from the parameter space sweep of Chapter 4 as a starting point, and apply a suitable irradiation to the atmosphere, as discussed in Chapter 4, Section 4.1.1.4. The base of the model atmosphere is fixed at the base pressure of PUMA, 1 bar, and uses the PUMA temperatures, which are modified by atmospheric circulation.

The age of the star HD 209458 is approximately 4 ± 2 Gyr (Schneider, 1995-2015). With this wide range of potential ages available, an evolution age of 4.5 Gyr was chosen to facilitate direct comparison with previous MESA model runs. As MESA chooses the length of each model timestep dynamically, adjusting it to a value appropriate for the difficulty with which a solution may be found, the records it produces are somewhat arbitrarily spaced in time. As a result, direct record-to-record comparison cannot be guaranteed throughout the planet's evolution save at fixed ages specified on intialisation.

Due to the limited availability of compatible variables, this experiment set the fixed outer boundary condition $T_{\rm eff}$ equal to the average temperature at the base of the PUMA intercomparison model run, approximately 1,550 K. The expected temperature from a simple calculation of the flux at the planet,

$$T_{\rm eq} = T_\star \sqrt{\frac{R_\star}{2D}}$$

where $T_{\rm eq}$ is the equilibrium temperature of the planet, $T_\star$ is the effective temperature of the star, $R_\star$ is the radius of the star, and D is the distance between the star and planet. For the case of HD 209458, $T_\star = 6{,}092$ K, $R_\star = 8.35 \times 10^8$ m, and $D = 7.10 \times 10^9$ m, resulting in a predicted $T_{\rm eq}$ of 1,500 K.

Two of these model investigations are highlighted below.

5.2.1. Irradiation Investigation. The two models chosen, adjusted to this high irradiation value, and evolved to 4.5Gyr are the *m02c10* model investigated in Chapter 4, which is a Jupiter-mass planet with a ten Earth-mass core and a metallicity of Z = 0.02, and a coreless model of the same metallicity and a mass identical to that of HD 209458b, $0.69 M_{\rm J}$.

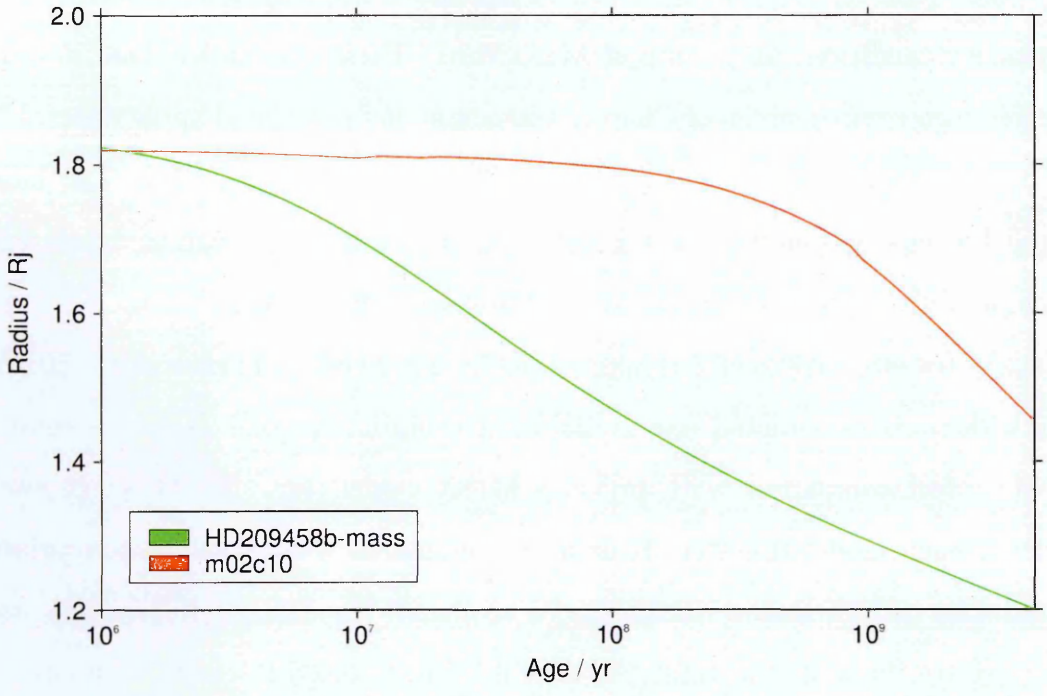

FIGURE 5.21. Plot of the radial evolution of the two models with T_{eff} = approximately 1,550 K.

Figure 5.21 shows the radial evolution of the two planets compared with one another. The slight 'wobble' effect up to and around 10^7 yr for the *m02c10* model is caused by model adjustment to the new irradiation values. Irradiation to this degree proved relatively difficult to simulate successfully, and the second model, a coreless HD 209458b-mass planet, was required to go through additional adjustment steps prior to 10^6 yr.

The *m02c10* planet has only shrunk to 1.02×10^8 m, or 102,000 km, which is approximately $1.46R_{\text{J}}$, by the age of 4.5 Gyr. The lower-mass coreless planet begins to shrink rapidly much earlier in its evolution, reducing to $1.2R_{\text{J}}$ at the age of 4.5 Gyr.

HD 209458b, the planet on which the atmospheric intercomparison test was based, has a radius of $1.38 \pm 0.018R_J$ (Schneider, 1995-2015), or $9.65 \times 10^7 \pm 1.3 \times 10^7$ m. The increased effective temperature tends to produce a larger radius, as the planet cannot lose energy as efficiently. In the case of the *m02c10* planet, its inert core counterbalances this effect to an extent, but not sufficiently to render it smaller than HD 209458b. Despite the intense irradiation and its lack of a core, however, the planet of HD 209458b's mass shrank to just $1.2R_{\text{J}}$, outside the error bars on the radius of HD 209458b.

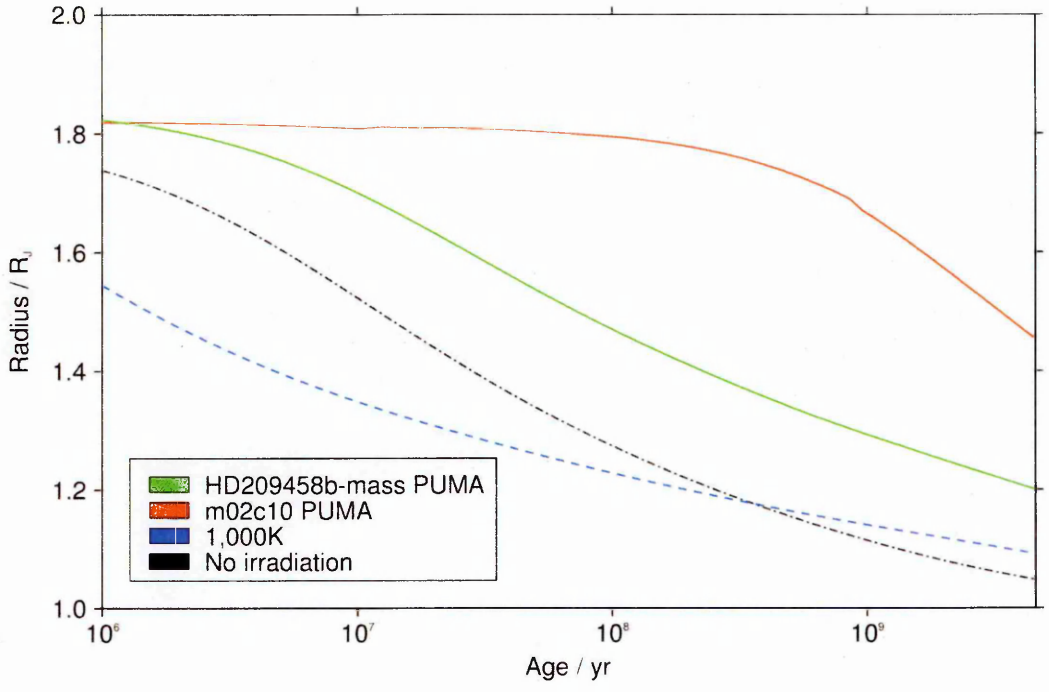

FIGURE 5.22. Comparison of the radius evolution of the HD 029458b-mass planet and the model m02c10 under different irradiation conditions.

Figure 5.22 displays the radius evolutionary profiles previously discussed together with those of other versions of the *m02c10* model, permitting direct comparison. Without irradiation, the radius of the *m02c10* planet (a planet created from the same initial model) decreased to just over $1R_J$ at the final age of 4.5 Gyr. By comparison, despite beginning to decrease in radius more rapidly at early times (see discussion in Chapter 4, Section 4.2.2), the same planet irradiated to a $T_{\rm eff}$ of 1,000 K reached a radius of closer to $1.1R_{\rm J}$ at this age. Though different, these two are much closer together than their next neighbour on this plot, the $1.2R_{\rm J}$ HD 209458b-mass planet. The greatest difference, however, is between any of the three models just mentioned and the highly-irradiated *m02c10* model, which ends its evolution at a radius of $1.4R_{\rm J}$.

The extremely late radius decrease of the highly irradiated *m02c10* model may be partially due to difficulties in the model adjustment. This model proved rather difficult to produce, and sensitive to even small changes in conditions: alterations on the order of 5% in the irradiation temperature during the setup stage produced models that failed to converge, indicating that it is not a robust model with the setup used.

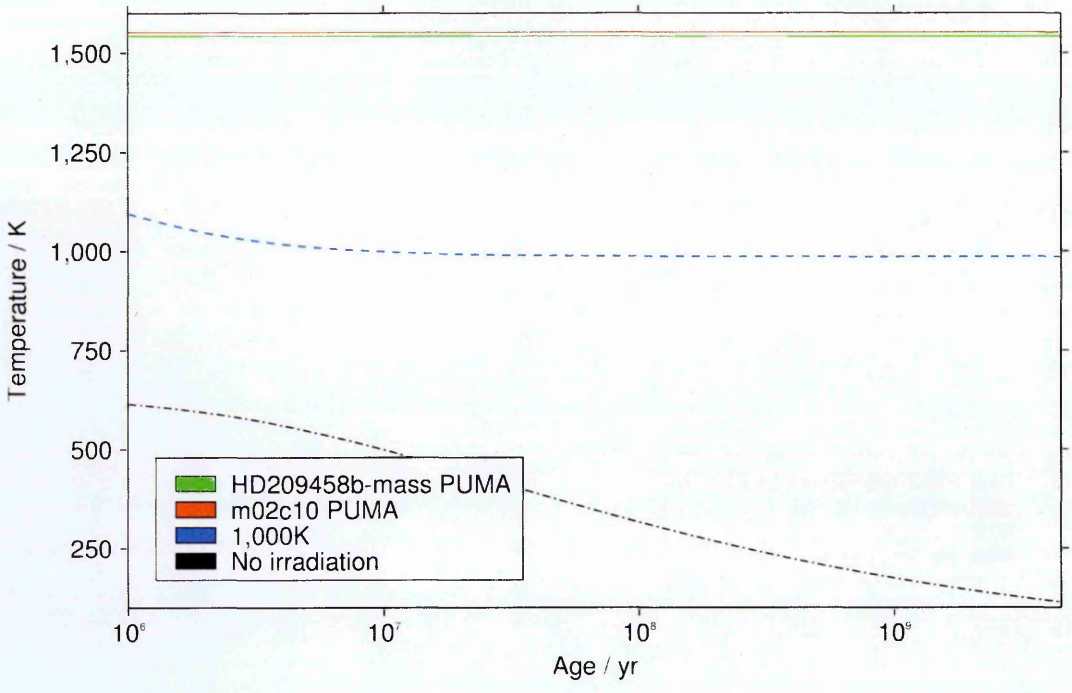

FIGURE 5.23. Comparison of the temperature evolution of the base model m02c10 under different irradiation conditions.

The effective temperatures of the irradiated planets, shown in Figure 5.23, do not evolve with time beyond the initial adjustment stage, as the effective temperature becomes one of the outer boundary conditions. The non-irradiated model cools throughout its lifetime to around 100 Kelvin, but the other models, once adjusted, remain at their specified values. The additional adjustment phase required for the HD 209458b-mass model forbids its history from being displayed prior to 10^6 years. Both this and the high-irradiation *m02c10* model have already reached their required temperature state, while the earlier 1,000K model, which began above rather than below its newly specified effective temperature, continues to adjust visibly in $T_{\rm eff}$ for the first 10^7 yr. This period corresponds to that during which the instability in the radius on the highly-irradiated *m02c10* becomes visible.

Figure 5.24 displays the final temperature-pressure profiles of the two planets on a log-log graph. Although the solid core of the *m02c10* model is not shown (it acts as an inner boundary condition only), this larger-mass planet still reaches greater pressures than its less massive counterpart. There is everywhere a difference of roughly 0.2 between the two profiles, with the *m02c10* model everywhere around 1.6 times hotter than the cooler HD 209458b-mass model. Although their effective temperatures are

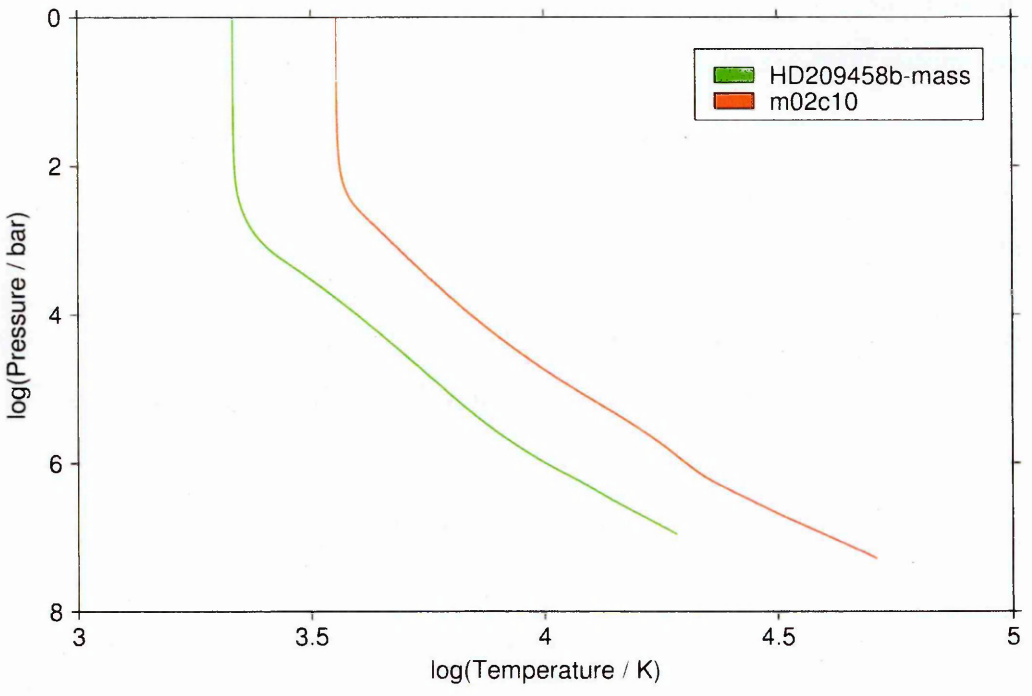

FIGURE 5.24. Final temperature-pressure profiles of the two models with an irradiation corresponding to $T_{\text{eff}} = 1,550K$ at 4.5 Gyr

the same to within a few degrees, the lower-mass planet is much cooler throughout its profile than is the higher-mass one. The transition from an isothermal profile to the deep adiabat occurs lower in the atmosphere (at higher pressure) in the low-mass planet than in the high-mass one, and forms a shallower curve in comparison.

5.3. Specific Exoplanets

This section takes a small number of exoplanets with relatively well-studied properties, and applies MESA and PUMA in sequence to determine their less-constrained properties. The five planets studied are HD 189733b, HD 209458b, WASP-12b, WASP-7b, and WASP-46b. The latter two planets are as yet less well-studied, providing an opportunity to predict more information.

5.3.1. Introducing the Planets. Five planets were initially chosen to form the basis for this study: HD 209458b, HD189733b, WASP-12b, WASP-7b, and WASP-46b. Three of the five (HD 209458b, HD189733b, and WASP-7b) were then followed through both model stages. All five planets and their known properties are discussed below.

HD 209458b is a well-known inflated hot Jupiter. First observed to transit in 1999 by Henry et al. (1999) and Charbonneau et al. (2000), it has a mass of just 0.69 M_J, yet is almost 40% larger than Jupiter, with a radius of 1.38 R_J. Orbiting a G star at a distance of just 0.05 AU, the irradiation received from its parent heats its upper atmosphere to over 1,500 Kelvin. Since the intercomparison studies of Chapter 3 were based around the parameters of this long-known planet, modelling it more specifically here provides a useful point of comparison to previous results, as well as the interest that such a planet naturally arouses.

Discovered more recently, in 2005, HD 189733b is a heavier, less inflated planet, at around 1.14 times both the mass and radius of Jupiter. Although it orbits closer to its star than HD 209458b, at 0.03 AU, the lower temperature of the K dwarf HD 189733 means that the planet is actually less heavily irradiated, and observations have placed its peak brightness temperature at 1,212 $\pm$ 11 Kelvin. (Knutson et al., 2007)

WASP-12b, discovered in 2009 by Hebb et al. (2009), was at the time the hottest transiting planet known. An extreme case, it orbits 0.02 AU from a G star, resulting in an equilibrium temperature of over 2,500 Kelvin. Its atmosphere has overflowed its Roche lobe, and is escaping towards the star, as discussed by Li et al. (2010) and Fossati et al. (2010).

Less is currently known about the planets WASP-7b and WASP-46b, discovered by Hellier et al. (2009) and Anderson et al. (2012) respectively. The former is almost the same mass as Jupiter, and orbits an F star at 0.06 AU, while the latter is twice Jupiter's mass, orbiting a G star at 0.02 AU. WASP-7b was originally thought to be more dense

than Jupiter, but subsequent observations by Southworth et al. (2011) proved this wrong. WASP-46b's thermal emission has been observed during one secondary eclipse by Chen et al. (2014), producing tentative brightness temperatures from the dayside of approximately 2,400 Kelvin, indicating a low heat redistribution efficiency.

The most relevant of the known properties of the five planets are summarised in Table 5.2.

	Planet				
Parameter	HD 209458b	HD 189733b	WASP-12b	WASP-7b	WASP-46b
Mass / M_J	0.69 ± 0.02	1.14 ± 0.03	1.4 ± 0.1	0.96 ± 0.13	2.10 ± 0.07
Radius / R_J	1.38 ± 0.02	1.14 ± 0.08	1.74 ± 0.09	1.33 ± 0.09	1.31 ± 0.05
a / 10^{-2} AU	4.75 ± 0.06	3.14 ± 0.05	2.29 ± 0.08	6.2 ± 0.1	2.45 ± 0.03
Period / day	3.52	2.22	1.09	4.95	1.43
Star Age / Gyr	4 ± 2	> 0.6	1.7 ± 0.8	2.4 ± 0.1	1.4 ± 0.6
Star T_{eff} / K	$6,100 \pm 100$	$4,880 \pm 40$	$6,300 \pm 150$	$6,400 \pm 100$	$5,620 \pm 160$
Star M / $M_\odot$	1.15 ± 0.02	0.8 ± 0.4	$1.35 \pm \pm 0.14$	1.28 ± 0.06	0.96 ± 0.03
Star R / $R_\odot$	1.20 ± 0.06	0.81 ± 0.02	1.60 ± 0.07	1.43 ± 0.09	0.92 ± 0.3

TABLE 5.2. Table of specific exoplanetary parameters. All values taken from the Exoplanet.EU database. (Schneider, 1995-2015) Where errors are not indicated, it is due to their being of greater precision than that of this table. The age of HD 189733 is a minimum value only.

From this information, it is possible to derive further quantities of use for modelling purposes, specifically the flux at each planet from its parent star, and the approximate equilibrium temperature of each planet. These are shown in Table 5.3.

Planet	HD 209458b	HD 189733b	WASP-12b	WASP-7b	WASP-46b
Flux / W m^{-2}	1.077×10^6	4.575×10^5	9.438×10^6	1.095×10^6	1.715×10^6
T_{eq} / K	1,590	1,200	2,560	1,500	1,670

TABLE 5.3. Table of derived quantities for each exoplanet.

5.3.2. Interior Structure. Due to time constraints and difficulties in modelling, only the three planets HD 209458b, HD 189733b, and WASP-7b were modelled, using coreless models of the correct respective masses. Each was created and irradiated to the irradiation values displayed in Table 5.3, and an atmospheric boundary condition applied specifying the equilibrium temperature as appropriate from Table 5.3. These are derived from the parameters in Table 5.2, which contains the relevant known information about each exoplanet.

The radial evolution of the three planets, each to its respective approximate age, is shown in Figure 5.25. HD 209458b contracts at an almost constant rate in log(time),

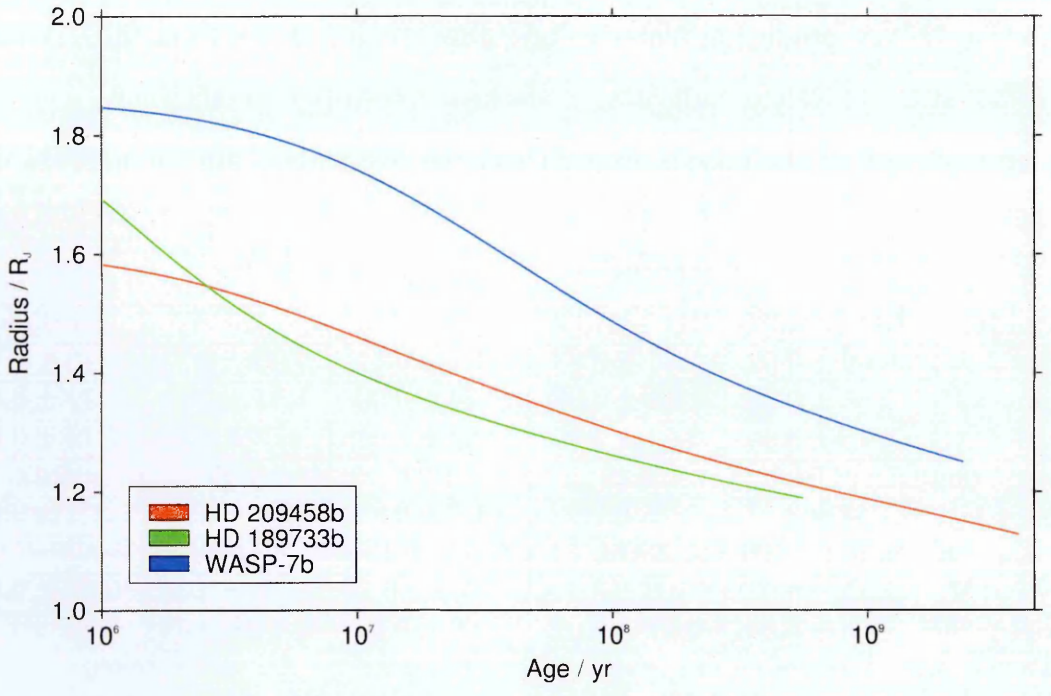

FIGURE 5.25. Radial evolution of HD 209458b, HD 189733b, and WASP-7b, to their respective approximate ages of 4, 0.6, and 2.4 Gyr.

whereas WASP-7b initially contracts slowly, but then more rapidly, beginning to approach the others more closely in radius. HD 189733b, by contrast, which is a distinctly cooler model, initially contracts rapidly and then slows down, so that it crosses the evolutionary path of HD 209458b once, at around 2×10^6 years into evolution. The final radius of the HD 209458b model, $1.13R_J$, differs from that of the actual planet, $1.38R_J$ (see Table 5.2) by over 18%, a not unexpected result since no additional, more speculative forms of radius inflation were tested: HD 209458b is well known to be inflated above all predictions for a planet of its low (0.69 M_J) mass. The WASP-7b model, by contrast, ends its evolution at a radius of $1.25R_J$, which is a difference of only 6% from the true radius of $1.33R_J$. Further modelling would likely be able to produce a closer result; however, this model appears to produce a reasonable approximation to the gross planetary characteristics. Finally, the modelled HD 189733b ends its evolution larger, rather than smaller, than its real counterpart, with radii of $1.19R_J$ and $1.14R_J$ respectively. This difference of only 4.4% encourages the production of closer approximations by further modelling, and is one element in favour of using other data from this model to impact its simulated atmosphere in the following subsection.

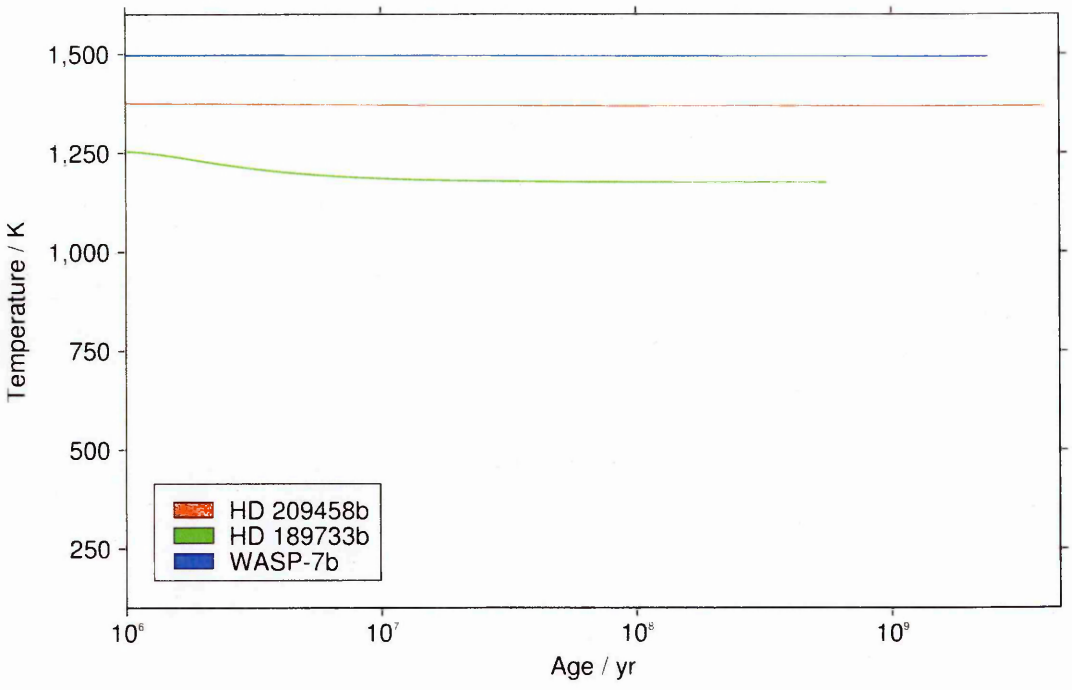

FIGURE 5.26. Effective temperature evolution of HD 209458b, HD 189733b, and WASP-7b, to their respective approximate ages of 4, 0.6, and 2.4 Gyr.

Figure 5.26 shows the effective temperatures of the three planets on the same graph, permitting direct comparison of their evolution. The high levels of irradiation received by WASP-7b and HD 209458b in particular ensure that, by 10^6 years, only HD 189733b is still able to noticeably cool, with its effective temperature levelling off and remaining essentially static after around 2×10^7 years. All three planets maintain effective temperatures well above 1,100 Kelvin. This artificially maintained effective temperature masks any potential signatures of their evolutionary history and/or interior composition that such a measurement might otherwise provide, although the cases of the isolated planets in Section 4.2.1 and the less-irradiated planets studied in Section 4.2.2 also indicate that without significant initial differences, such a measurement would be of limited use.

Figure 5.27 shows the temperature-pressure profiles for each of the three planets at their respective present-day stages of evolution, 4, 0.6, and 2.4 Gyr respectively. Despite its heated atmosphere, the deep profile of HD 209458b is distinctly cooler than the other two planets below about 100 bars, and the isothermal region in its outer layers extends to the greatest depth before curving gradually onto an adiabat. HD 189733b

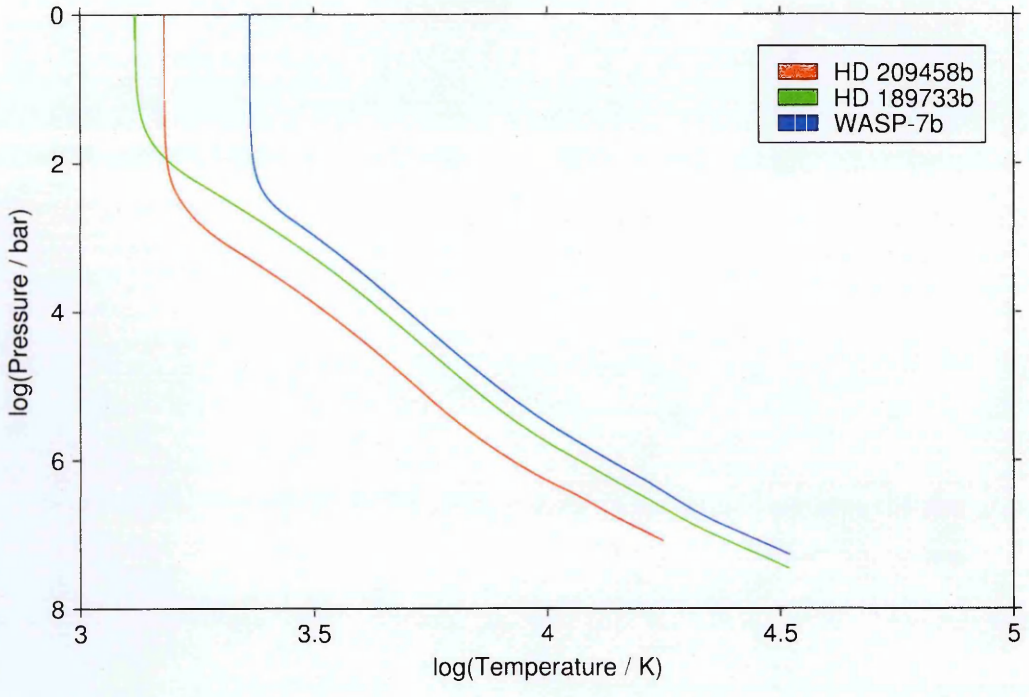

FIGURE 5.27. Temperature-pressure profiles for HD 209458b, HD 189733b, and WASP-7b at the final stage of their evolution.

and WASP-7b, the more massive planets, have very similar deep adiabats, but the greater irradiation of WASP-7b brings it onto an isothermal profile much deeper than HD 189733, with the result that the latter planet is by far the coolest at the outermost layers, despite being relatively warm in the interior. Effects such as this cannot be directly observed, and rely on modelling to suggest, but by the same token are difficult to constrain.

5.3.3. Atmospheres. The three planets studied in the previous section, HD 209458b, HD 189733b, and WASP-7b, are now introduced to PUMA. Where possible, atmospheric and planetary parameters are taken from the corresponding interior model, with the partial exception of HD 209458b, whose true radius and 'surface' gravity are used due to the great discrepancy between the model and the planet. The form of the forcing remains the same as in previous runs, with the simple dayside hotspot and nightside cold spot, but the magnitude is adjusted to suit. Rotational rates are taken from Table 5.2, assuming that the three planets are synchronised such that one rotation takes place over the course of one orbit.

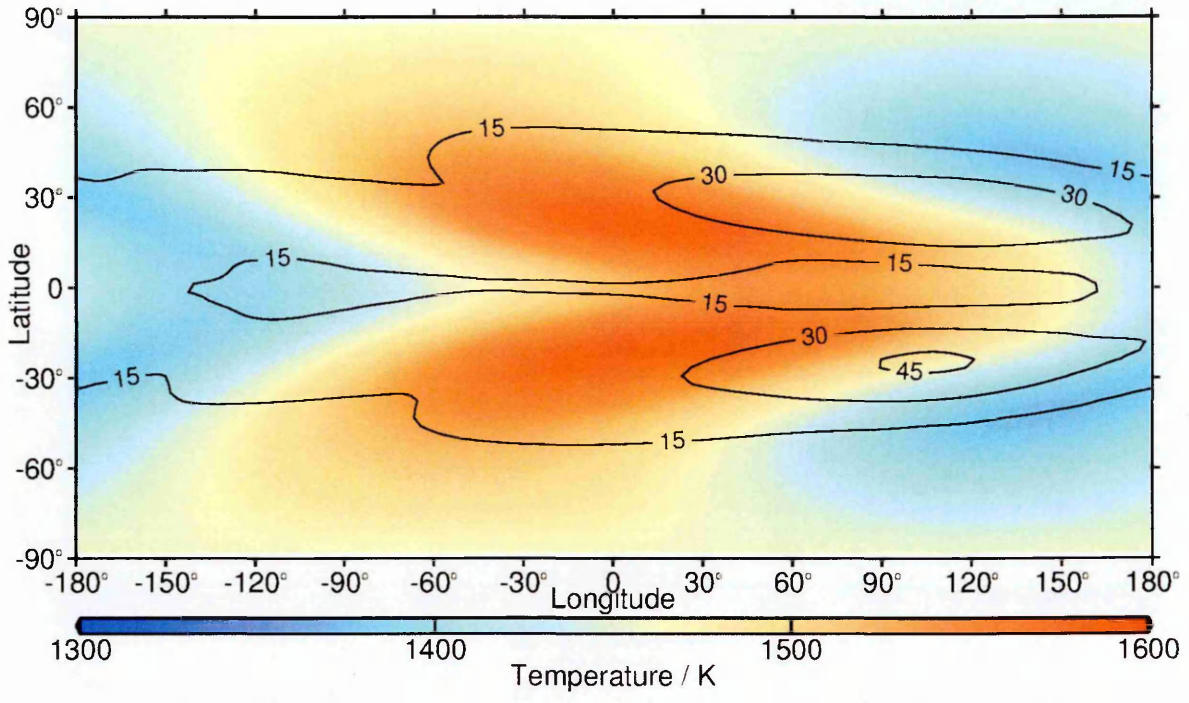

FIGURE 5.28. Temperature mean and standard deviation for HD 209458b at $\sigma = 0.7$

Figure 5.28 shows the time mean and standard deviation of temperature for HD 209458b on the $\sigma = 0.7$ level. It is unsurprisingly similar to the simplified intercomparison planet of Section 3.2.1; however, some differences are revealed: the planet is everywhere cooler, and the variability is decreased. The slight asymmetry in variability is likely due to the shorter length of the run, providing a shorter timespan over which the results can be averaged: these planets were run for a maximum of 300 planetary days after the initial approximately 30-day spin-up period.

The zonal mean temperature and standard deviation for HD 209458b are shown in Figure 5.29. The variability is again lower in all locations than the intercomparison planet, with the temperature standard deviation decreased by typically around 5 Kelvin. However, the zonal wind, shown in Figure 5.30, demonstrates an equatorial jet that is more powerful and reaches higher into the atmosphere, bounded between the same latitudes of roughly $\pm 25°$.

Figure 5.31 displays the mean meridional circulation for HD 209458b. Again, it bears a strong similarity to the intercomparison model, with air descending over the equator and rising at $\pm 60°$, but is roughly $2\times$ weaker. While equatorial regions of the atmosphere are well mixed, the same cannot necessarily be said of the poles.

Observing the temporal variability of this model indicates that it switches between phases of high activity, in which vortices form and travel westward on either side of the

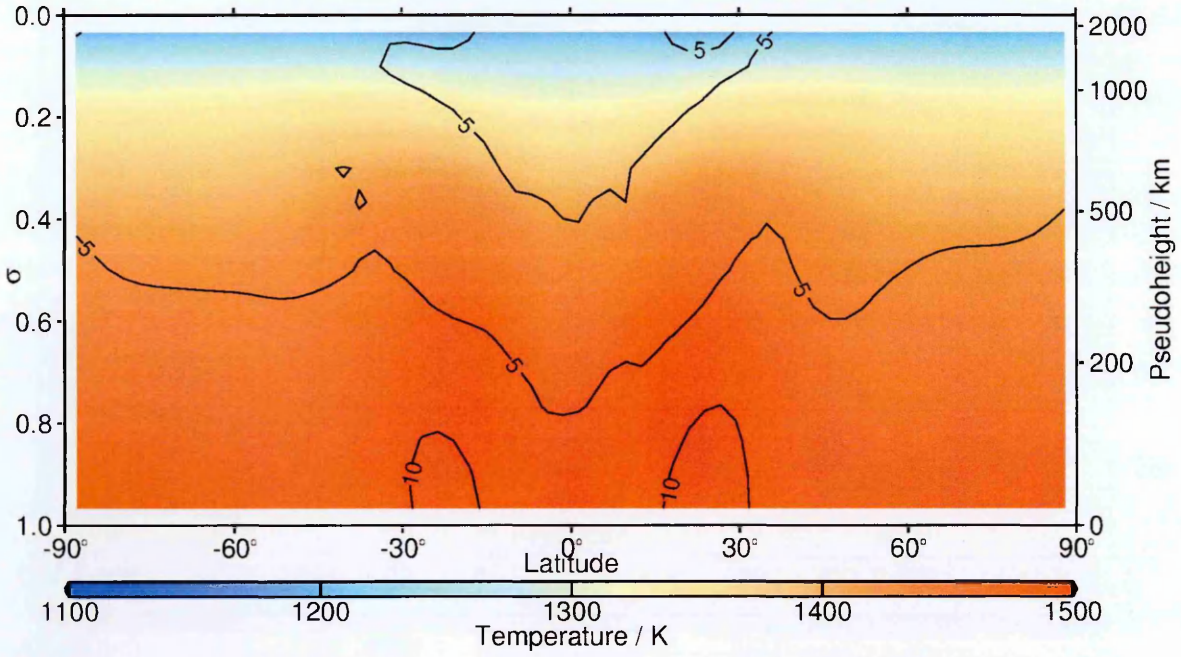

FIGURE 5.29. Zonal mean temperature time mean and standard deviation for HD 209458b

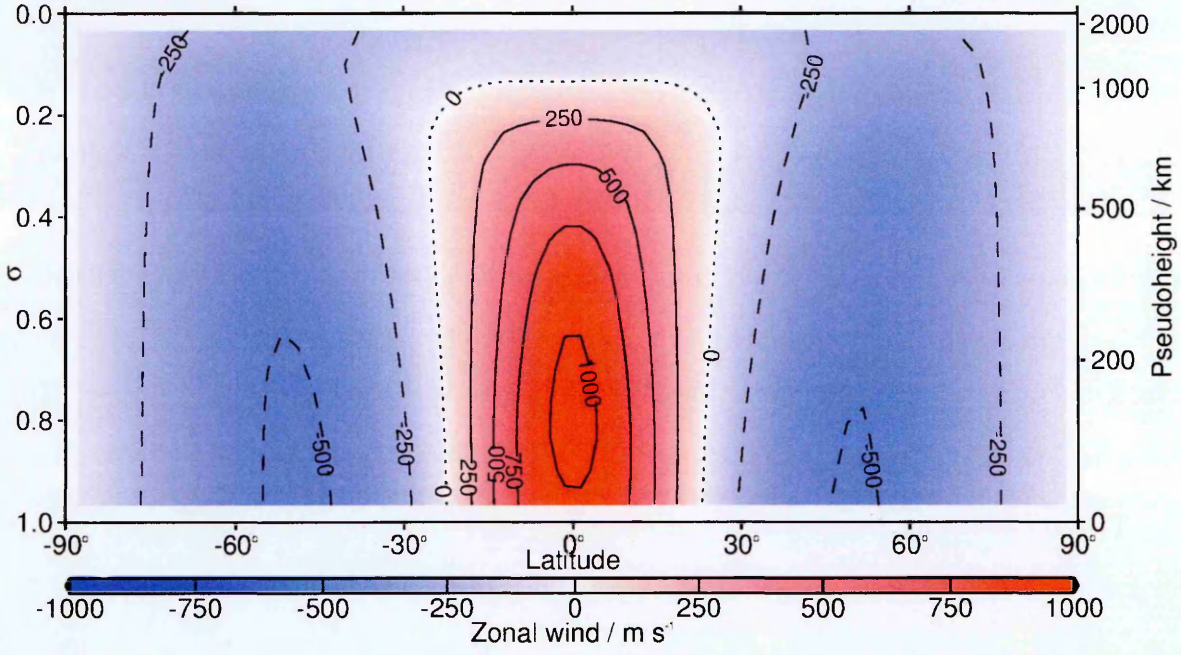

FIGURE 5.30. Zonal mean wind time mean for HD 209458b

equator before dispersing and returning to a calm, relatively equatorially symmetric flow state 7-8 orbits later. The entire cycle repeats with a periodicity of roughly 19 orbits, meaning the planet spends approximately 2/3 of its time in a calm state. At higher pressures, $\sigma = 0.7$ or $p \approx 700$ mbar, the motion in the active state merely causes the chevron pattern to fluctuate north-south in a weaving motion; however, at higher altitudes of $\sigma = 0.37$, 300 km in pseudoheight above the $\sigma = 0.7$ layer and a pressure of approximately 370 mbar, a series of miniature hotspots are formed that can travel into the nightside before dispersing.

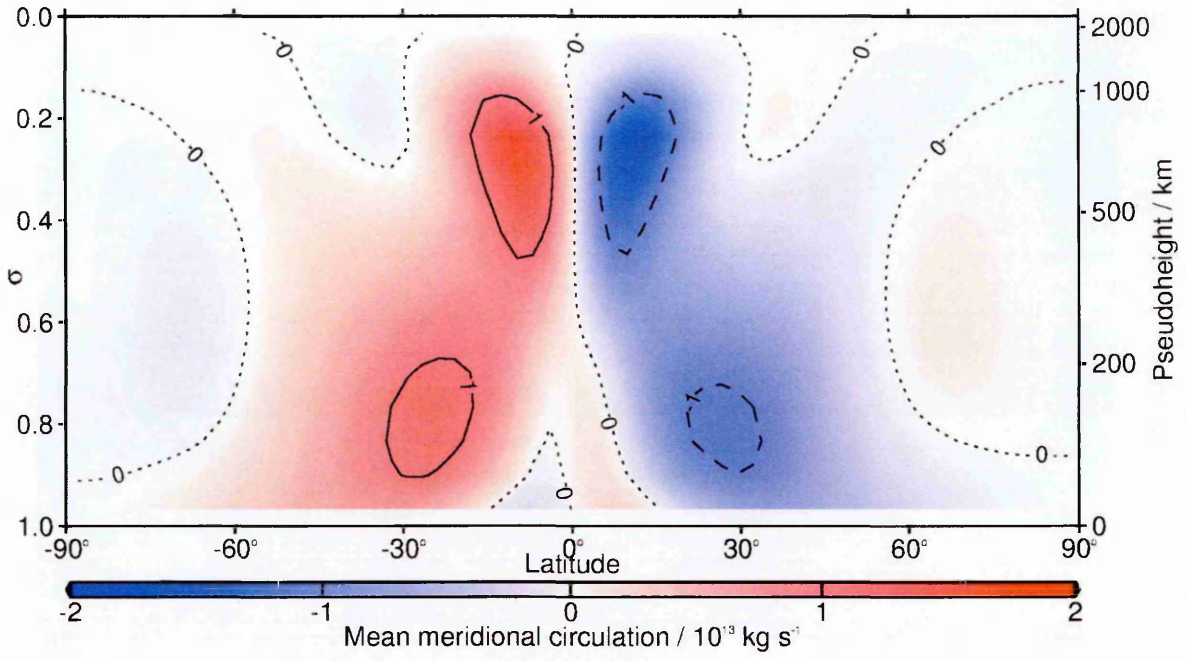

FIGURE 5.31. Time-averaged HD 209458b mean meridional circulation

HD 189733 displays a very similar, though cooler, average temperature pattern at $\sigma = 0.7$, as shown in Figure 5.32. The variability is distinctly higher than that of HD 209458b, with the standard deviation exceeding 60 Kelvin in the two regions bounded by $\pm(15° - 30°)$ latitude, and roughly $60° - 160°$ longitude. The increased variability is not only due to the greater temperature gradient between minimum and maximum: as discussed below, when the time evolution of the atmosphere is observed, it demonstrates a more variable pattern than that of HD 209458b, never reaching as symmetric a state.

Figure 5.33 shows the time mean and standard deviation of the zonal mean temperature for HD 189733b. Although the variability in temperature is high on the horizontal plots, when averaged longitudinally, the variability becomes much lower, nowhere reaching 15 Kelvin. Note the difference in pseudoheight: the different properties of HD 189733b's model atmosphere render it distinctly vertically thinner than that of HD 209458b.

The temporally averaged zonal mean zonal wind for HD 189733b is shown in Figure 5.34. A very powerful, vertically broad superrotating jet can clearly be seen, with averaged windspeeds of up to 1,300 ms^{-1} at its centre, extending to above $\sigma = 0.5$ and continuing deeper into the atmosphere than the model base. A much weaker return flow dominates beyond $\pm 25°$ latitude, and at the very top of the atmosphere.

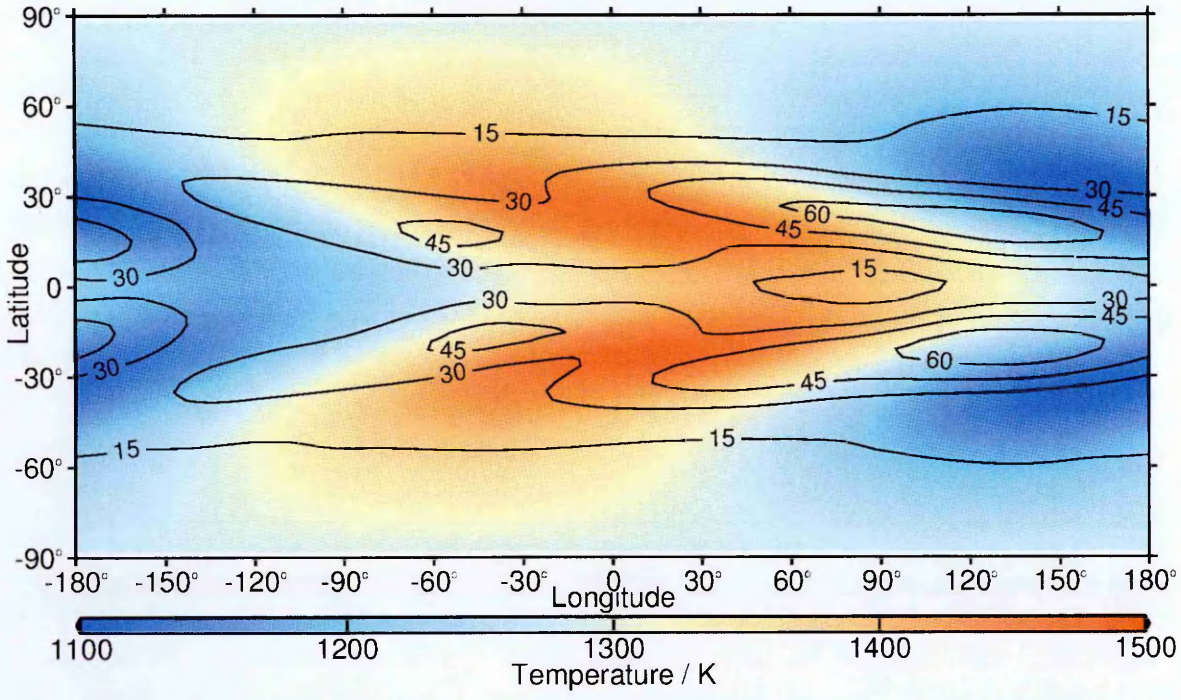

FIGURE 5.32. Temperature mean and standard deviation for HD 189733b at $\sigma = 0.7$

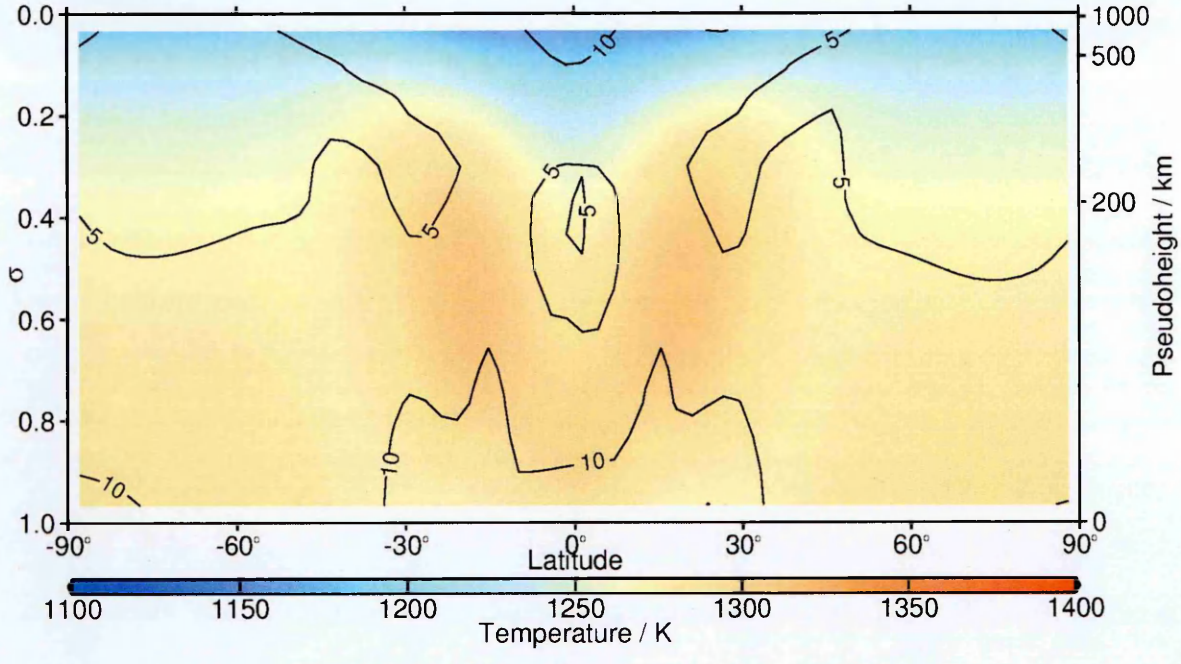

FIGURE 5.33. Zonal mean temperature time mean and standard deviation for HD 189733b

Figure 5.35 displays the time-averaged mean meridional circulation in the HD 189733b atmosphere. Once again, air primarily descends over the equator, but now primarily rises between $\pm(60° - 30°)$ latitude, the cell narrowing with increasing height. Just above the 1 bar level, two small cells rotate in the opposite sense, so that in the lowest parts of the atmosphere, air now rises over the equator. At their widest point, these cells extend no further than 20° in latitude. The slight clockwise (counterclockwise) circulation over the north (south) pole is also somewhat expanded. Overall,

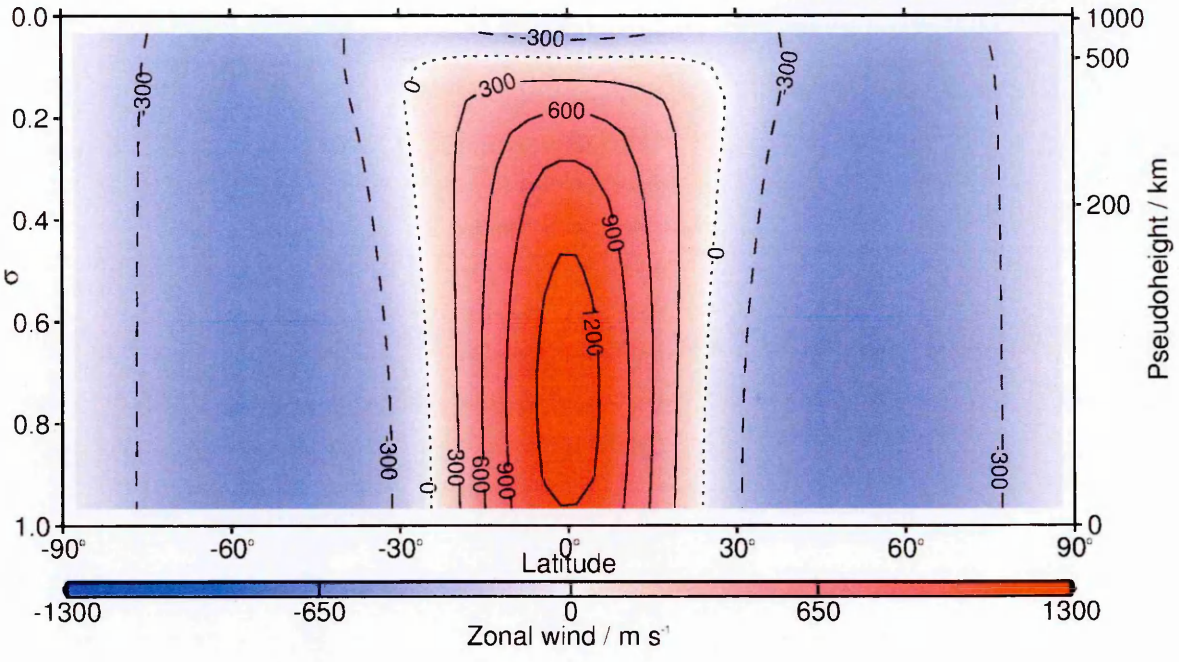

FIGURE 5.34. Zonal mean wind time mean for HD 189733b

however, the circulation is weak compared to that of HD 209458b: note the order of magnitude difference in scale. The increased rotation rate of this planet (2.22 days vs. 3.52) accounts for part of this difference, as observed in the rotation rate tests of Section 3.2.2.

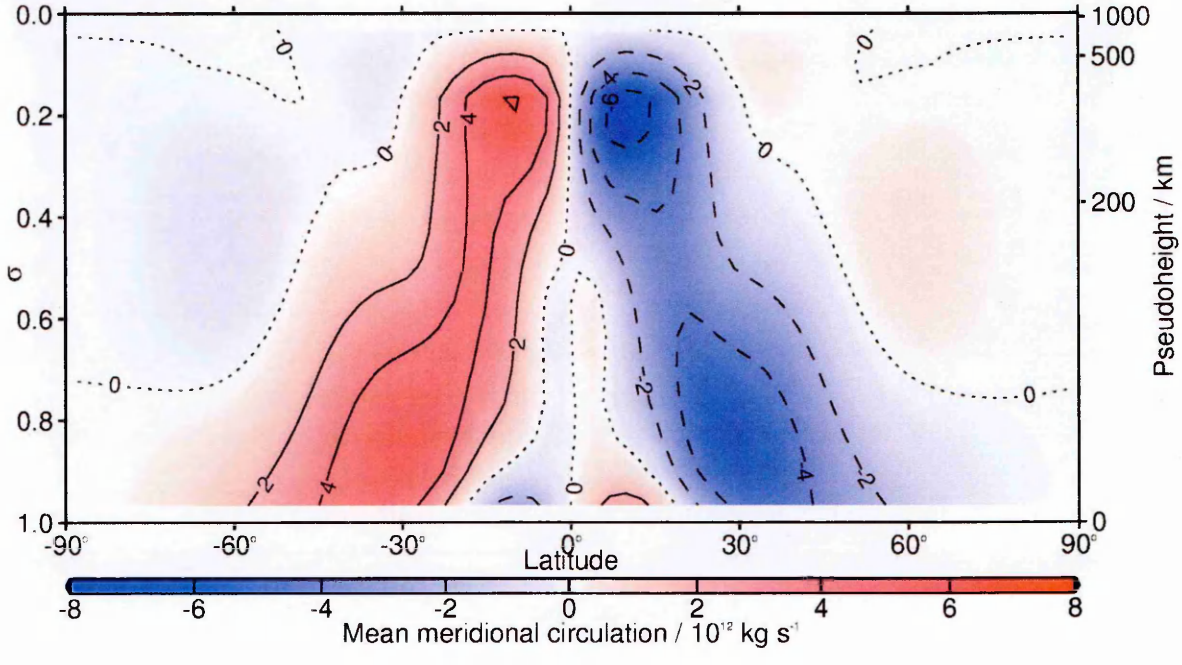

FIGURE 5.35. Time-averaged HD 189733b mean meridional circulation

As implied by the temperature plots, HD 189733b displays more variability than HD 209458b when its temporal evolution is studied. Unlike the latter planet, it never enters a very equatorially-symmetric 'calm' state, with the equatorial jet always displaying two to three kinks in its flow, and on all levels, the jet never becomes as disrupted as

that of HD 209458b. The smaller vortices formed here tend to drift slightly eastward rather than westward. At higher altitudes, it is again possible for warmer spots to migrate to the nightside; a typical such spot lasts for on the order of one orbital period before dissipating.

In subsequent plots, the apparent reduced symmetry of WASP-7b in comparison to the other two planets is expected to result from time constraints that restricted the length of the WASP-7b run to half the runtime of HD 209458b and HD 189733b.

Figure 5.36 shows the temperature mean and standard deviation for WASP-7b at $\sigma = 0.7$. This hotter, slower-rotating (4.95 day) planet exhibits a very different average temperature pattern and pattern of variability, with the distinctive chevron shape of earlier runs here replaced by a pair of hotspots centred on $\pm 30°$ latitude and approximately 30° longitude. This symmetrical pattern does not appear on the face of the planet itself, as the twin hotspots result from alternating temperature peaks in these two locations. It bears a distinct similarity to the 6-day rotation rate planet of Section 3.2.2.

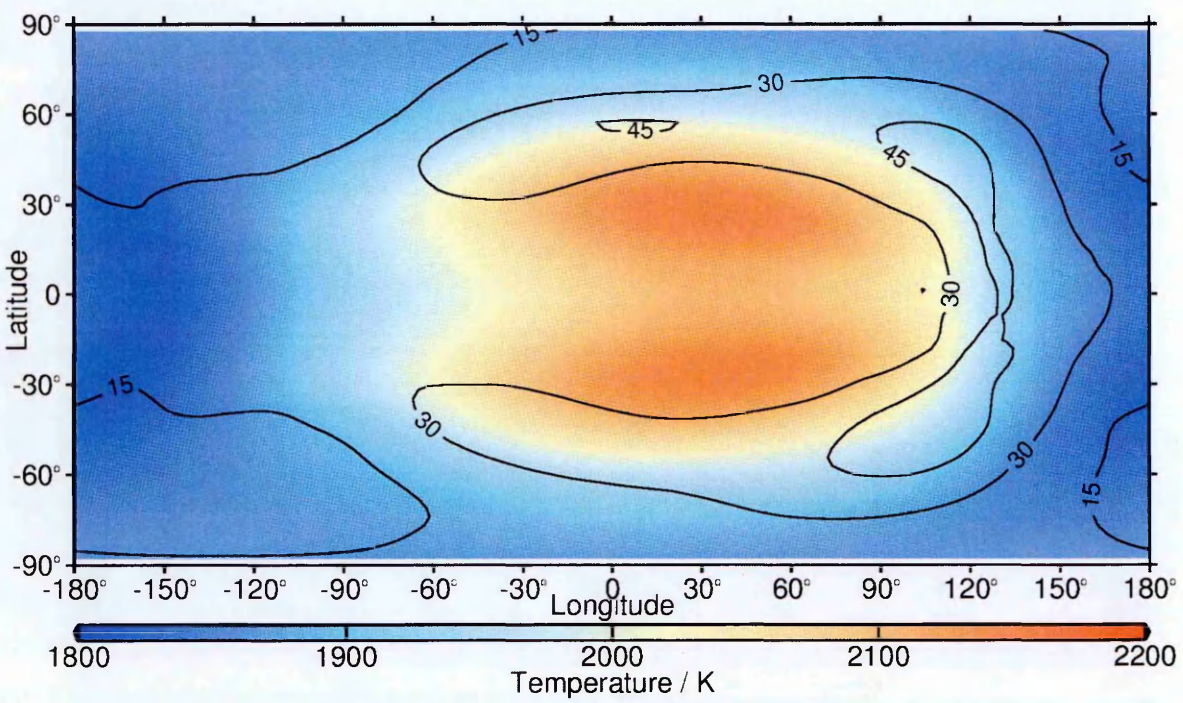

FIGURE 5.36. Temperature mean and standard deviation for WASP-7b at $\sigma = 0.7$

Figure 5.37 shows the temporally averaged zonal mean temperature and corresponding standard deviation for WASP-7b. At low levels, below about $\sigma = 0.8$, the variability grows higher than 15 Kelvin between $\pm(40° - 60°)$. The zonal mean temperature becomes latitudinally almost uniform high in the atmosphere.

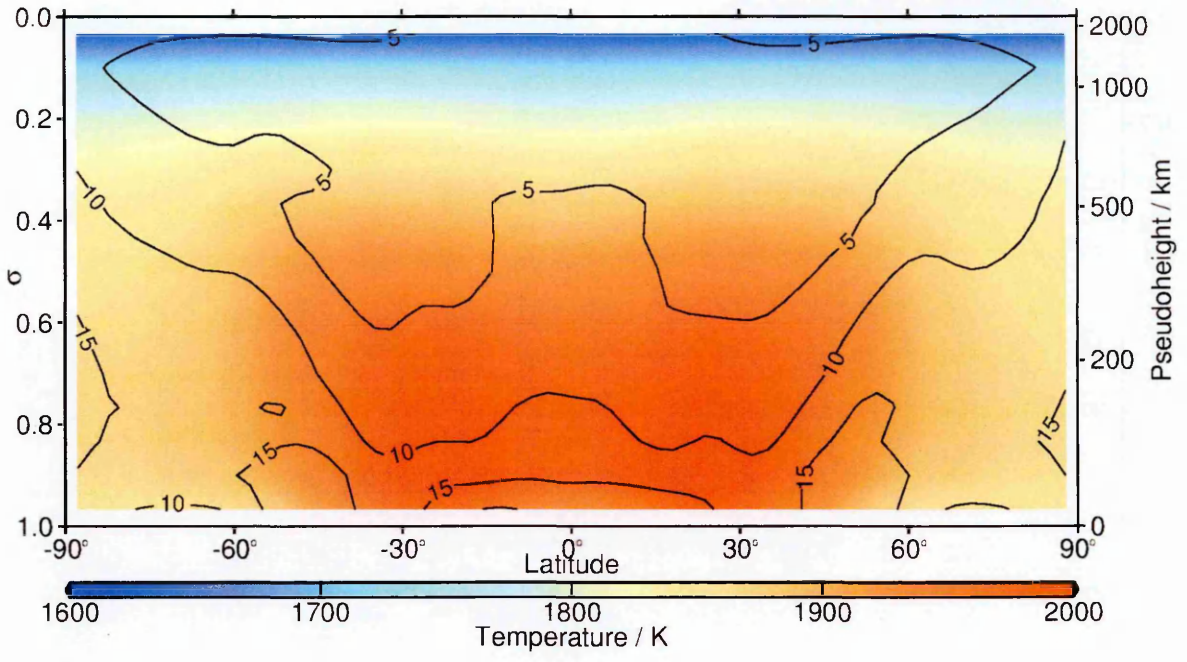

FIGURE 5.37. Zonal mean temperature and standard deviation for WASP-7b

The temporally averaged zonal mean winds of WASP-7b are shown in Figure 5.38. While still clearly present, the equatorial jet is much weaker, reaching only 500 m s^{-1} at its maximum. It is unique among the planets here studied in that the low-level reverse flow near the model base actually exceeds the equatorial jet in speed, with a westward velocity of up to over 600 m s^{-1}, though these winds are likely to be too deep in the atmosphere to detect observationally.

The temporally averaged mean meridional circulation, displayed in Figure 5.39, shows clockwise circulation throughout the entire southern hemisphere, with anticlockwise circulation similarly throughout the northen hemisphere. These two cells appear to contain a pair of regions of stronger overturning, with the stronger regions centred between $\pm(50° - 60°)$, and the weaker regions centred on approximately $\pm 15°$.

When observed over the course of the model run, it is possible to draw conclusions about the variability of WASP-7b despite the somewhat shorter run length. The weaker winds are less likely to provide opportunities for detection, but the main sources of variability in temperature occur in the 'switching' that takes place between the two hot regions identified in Figure 5.36, which extend into the higher regions of the atmosphere. Latitudinally averaged, therefore, the temperature variation is minimised, and it is likely that a brightness temperature map of this planet would reveal a reasonably close correspondence to the average state.

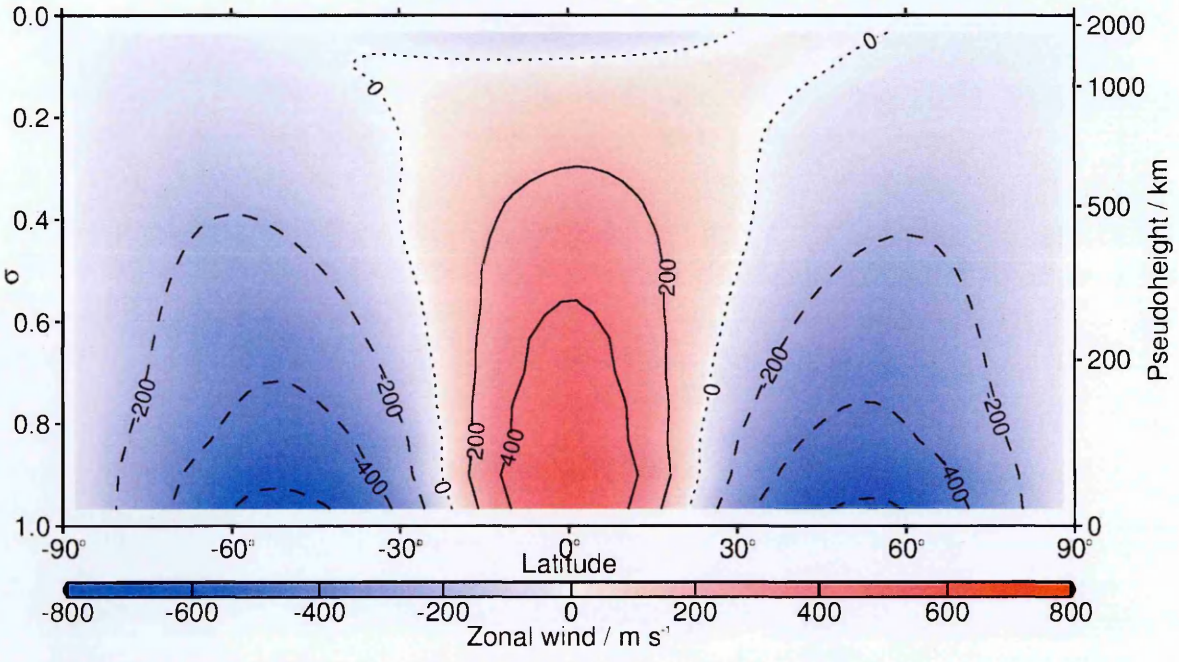

FIGURE 5.38. Zonal mean winds for WASP-7b.

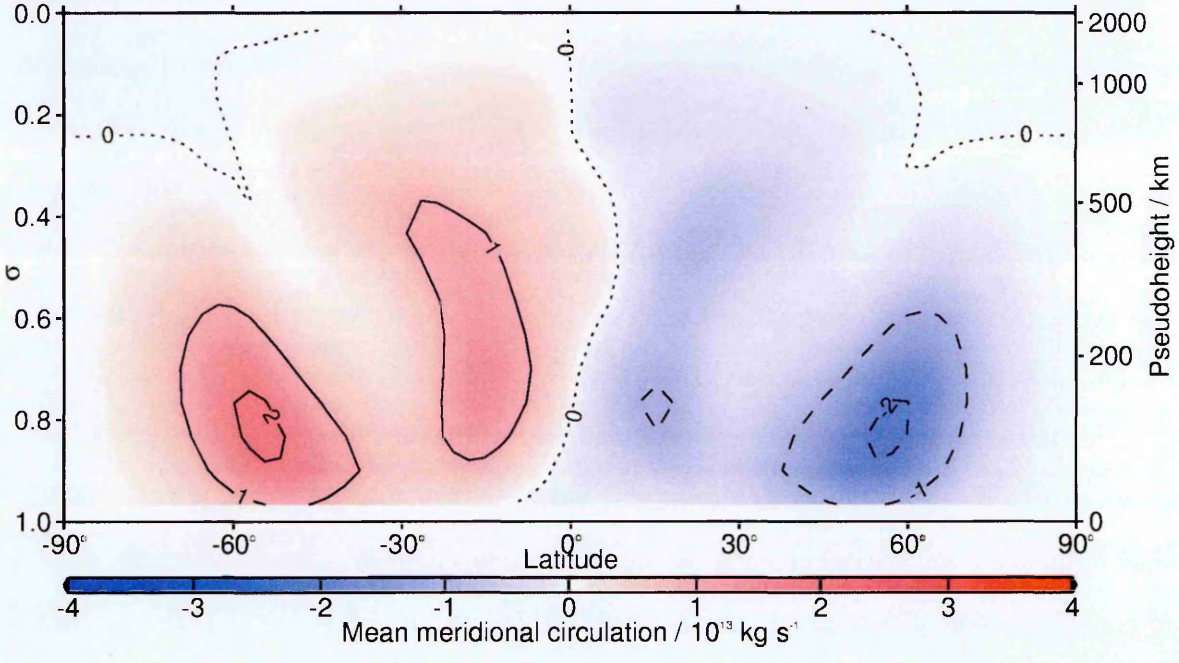

FIGURE 5.39. Mean meridional circulation for WASP-7b

5.4. Discussion

The MESA suite of planets irradiated to 1,000 Kelvin produces distinct changes in the time mean results when introduced to PUMA via boundary conditions and planetary properties: a given evolution track can plausibly affect the atmospheric model results gained as a result, although the changes are in general relatively small. It proved difficult, however, to find useful constraints that could be produced from the atmospheric model for use in the construction of an interior.

Although high-irradiation modelling is a more sensitive task than low or no irradiation, it proved possible to model both WASP-7b and HD 189733b to within 6% of the known constraints without difficulty. Time constraints precluded the modelling of WASP-46b, and WASP-12b's extreme conditions resulted in model breakdowns that could not be resolved within the time allotted. Although inflated planets such as HD 209458b are not reproduced with the correct size, it is then possible to introduce information from these models, from surface temperature and gravity to the compositional properties of the gas at the surface, into the atmospheric model.

HD 209458b's model atmosphere appears to spend roughly 2/3 of its time in a calm, relatively equatorially symmetric flow state. This state periodically disrupts, introducing large instabilities and altering the temperature distribution, with travelling localised hot and cold spots moving between dayside and nightside. This state can persist for several orbital periods, with the whole cycle having a periodicity of roughly 20 orbits. Although the flow on HD 189733b is never equatorially symmetric as it can appear on HD 209458b, it does not exhibit the same levels of disruption, and forms travelling hot and cold spots more frequently. WASP-7b has a very stable flow state, displaying little variability in longitude: the majority of its temporal variation occurs between north and south. The latitudinally-averaged hotspot is predicted to be slightly extended and somewhat offset, with the warmest location at approximately 30° east of the substellar point. The winds are relatively low in the upper atmosphere, and the equatorial jet, while still present, is of lower strength than on other planets.

CHAPTER 6

Conclusions

The study of the evolutionary history and atmospheric conditions of hot Jupiter exoplanets, begun separately in Chapters 3 and 4, was brought together in Chapter 5. The conclusions of each strand of work are now united here in answering the questions posed at the very beginning of this work:

(1) How does the interior structure of a hot Jupiter evolve?

(2) How does the atmosphere of a hot Jupiter behave?

(3) To what extent do these factors affect one another?

(4) What conclusions can be drawn for future observations?

High irradiation keeps a hot Jupiter's effective temperature high long after it would have otherwise cooled, delaying its contraction, but the inflated planets remain unreproduced. Despite the large-scale characteristics of atmospheric flow on hot Jupiters, whose length scales are comparable to their radii, it is found to be possible to distinguish the behaviour of one from that of another, although most such differences are typically governed by relatively simple alterations, such as the difference in rotation rate. The particular conclusions drawn for individual planets suggest potentially detectable levels of variability in some cases, which would plausibly affect the specific results gained from detailed measurement.

6.1. The Evolution of Hot Jupiter Exoplanets

Gas giant planets, which do not undergo nuclear fusion in their cores, are formed in a protoplanetary disk and contract and cool with time, converting gravitational potential energy into heat which is radiated away. If a planet's cooling is restricted, it will not contract as rapidly if at all, since the energy cannot be lost as readily. Each planet will have a different metallicity depending on the conditions from which it was formed. Some gas giants may have rocky cores, which typically do not directly affect the composition of the planet during its further evolution but still affect its evolution as they are much more dense than the rest of the material and add additional gravitational pull. Each planet has its own individual values of these and more factors, but in general if sample points can be taken in parameter space they can be interpolated between.

The initial parameter space scans in Section 4.2.1 demonstrate the general trends clearly. Planets of higher core mass are everywhere smaller than their equal-mass counterparts with lower mass or no core. Higher metallicity planets are slightly larger than their lower metallicity counterparts, as the increased metallicity alters the opacities and impedes cooling.

With a baseline established, it becomes possible to discuss the evolution of irradiated planets. These planets are kept at increased surface temperatures due to their proximity to their parent stars. This renders it more difficult for the planet to lose heat, with more constantly being injected, delaying the cooling process and resulting in an increased radius for a given age. However, no focused investigation was conducted into the size of planets known to be inflated, such as HD 209458b, and this remains an interesting topic of further study. When individual planets are modelled despite the poor constraints, it requires minimal adjustment to approach the observed characteristics of non-inflated planets at their respective ages. It would be difficult to pick out potential evolutionary histories for a given planet with current observations, as age and irradiation tend to conceal indicators of past conditions.

6.2. The Atmospheres of Hot Jupiter Exoplanets

The primary driver for the atmospheric dynamics of a hot Jupiter planet is the degree of irradiation received from the parent star. Due to the close orbit, it is expected that the planet's will have become tidally locked with its star. One side of the planet

is thus extremely hot, permanently irradiated, while the other, facing into deep space, is cooler. Atmospheric motions affect this simple pattern, redistributing heat from the hot side to the cold, potentially allowing it to be lost more effectively and altering the heat transport between the upper and lower layers.

Atmospheric motion in response to the intense heating sets up a powerful superrotating wind system at the equator, which carries the heated air rapidly to the colder side of the planet, where heat may escape more readily. In contrast to the behaviour of Jupiter itself, with its many bands and zones, these planets are found to typically exhibit only this single jet in the direction of rotation, with weaker return flow to either side of it. This is readily expected due to the very different scales at work upon these planets, and is a common feature of hot Jupiter modelling work.

The powerful winds predicted on hot Jupiters carry the heated air rapidly away from the point of most intense irradiation, the substellar point, with the result that an offset "hotspot" is typically predicted. This warmest location may be offset by over 90° in the direction of rotation (following the superrotating jet: if the equatorial wind had the same strength but opposite direction, the reverse would be seen). The speed, width, and depth of the jet all combine to affect the location and appearance of the hotspot.

A powerful superrotating equatorial wind is a common feature of all hot Jupiter simulations here carried out. Although if a 'parcel' of air were simply moved from elsewhere on the planet to the equator, conservation of angular momentum would cause it to move more slowly than solid-body rotation, energy input is transferred to angular momentum through eddy processes in the atmosphere, permitting faster winds than would otherwise be the case. (See discussion in Chapter 3.) This strong wind is counterbalanced by a weaker reverse flow pervading all or almost all the rest of the atmosphere. Temporal and zonal mean windspeeds display equatorial symmetry; however, on the day-to-day basis the jet is both thinner and more powerful than this average indicates, fluctuating in strength and north-south direction, as exemplified in the snapshot plots, such as that in Figure 6.1 or the time series of Figure 6.2.

This variability, occurring as it does over the course of multiple planetary days and thus orbits, persists for long enough that a single planetary observation of the secondary eclipse may report upon it in any state, although observations closer to the

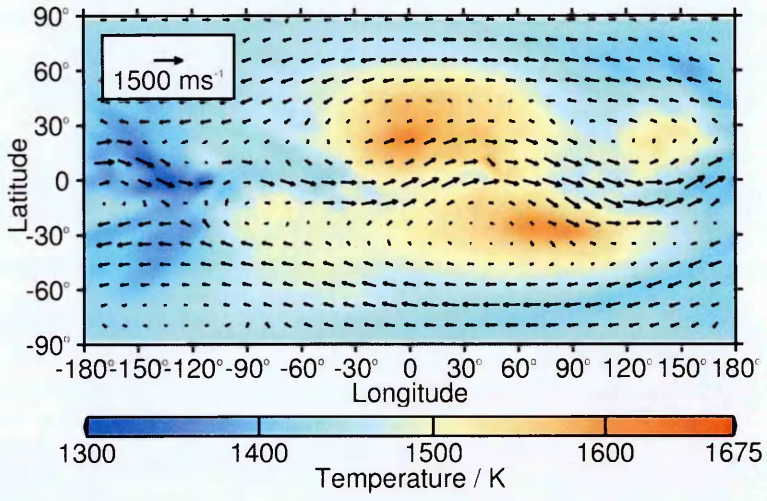

FIGURE 6.1. Example wind and temperature snapshot plot from the intercomparison study.

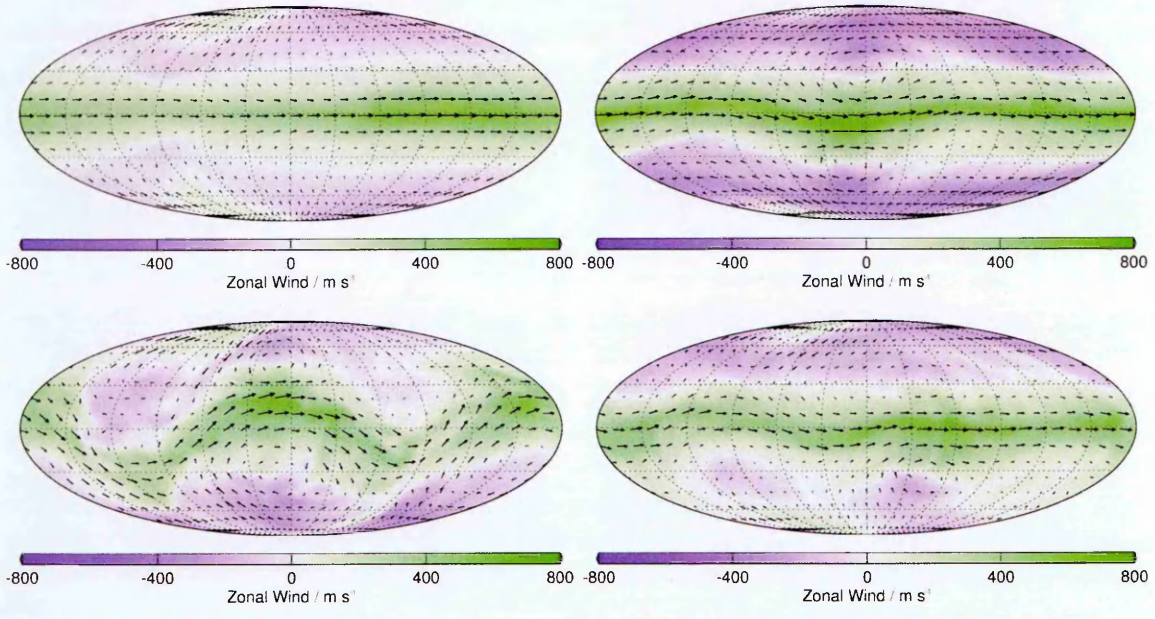

FIGURE 6.2. Example time series of wind snapshots (Figure 5.19). Note that the images are not equally spaced in time, and are taken at 6, 7, and 10 planetary days after the first image, respectively.

smooth-flow state are favoured due to the longer duration of this phase as compared to the maximally disrupted one. It cannot, therefore, be safely stated that any individual observation necessarily accurately represents the typical flow state of the exoplanetary atmosphere.

6.3. Evolution and Atmospheric Dynamics: Complementary Factors?

The more detailed conditions provided by an evolutionary model result in small but notable differences between atmospheric models for what is broadly the same planet. The base surface temperature differing by a few tens of degrees, on exposure to a 200-Kelvin temperature contrast, together with small differences in gravity and radius, can

result in a distinctly warmer or cooler model, though one with much the same thermal and wind structure. The studies in Section 5.1 investigate the modelling of a set of planets with identical masses and irradiation conditions, but different evolutionary histories owing to their differing metallicities and core masses. Although far more variables are available for variation, this focus allows response to the conditions to be more clearly elucidated.

Similarly, the studies in Section 5.2 attempt to apply interior modelling to the constraints determined by the atmospheric models of Chapter 3. However, it proved difficult for a simple GCM to have a direct and clear output that could inform the boundary conditions of the one-dimensional interior model. The flow of information is, at this stage, still easier in the opposite direction, with interior model results informing three-dimensional atmospheric conditions. The potential for further work in this area remains, but would require a tightly focused avenue of investigation.

6.4. Observational Implications

Atmospheric models predict patterns the broadest of which are already within reach of today's observations. High-altitude winds and an approximate brightness temperature map of the planet may be achieved with careful study, dependent on the overall system properties. A more variable star will always render it more difficult to separate the subtle variations due to the properties of the orbiting planet from those of the star. As the next generation of telescopes come into service, it becomes more plausible to discern "detailed" (e.g. low-resolution temperature mapping) observations of a greater number of exoplanets, potentially at higher resolution.

With this increased ability, however, comes an increased chance of detecting a non-typical state. The artificial planets studied in Section 5.1 demonstrate a degree of variability on the timescale of 15-20 orbits, with the most atypical state short-lived, but still of sufficient duration to be observed over the course of an orbit. Repeat observations will thus continue to be warranted, not only to improve accuracy, but also to screen for such atypical states. This may also affect planetary spectra in that vortices can migrate warm and cold regions potentially some distance beyond the terminator, possibly affecting the localised abundance of elements that condense out at high-atmosphere nightside temperatures. The strong winds of these planets will also

contribute to the mixing, however, providing the nightside with a constant supply of air from the dayside.

For each of the three specific planets studied most closely, the observational predictions are as follows:

6.4.1. HD 209458b. HD 209458b's atmosphere is predicted to spend roughly 2/3 of its time in a calm, relatively equatorially symmetric flow state. This state periodically disrupts, introducing large instabilities and altering the temperature distribution, with travelling localised hot and cold spots moving between dayside and nightside. This state lasts for several orbital periods, with the result that observations made over the course of only a small number of orbits cannot guarantee which state may have been captured.

6.4.2. HD 189733b. Although the flow on HD 189733b is never equatorially symmetric as it can appear on HD 209458b, it does not exhibit the same levels of disruption, and forms travelling hot and cold spots more frequently; it is more likely that a given observation will capture something approximating to the average state.

6.4.3. WASP-7b. This planet has a very stable flow state, and is likely to show little variability in brightness temperature, as most of the variation occurs between north and south. The latitudinally-averaged hotspot is predicted to be slightly extended and somewhat offset, with the warmest location at approximately 30° east of the substellar point. The winds are relatively low in the upper atmosphere, and the equatorial jet, while present, of lower strength than on other planets. The main source of variability is at the transition between this hotspot and the cool nightside, at around 120° east.

6.4.4. Planetary Differences. The primary difference between WASP-7b and the other two planets is its longer orbital period and thus rotation rate: though it is irradiated to a similar degree as HD 209458b, has a similar radius, and has a "surface" gravity intermediate between the other two planets, it completes one rotation in 4.95 Earth days rather than HD 209458b's 3.52 or the faster HD 189733b's 2.22 days. (The properties of the planets are summarised in Tables 5.2 and 5.3.) This difference causes the much slower winds and decreased, larger-scale variability compared to HD 209458b, similar to the slow rotator of Section 3.2.2. HD 189733b, on the other hand,

a denser planet with a faster rotation (although with lower irradiation temperatures due to its cooler star), has stronger winds, a vertically thinner atmosphere, and a somewhat smaller characteristic scale, resulting in its smaller, more numerous vortices. In general, rotation rate and planetary radius are important constraints on the types of atmospheric circulation observed, together with the strength and nature of heat sources, which factor is relatively similar between these highly irradiated, tidally locked planets.

6.5. Further Work

The most immediate continuation of this work would be to complete the modelling of WASP-12b and WASP-46b, thereby finishing the suite of planets studied. A further natural extension would be to expand the range of the study, covering more exoplanets, in particular those likely to be amenable to observation by upcoming missions and facilities. In principle, to simulate more planets would primarily require additional computing time, and there are sufficient known hot Jupiters that there will be no shortage of potential study targets for modelling. The primary consideration then becomes the observability of the planet by present or future telescopes: planets which are poor observational candidates may be ruled out as immediately useful for the application of modelling.

Upcoming missions and new ground-based facilities will greatly improve the precision of measurements available to the community, as well as the expected discovery of large numbers of hitherto unknown planets. On Earth, the European Extremely Large Telescope (E-ELT) is now under construction, and, using advanced adaptive optics, will be able to directly observe exoplanets, make extremely high-precision (cm/s) radial velocity observations, and produce transmission spectra of exoplanet atmospheres. In space, GAIA (Perryman et al., 2001) was successfully launched in 2013, has been performing observations since 2014, and is scheduled to release its first dataset in September 2016. Since it is a sky surveying mission, designed to provide positions, parallaxes, and proper motions of millions of stars, it is expected to detect exoplanets in the course of its observations through both astrometry and transit detection. PLATO (PLAnetary Transits and Oscillations of stars) (Rauer et al., 2014) is scheduled for launch in 2024, and will consist of multiple (32 + 2) small telescopes around the L2 point, primarily targeting stars between 4th and 11th magnitude. As the name implies, Plato is a transit mission, and will observe a large number of bright stars for an

extended period of time, with the aim of detecting planets down to the mass of Earth orbiting at distances up to roughly that of Earth. In the course of this search, it will also detect and observe a large number of hot Jupiters with high accuracy, producing precision light curves that may be used to constrain planetary features such as the location and strength of a hotspot as well as determining the gross physical properties of the planet. Promising candidates for further observation may then be followed up by other missions such as the James Webb Space Telescope (JWST, due for launch in 2018) (Gardner et al., 2006). While this mission has many science goals besides the study of exoplanets, it will be able to perform transit spectroscopy to reveal the compositions of the atmospheres of transiting exoplanets. It is additionally equipped with a coronagraph, which will allow for the detection and study of relatively nearby giant planets: it is predicted to be able to detect Jupiter-analogue planets up to 30 parsecs from the Earth.

Launching before PLATO, in 2017, TESS (Transiting Exoplanet Survey Satellite) (Ricker et al., 2014) is designed to search nearby bright stars for transiting sub-Neptune planets, in a complementary search to the fainter stars studied by the Kepler mission. It will conduct an all-sky survey, detecting primarily short-period planets, and in the course of the survey will therefore discover a suite of hot Jupiters. Orbiting bright stars, these planets will be more amenable to follow-up observations with other instruments, and will produce a new population of relatively well-constrained gas giants for study. CHEOPS (CHaracterising ExoPlanet Satellite) (Broeg et al., 2013), also due to launch in 2017, is specifically designed to follow up on initial observations, and will be able to target known planet-hosting bright stars anywhere on the sky. It will be able to provide phase curves for hot Jupiters orbiting these stars in addition to constraining their gross physical parameters.

The measurements produced by these and other missions can confirm or deny model predictions, constraining future modelling efforts and highlighting successes or inadequacies in the models employed. Observations such as the temperature maps of HD 189733b produced by Knutson et al. (2007); Majeau et al. (2012) allow the location and approximate strength of global-scale features to be determined: it is now clear that a model which does not produce a hotspot with peak temperatures appearing approximately 30° east of the substellar point cannot be accurately capturing the atmosphere

of this planet. Phase curves can also be produced from an atmospheric model and compared to those obtained observationally, allowing the direct comparison of model results and observational data. Further, phase curves of planets that have not yet been as closely studied may be predicted, potentially informing decisions on future observations, particularly in cases where a specific feature may prove detectable. Similarly, the detectability of features such as the high-altitude winds on HD 209458b (Snellen et al., 2010) may be predicted.

Inflated exoplanets, which cannot be replicated using only the techniques of this study, remain a fascinating area of investigation and could provide material for a large body of work. It would also be highly interesting to continue from the data here obtained, processing it in a more specific fashion to make such predictions as localised chemical abundance or depletion of species, or producing simulated transmission spectra either for comparison with observational results or to make predictions for such results.

Another interesting area of further enquiry would be to expand the number of factors accounted for during the evolutionary studies, taking into account the potential effects of migration during the course of the planet's history. All hot Jupiters are believed to have undergone extensive migration after their initial formation in order to reach their present locations, a factor which may affect their subsequent evolution.

References

Agol, E., Cowan, N. B., Knutson, H. A., Deming, D., Steffen, J. H., Henry, G. W., Charbonneau, D., 2010. The climate of HD 189733b from fourteen transits and eclipses measured by Spitzer. The Astrophysical Journal 721, 1861–1877.

Albrecht, S., Winn, J. N., Marcy, G. W., Howard, A. W., Isaacson, H., Johnson, J. A., Jul. 2013. Low Stellar Obliquities in Compact Multiplanet Systems. The Astrophysical Journal 771, 11 (14pp).

Anderson, D. R., Collier Cameron, A., Gillon, M., Hellier, C., Jehin, E., Lendl, M., Maxted, P. F. L., Queloz, D., Smalley, B., Smith, A. M. S., Triaud, A. H. M. J., West, R. G., Pepe, F., Pollacco, D., Ségransan, D., Todd, I., Udry, S., 2012. WASP-44b, WASP-45b and WASP-46b: three short-period, transiting extrasolar planets. Monthly Notices of the Royal Astronomical Society 422, 1988–1998.

Andrews, D. G., 2000. An Introduction to Atmospheric Physics. Cambridge University Press.

Andrews, D. G., Holton, J. R., Leovy, C. B., 1987. Middle Atmosphere Dynamics. Academic Press.

Arras, P., Bildsten, L., Oct. 2006. Thermal structure and radius evolution of irradiated gas giant planets. The Astrophysical Journal 650, 394–407.

Bagenal, F., Dowling, T. E., McKinnon, W. B. (Eds.), 2006. *Jupiter: The Planet, Satellites, and Magnetosphere*. Cambridge University Press, Ch. The Interior of Jupiter, pp. 35–57.

Bahcall, J. N., Basu, S., Pinsonneault, M., Serenelli, A. M., Jan. 2005. Helioseismological implications of recent solar abundance determinations. The Astrophysical Journal 618, 1049–1056.

Baraffe, I., Chabrier, G., Barman, T., 2010. The physical properties of extra-solar planets. Reports on Progress in Physics 73, 1–30.

Baruteau, C., Masset, F., 2013. Recent Developments in Planet Migration Theory. In: Souchay, J., Mathis, S., Tokieda, T. (Eds.), Tides in Astronomy and Astrophysics. Vol. 861 of Lecture Notes in Physics. Springer Berlin Heidelberg, pp. 201–253.

Bodenheimer, P., Lin, D. N. C., Mardling, R. A., Feb. 2001. On the Tidal Inflation of Short-Period Extrasolar Planets. The Astrophysical Journal 548, 466–472.

Bond, I. A., Udalski, A., Jaroszynski, M., Rattenbury, N. J., Paczynski, B., Soszynski, I., Wyrzykowski, L., Szymanski, M. K., Kubiak, M., Szewczyk, O., Zebrun, K., Pietrzynski, G., Abe, F., Bennett, D. P., Eguchi, S., Furuta, Y., Hearnshaw, J. B., Kamiya, K., Kilmartin, P. M., Kurata, Y., Masuda, K., Matsubara, Y., Muraki, Y., Noda, S., Okajima, K., Sako, T., Sekiguchi, T., Sullivan, D. J., Sumi, T., Tristram, P. J., Yanagisawa, T., Yock, P. C. M., The MOA and OGLE Collaborations, Apr. 2004. OGLE 2003-BLG-235/MOA 2003-BLG-53: A Planetary Microlensing Event. The Astrophysical Journal Letters 606 (2), L155–L158.

Bonnefoy, M., Lagrange, A.-M., Boccaletti, A., Chauvin, G., Apai, D., Allard, F., Ehrenreich, D., Girard, J. H. V., Mouillet, D., Rouan, D., Gratadour, D., Kasper, M., 2011. High angular resolution detection of β Pictoris b at 2.18 μm. Astronomy & Astrophysics 528, L15.

Borucki, W. J., Koch, D., Basri, G., Batalha, N., Brown, T., Caldwell, D., Caldwell, J., Christensen-Dalsgaard, J., Cochran, W. D., DeVore, E., Dunham, E. W., Dupree, A. K., III, T. N. G., Geary, J. C., Gilliland, R., Gould, A., Howell, S. B., Jenkins, J. M., Kondo, Y., Latham, D. W., Marcy, G. W., Meibom, S., Kjeldsen, H., Lissauer, J. J., Monet, D. G., Morrison, D., Sasselov, D., Tarter, J., Boss, A., Brownlee, D., Owen, T., Buzasi, D., Charbonneau, D., Doyle, L., Fortney, J., Ford, E. B., Holman, M. J., Seager, S., Steffen, J. H., Welsh, W. F., Rowe, J., Anderson, H., Buchhave, L., Ciardi, D., Walkowicz, L., Sherry, W., Horch, E., Isaacson, H., Everett, M. E., Fischer, D., Torres, G., Johnson, J. A., Endl, M., MacQueen, P., Bryson, S. T., Dotson, J., Haas, M., Kolodziejczak, J., Cleve, J. V., Chandrasekaran, H., Twicken, J. D., Quintana, E. V., Clarke, B. D., Allen, C., Li, J., Wu, H., Tenenbaum, P., Verner, E., Bruhweiler, F., Barnes, J., Prsa, A., Feb. 2010. Kepler Planet-Detection Mission: Introduction and First Results. Science 327, 977–980.

Boss, A. P., Jan. 1995. Proximity of Jupiter-Like Planets to Low-Mass Stars. Science 267, 360–362.

Boss, A. P., Basri, G., Kumar, S. S., Liebert, J., Martín, E. L., Reipurth, B., Zinnecker, H., Jun. 2003. Nomenclature: Brown Dwarfs, Gas Giant Planets, and ? In: Martín, E. (Ed.), Brown Dwarfs. Vol. 211 of IAU Symposium. p. 529.

Broeg, C., Fortier, A., Ehrenreich, D., Alibert, Y., Baumjohann, W., Benz, W., Deleuil, M., Gillon, M., Ivanov, A., Liseau, R., Meyer, M., Oloffson, G., Pagano, I., Piotto, G., Pollacco, D., Queloz, D., Ragazzoni, R., Renotte, E., Steller, M., Thomas, N., the CHEOPS team, 2013. CHEOPS: A transit photometry mission for ESAs small mission programme. In: European Physical Journal Web of Conferences. Vol. 47 of European Physical Journal

Web of Conferences. p. 03005.

Burkert, A., Lin, D. N. C., Bodenheimer, P. H., Jones, C. A., Yorke, H. W., Jan. 2005. On the surface heating of synchronously spinning short-period jovian planets. The Astrophysical Journal 618, 512–523.

Cabrera, J., Csizmadia, S., Lehmann, H., Dvorak, R., Gandolfi, D., Rauer, H., Erikson, A., Dreyer, C., Eigmüller, P., Hatzes, A., Jan. 2014. The planetary system to KIC 11442793: A compact analogue to the solar system. The Astrophysical Journal 781, 18 (13pp).

Carroll, B. W., Ostlie, D. A., 1996. An Introduction to Modern Astrophysics. Addison-Wesley.

Cassisi, S., Potekhin, A. Y., Pietrinferni, A., Catelan, M., Salaris, M., Jun. 2007. Updated electron-conduction opacities: The impact on low-mass stellar models. The Astrophysical Journal 661, 1094–1104.

Chabrier, G., Baraffe, I., 2000. Theory of Low-Mass Stars and Substellar Objects. Annual Review of Astronomy and Astrophysics 38, 337–377.

Charbonneau, D., Brown, T. M., Latham, D. W., Mayor, M., Jan. 2000. Detection of Planetary Transits across a Sun-like Star. The Astrophysical Journal Letters 529, L45–L48.

Chen, G., van Boekel, R., Wang, H., Nikolov, N., Seemann, U., Henning, T., Jul. 2014. Observed spectral energy distribution of the thermal emission from the dayside of WASP-46b. Astronomy & Astrophysics 567, A8, 8pp.

Cho, J. Y., Menou, K., Hansen, B. M. S., Seager, S., Mar. 2008. Atmospheric circulation of close-in extrasolar giant planets. I. global, barotropic, adiabatic simulations. The Astrophysical Journal 675, 817–845.

Cho, J. Y.-K., Menou, K., Hansen, B. M. S., Seager, S., Apr. 2003. The changing face of the extrasolar giant planet HD 209458b. The Astrophysical Journal Letters 587, L117–L120.

Cole, G. H. A., Woolfson, M. M., 2002. Planetary Science: The Science of Planets Around Stars. IOP Publishing.

Cooper, C. S., Showman, A. P., Aug. 2005. Dynamic meteorology at the photosphere of HD 209458b. The Astrophysical Journal Letters 629, L45–L48.

Davis, T. A., Wheatley, P. J., 2009. Evidence for a lost population of close-in exoplanets. Monthly Notices of the Royal Astronomical Society 396, 1012–1017.

de Pater, I., Lissauer, J. J., 2007. Planetary Sciences. Cambridge University Press.

Demory, B.-O., Seager, S., Nov. 2011. Lack of inflated radii for *KEPLER* giant planet candidates receiving modest stellar irradiation. The Astrophysical Journal Supplement Series 197, 12 (5pp).

Dobbs-Dixon, I., Agol, E., Burrows, A., Jun. 2012. The Impact of Circumplantary Jets on Transit Spectra and Timing Offsets for Hot Jupiters. The Astrophysical Journal 751, 87 (11pp).

Dobbs-Dixon, I., Cumming, A., Lin, D. N. C., Feb. 2010. Radiative Hydrodynamic Simulations of HD209458b: Temporal Variability. The Astrophysical Journal 710, 1395–1407.

Dobbs-Dixon, I., Lin, D. N. C., Jan. 2008. Atmospheric dynamics of short-period extrasolar gas giant planets. I. dependence of nightside temperature on opacity. The Astrophysical Journal 673, 513–525.

Eddington, A. S., 1926. Internal Constitution of the Stars. Cambridge University Press.

Ferguson, J. W., Alexander, D. R., Allard, F., Barman, T., Bodnarik, J. G., Hauschildt, P. H., Heffner-Wong, A., Tamanai, A., Apr. 2005. Low-temperature opacities. The Astrophysical Journal 623, 585–596.

Fortney, J. J., Nettelmann, N., 2010. The Interior Structure, Composition, and Evolution of Giant Planets. Space Sci Rev 152, 423–447.

Fortney, J. J., Shabram, M., Showman, A. P., Lian, Y., Freedman, R. S., Marley, M. S., Lewis, N. K., Feb. 2010. Transmission Spectra of Three-Dimensional Hot Jupiter Model Atmospheres. The Astrophysical Journal 709, 1396–1406.

Fossati, L., Haswell, C. A., Froning, C. S., L.Hebb, Holmes, S., Kolb, U., Helling, C., Carter, A., Wheatley, P., Cameron, A. C., Loeillet, B., Pollacco, D., Street, R., Stempels, H. C., Simpson, E., Udry, S., Joshi, Y. C., West, R. G., Skillen, I., Wilson, D., May 2010. Metals in the exosphere of the highly irradiated planet WASP-12b. The Astrophysical Journal Letters 714, L222–L227.

Fraedrich, K., Blessing, S., Kirk, E., Kunz, T., Luksch, U., Lunkeit, F., Sielmann, F., Jul. 2007. PUMA Users' Guide, Version 15.0. University of Hamburg.

Fraedrich, K., Kirk, E., Luksch, U., Lunkeit, F., Dec. 2005. The portable university model of the atmosphere (PUMA): Storm track dynamics and low-frequency variability. Meteorologische Zeitschrift 14 (6), 735–745.

Freedman, R. S., Marley, M. S., Lodders, K., Feb. 2008. Line and Mean Opacities for Ultracool Dwarfs and Extrasolar Planets. The Astrophysical Journal Supplement Series 174 (2), 504–513.

Gardner, J. P., Mather, J. C., Clampin, M., Doyon, R., Greenhouse, M. A., Hammel, H. B., Hutchings, J. B., Jakobsen, P., Lilly, S. J., Long, K. S., Lunine, J. I., McCaughrean, M. J., Mountain, M., Nella, J., Rieke, G. H., Rieke, M. J., Rix, H.-W., Smith, E. P., Sonneborn,

G., Stiavelli, M., Stockman, H. S., Windhorst, R. A., Wright, G. S., 2006. The James Webb Space Telescope. Space Science Reviews 123, 485–606.

Gaudi, B. S., Sep. 2012. Microlensing surveys for exoplanets. Annual Review of Astronomy and Astrophysics 50, 411–453.

Grieger, B., Segschneider, J., Keller, H. U., Rodin, A. V., Lunkeit, F., Kirk, E., Fraedrich, K., 2004. Simulating Titan's tropospheric circulation with the Portable University Model of the Atmosphere. Advances in Space Research 34, 1650–1654.

Guillot, T., Sep. 2010. On the radiative equilibrium of irradiated planetary atmospheres. Astronomy & Astrophysics 520, A27, 13pp.

Guillot, T., Showman, A. P., Apr. 2002. Evolution of "51Pegasus b-like" planets. Astronomy & Astrophysics 385, 156–165.

Haswell, C. A., 2010. Transiting Exoplanets. Cambridge University Press.

Hebb, L., Collier-Cameron, A., Loeillet, B., Pollacco, D., Hébrard, G., Street, R. A., Bouchy, F., Stempels, H. C., Moutou, C., Simpson, E., Udry, S., Joshi, Y. C., West, R. G., Skillen, I., Wilson, D. M., McDonald, I., Gibson, N. P., Aigrain, S., Anderson, D. R., Benn, C. R., Christian, D. J., Enoch, B., Haswell, C. A., Hellier, C., Horne, K., Irwin, J., Lister, T. A., Maxted, P., Mayor, M., Norton, A. J., Parley, N., Pont, F., Queloz, D., Smalley, B., Wheatley, P. J., Mar. 2009. WASP-12b: The hottest transiting extrasolar planet yet discovered. The Astrophysical Journal 693, 1920–1928.

Held, I. M., Suarez, M. J., Oct. 1994. A Proposal for the Intercomparison of the Dynamical Cores of Atmospheric General Circulation Models. Bulletin of the American Meteorological Society 75, 1825–1830.

Hellier, C., Anderson, D. R., Gillon, M., Lister, T. A., Maxted, P. F. L., Queloz, D., Smalley, B., Triaud, A. H. M. J., West, R. G., Wilson, D. M., Alsubai, K., Bentley, S. J., Collier Cameron, A., Hebb, L., Horne, K., Irwin, J., Kane, S. R., Mayor, M., Pepe, F., Pollacco, D., Skillen, I., Udry, S., Wheatley, P. J., Christian, D. J., Enoch, R., Haswell, C. A., Joshi, Y. C., Norton, A. J., Parley, N., Ryans, R., Street, R. A., Todd, I., Jan. 2009. WASP-7: A bright transiting-exoplanet system in the southern hemisphere. The Astrophysical Journal Letters 690, L81–L91.

Heng, K., Hayek, W., Pont, F., Sing, D. K., Feb. 2012. On the effects of clouds and hazes in the atmospheres of hot Jupiters: semi-analytical temperature-pressure profiles. Monthly Notices of the Royal Astronomical Society 420, 20–36.

Heng, K., Menou, K., Phillipps, P. J., 2011. Atmospheric circulation of tidally-locked exoplanets: a suite of benchmark tests for dynamical solvers. Monthly Notices of the Royal Astronomical Society 413, 2380–2402.

Henry, G., Marcy, G., Butler, R. P., Vogt, S. S., Nov. 1999. HD 209458. IAU Circ. 7307, 1.

Henry, G. W., Marcy, G. W., Butler, R. P., Vogt, S. S., Jan. 2000. A transiting "51 peg-like" planet. The Astrophysical Journal Letters 529, L41–L44.

Henyey, L., Vardya, M. S., Bodenheimer, P., Oct. 1965. Studies in stellar evolution. III. the calculation of model envelopes. The Astrophysical Journal 142, 841–854.

Henyey, L. G., Wilets, L., Bohm, K. H., LeLevier, R., Levee, R. D., May 1959. A method for automatic computation of stellar evolution. The Astrophysical Journal 129, 628–636.

Houghton, J. T., 1986. The Physics of Atmospheres, 2nd Edition. Cambridge University Press.

Hut, P., Jun. 1981. Tidal Evolution in Close Binary Systems. Astronomy & Astrophysics 99, 126–140.

Ibgui, L., Burrows, A., Aug. 2009. Coupled Evolution with Tides of the Radius and Orbit of Transiting Giant Planets: General Results. The Astrophysical Journal 700, 1921–1932.

Iglesias, C. A., Rogers, F. J., Aug. 1993. Radiative opacities for carbon- and oxygen-rich mixtures. The Astrophysical Journal 412, 752–760.

Iglesias, C. A., Rogers, F. J., Jun. 1996. Updated opal opacities. The Astrophysical Journal 464, 943–953.

Iro, N., Bzard, B., Guillot, T., 2005. A time-dependent radiative model of HD209458b. Astronomy & Astrophysics 436, 719–727.

Jackson, B., Barnes, R., Greenberg, R., Jun. 2009. Observational evidence for tidal destruction of exoplanets. The Astrophysical Journal 698, 1357–1366.

James, I. N., 1994. Introduction to Circulating Atmospheres. Cambridge Atmospheric and Space Science Series. Cambridge University Press.

Kalas, P., Graham, J. R., Chiang, E., Fitzgerald, M. P., Clampin, M., Kite, E. S., Stapelfeldt, K., Marois, C., Krist, J., Nov. 2008. Optical Images of an Exosolar Planet 25 Light-Years from Earth. Science 322 (5906), 1345–1348.

Kitchin, C. R., 2003. Astrophysical Techniques, 4th Edition. Taylor & Francis Group.

Kley, W., Nelson, R. P., Sep. 2012. Planet-Disk Interaction and Orbital Evolution. Annual Review of Astronomy and Astrophysics 50, 211–249.

Knutson, H. A., Charbonneau, D., Allen, L. E., Fortney, J. J., Agol, E., Cowan, N. B., Showman, A. P., Cooper, C. S., Megeath, S. T., May 2007. A map of the day-night contrast of the extrasolar planet HD 189733b. Nature 447, 183–186.

Krishna Swamy, K. S., Jul. 1966. Profiles of strong lines in k-dwarfs. The Astrophysical Journal 145, 174–194.

Langton, J., Laughlin, G., Mar. 2007. Observational Consequences of Hydrodynamic Flows on Hot Jupiters. The Astrophysical Journal 657, L113–L116.

Langton, J., Laughlin, G., Jun. 2008. Persistent circumpolar vortices on the extrasolar giant planet HD 37605 b. Astronomy & Astrophysics 483, L25–L28.

Leconte, J., G.Chabrier, Baraffe, I., Levrard, B., Jun. 2010. Is tidal heating sufficient to explain bloated exoplanets? Consistent calculations accounting for finite initial eccentricity. Astronomy & Astrophysics 516, A64.

Leethochawalit, N., Jones, T. A., Ellis, R. S., Stark, D. P., Richard, J., Zitrin, A., Auger, M., Apr. 2016. A Keck adaptive optics survey of a representative sample of gravitationally lensed star-forming galaxies: High spatial resolution studies of kinematics and metallicity gradients. The Astrophysical Journal 820 (2), 84 (18pp).

Lewis, S. R., Read, P. L., Apr. 2003. Equatorial jets in the dusty Martian atmosphere. Journal of Geophysical Research 108 (E4).

Li, S., Miller, N., Lin, D. N. C., Fortney, J. J., Feb. 2010. WASP-12b as a prolate, inflated and disrupting planet from tidal dissipation. Nature 463, 1054–1056.

Liakka, J., 2006. Validation of the dynamical core of the Portable University Model of the Atmosphere (PUMA). Master's thesis, Institute of Meteorology and Geophysics, University of Innsbruck.

Lissauer, J. J., Fabrycky, D. C., Ford, E. B., Borucki, W. J., Fressin, F., Marcy, G. W., Orosz, J. A., Rowe, J. F., Torres, G., Welsh, W. F., Batalha, N. M., Bryson, S. T., Buchhave, L. A., Caldwell, D. A., Carter, J. A., Charbonneau, D., Christiansen, J. L., Cochran, W. D., Desert, J.-M., Dunham, E. W., Fanelli, M. N., Fortney, J. J., Gautier, III, T. N., Geary, J. C., Gilliland, R. L., Haas, M. R., Hall, J. R., Holman, M. J., Koch, D. G., Latham, D. W., Lopez, E., McCauliff, S., Miller, N., Morehead, R. C., Quintana, E. V., Ragozzine, D., Sasselov, D., Short, D. R., Steffen, J. H., Feb. 2011. A closely packed system of low-mass, low-density planets transiting Kepler-11. Nature 470, 53–58.

Lovis, C., Segransan, D., Mayor, M., Udry, S., Benz, W., Bertaux, J.-L., Bouchy, F., Correia, A. C. M., Laskar, J., Lo Curto, G., Mordasini, C., Pepe, F., Queloz, D., Santos, N. C.,

2011. The HARPS search for southern extra-solar planets XXVIII. Up to seven planets orbiting HD 10180: probing the architecture of low-mass planetary systems. Astronomy & Astrophysics 528, A112, 16pp.

MacDonald, J., Mullan, D. J., Apr. 2012. Precision modelling of M dwarf stars: the magnetic components of CM Draconis. Monthly Notices of the Royal Astronomical Society 421, 3084–3101.

Majeau, C., Agol, E., Cowan, N. B., Mar. 2012. A two-dimensional infrared map of the extrasolar planet HD 189733b. The Astrophysical Journal Letters 747, L20 (5pp).

Mayor, M., Queloz, D., Nov. 1995. A Jupiter-mass companion to a solar-type star. Nature 378, 355–359.

Menou, K., Cho, J. Y.-K., Seager, S., Hansen, B. M. S., Apr. 2003. "Weather" Variability of Close-In Extrasolar Giant Planets. The Astrophysical Journal 587, L113–L116.

Menou, K., Rauscher, E., Jul. 2009. Atmospheric circulation of hot Jupiters: a shallow three-dimensional model. The Astrophysical Journal 700, 887–897.

Menou, K., Rauscher, E., Apr. 2010. Radiation-Hydrodynamics of Hot Jupiter Atmospheres. The Astrophysical Journal 713, 1174–1182.

Mohr, P. J., Taylor, B. N., Newell, D. B., Apr. 2008. CODATA recommended values of the fundamental physical constants: 2006. Reviews of Modern Physics 80, 633–730.

Morzinski, K. M., Males, J. R., Skemer, A. J., Close, L. M., Hinz, P. M., Rodigas, T. J., Puglisi, A., Esposito, S., Riccardi, A., Pinna, E., Xompero, M., Briguglio, R., Bailey, V. P., Follette, K. B., Kopon, D., Weinberger, A. J., Wu, Y.-L., Dec. 2015. Magellan adaptive optics first-light observations of the exoplanet β Pic b. II. 35 μm direct imaging with MagAO+Clio, and the empirical bolometric luminosity of a self-luminous giant planet. The Astrophysical Journal 815 (2), 108 (24pp).

Muterspaugh, M. W., Lane, B. F., Kulkarni, S. R., Konacki, M., Burke, B. F., Colavita, M. M., Shao, M., Hartkopf, W. I., Boss, A. P., Williamson, M., Oct. 2010. The PHASES differential astrometry data archive. V. candidate substellar companions to binary systems. The Astronomical Journal 140 (6), 1657–1671.

Nettelmann, N., Oct. 2011. Predictions on the core mass of Jupiter and of giant planets in general. Astrophysics & Space Science 336, 47–51.

Paxton, B., Bildsten, L., Dotter, A., Herwig, F., Lesaffre, P., Timmes, F., Jan. 2011. Modules for Experiments in Stellar Astrophysics (MESA). The Astrophysical Journal Supplement Series 192 (1), 35pp.

Paxton, B., Cantiello, M., Arras, P., Bildsten, L., Brown, E. F., Dotter, A., Mankovich, C., Montgomery, M. H., Stello, D., Timmes, F. X., Townsend, R., 2013. Modules for experiments in stellar astrophysics (MESA): Giant planets, oscillations, rotation, and massive stars. The Astrophysical Journal Supplement Series 208, 4 (43pp).

Perna, R., Heng, K., Pont, F., 2012. The effects of irradiation on hot Jovian atmospheres: heat redistribution and energy dissipation. The Astrophysical Journal 751, 59.

Perryman, M. A. C., de Boer, K. S., Gilmore, G., Hog, E., Lattanzi, M. G., Lindegren, L., Luri, X., Mignard, F., Pace, O., de Zeeuw, P. T., 2001. GAIA: Composition, formation and evolution of the Galaxy. Astronomy & Astrophysics 369, 339–363.

Pollacco, D. L., Skillen, I., Cameron, A. C., Christian, D. J., Hellier, C., Irwin, J., Lister, T. A., Street, R. A., West, R. G., Anderson, D., Clarkson, W. I., Deeg, H., Enoch, B., Evans, A., Fitzsimmons, A., Haswell, C. A., Hodgkin, S., Horne, K., Kane, S. R., Keenan, F. P., Maxted, P. F. L., Norton, A. J., Osborne, J., Parley, N. R., Ryans, R. S. I., Smalley, B., Wheatley, P. J., Wilson, D. M., Oct. 2006. The WASP Project and the SuperWASP Cameras. Publications of the Astronomical Society of the Pacific 118, 1407–1418.

Potekhin, A. Y., Chabrier, G., Jan. 2010. Thermodynamic functions of dense plasmas: Analytic approximations for astrophysical applications. Contributions to Plasma Physics 50, 82–87.

Prialnik, D., 2000. An Introduction to the Theory of Stellar Structure and Evolution. Cambridge University Press.

Rauer, H., Catala, C., Aerts, C., Appourchaux, T., Benz, W., Brandeker, A., Christensen-Dalsgaard, J., Deleuil, M., Gizon, L., Goupil, M.-J., andE. Janot-Pacheco, M. G., Mas-Hesse, M., Pagano, I., Piotto, G., Pollacco, D., Santos, N. C., Smith, A., Suarez, J.-C., Szabo, R., Udry, S., Adibekyan, V., Alibert, Y., Almenara, J.-M., maro Seoane, P. A., von Eiff, M. A., Asplund, M., Antonello, E., Barnes, S., Baudin, F., Belkacem, K., Bergemann, M., Bihain, G., Birch, A. C., Bonfils, X., Boisse, I., Bonomo, A. S., Borsa, F., Brandao, I. M., Brocato, E., Brun, S., Burleigh, M., Burston, R., Cabrera, J., Cassisi, S., Chaplin, W., Charpinet, S., Chiappini, C., Church, R. P., Csizmadia, S., Cunha, M., Damasso, M., Davies, M. B., Deeg, H. J., Diaz, R. F., Dreizler, S., Dreyer, C., Eggenberger, P., Ehrenreich, D., Eigmuller, P., Erikson, A., Farmer, R., Feltzing, S., de Oliveira Fialho, F., Figueira, P., Forveille, T., Fridlund, M., Garcia, R. A., Giommi, P., Giuffrida, G., Godolt, M., da Silva, J. G., Granzer, T., Grenfell, J. L., Grotsch-Noels, A., Gunther, E., Haswell, C. A., Hatzes, A. P., Hebrard, G., Hekker, S., Helled, R., Heng, K., Jenkins, J. M., Johansen, A., Khodachenko, M. L., Kislyakova, K. G., Kley, W., Kolb, U., Krivova,

N., Kupka, F., Lammer, H., Lanza, A. F., Lebreton, Y., Magrin, D., Marcos-Arenal, P., Marrese, P. M., Marques, J. P., Martins, J., Mathis, S., Mathur, S., Messina, S., Miglio, A., Montalban, J., Montalto, M., Monteiro, M. J. P. F. G., Moradi, H., Moravveji, E., Mordasini, C., Morel, T., Mortier, A., Nascimbeni, V., Nelson, R. P., Nielsen, M. B., Noack, L., Norton, A. J., Ofir, A., Oshagh, M., Ouazzani, R.-M., Papics, P., Parro, V. C., Petit, P., Plez, B., Poretti, E., Quirrenbach, A., Ragazzoni, R., Raimondo, G., Rainer, M., Reese, D. R., Redmer, R., Reffert, S., Rojas-Ayala, B., Roxburgh, I. W., Salmon, S., Santerne, A., Schneider, J., Schou, J., Schuh, S., Schunker, H., Silva-Valio, A., Silvotti, R., Skillen, I., Snellen, I., Sohl, F., Sousa, S. G., Sozzetti, A., Stello, D., Strassmeier, K. G., Svanda, M., Szabo, G. M., Tkachenko, A., Valencia, D., Grootel, V. V., Vauclair, S. D., Ventura, P., Wagner, F. W., Walton, N. A., Weingrill, J., Werner, S. C., Wheatley, P. J., Zwintz, K., 2014. The PLATO 2.0 mission. Experimental Astronomy 38, 249–330.

Rauscher, E., Menou, K., May 2010. Three-dimensional modeling of hot jupiter atmospheric flows. The Astrophysical Journal 714, 1334–1342.

Rauscher, E., Menou, K., May 2012a. A general circulation model for gaseous exoplanets with double-gray radiative transfer. The Astrophysical Journal 750, 96–109.

Rauscher, E., Menou, K., Jan. 2012b. The Role of Drag in the Energetics of Strongly Forced Exoplanet Atmospheres. The Astrophysical Journal 745, 78 (12pp).

Rauscher, E., Menou, K., Cho, J. Y.-K., Seager, S., Hansen, B. M. S., 2008. On Signatures of Atmospheric Features in Thermal Phase Curves of Hot Jupiters. The Astrophysical Journal 681, 1646–1652.

Ricker, G. R., Winn, J. N., Vanderspek, R., Latham, D. W., Bakos, G. A., Bean, J. L., Berta-Thompson, Z. K., Brown, T. M., Buchhave, L., Butler, N. R., Butler, R. P., Chaplin, W. J., Charbonneau, D., Christensen-Dalsgaard, J., Clampin, M., Deming, D., Doty, J., Lee, N. D., Dressing, C., Dunham, E. W., Endl, M., Fressin, F., Ge, J., Henning, T., Holman, M. J., Howard, A. W., Ida, S., Jenkins, J., Jernigan, G., Johnson, J. A., Kaltenegger, L., Kawai, N., Kjeldsen, H., Laughlin, G., Levine, A. M., Lin, D., Lissauer, J. J., MacQueen, P., Marcy, G., McCullough, P. R., Morton, T. D., Narita, N., Paegert, M., Palle, E., Pepe, F., Pepper, J., Quirrenbach, A., Rinehart, S. A., Sasselov, D., Sato, B., Seager, S., Sozzetti, A., Stassun, K. G., Sullivan, P., Szentgyorgyi, A., Torres, G., Udry, S., Villasenor, J., Aug. 2014. Transiting Exoplanet Survey Satellite (TESS). In: Space Telescopes and Instrumentation 2014: Optical, Infrared, and Millimeter Wave. Vol. 9143 of Proc. SPIE. p. 914320.

Rigaut, F., Dec. 2015. Astronomical adaptive optics. Publications of the Astronomical Society of the Pacific 127, 1197–1203.

Rogers, F. J., Nayfonov, A., Sep. 2002. Updated and Expanded OPAL Equation-of-State Tables: Implications for Helioseismology. The Astrophysical Journal 576, 1064–1074.

Saumon, D., Chabrier, G., Van Horn, H. M., Aug. 1995. An equation of state for low-mass stars and giant planets. The Astrophysical Journal Supplement Series 99, 713–741.

Schmitt, J. R., Wang, J., Fischer, D. A., Jek, K. J., Moriarty, J. C., Boyajian, T. S., Schwamb, M. E., Lintott, C., Lynn, S., Smith, A. M., Parrish, M., Schawinski, K., Simpson, R., LaCourse, D., Omohundro, M. R., Winarski, T., Goodman, S. J., Jebson, T., Schwengeler, H. M., Paterson, D. A., Sejpka, J., Terentev, I., Jacobs, T., Alsaadi, N., Bailey, R. C., Ginman, T., Granado, P., Guttormsen, K. V., Mallia, F., Papillon, A. L., Rossi, F., Socolovsky, M., Aug. 2014. Planet Hunters. VI. an independent characterization of KOI-351 and several long period planet candidates from the kepler archival data. The Astronomical Journal 148, 28 (11pp).

Schneider, J., 1995-2015. The Extrasolar Planets Encyclopaedia.
URL `http://exoplanet.eu`

Seager, S., Deming, D., 2010. Exoplanet atmospheres. Annual Review of Astronomy and Astrophysics 48, 631–672.

Seaton, M. J., 2005. Opacity Project data on CD for mean opacities and radiative accelerations. Monthly Notices of the Royal Astronomical Society 362, L1–L3.

Showman, A. P., Cooper, C. S., Fortney, J. J., Marley, M. S., Jul. 2008. Atmospheric circulation of hot Jupiters: Three-dimensional circulation models of HD 209458b and HD 189733b with simplified forcing. The Astrophysical Journal 682, 559–576.

Showman, A. P., Fortney, J. J., Lian, Y., Marley, M. S., Freedman, R. S., Knutson, H. A., Charbonneau, D., Jul. 2009. Atmospheric circulation of hot Jupiters: Coupled radiative-dynamical general circulation model simulations of HD 189733b and HD 209458b. The Astrophysical Journal 699, 564–584.

Showman, A. P., Guillot, T., 2002. Atmospheric circulation and tides of "51Pegasus b-like" planets. Astronomy & Astrophysics 385, 166–180.

Showman, A. P., Polvani, L. M., Sep. 2011. Equatorial Superrotation on Tidally Locked Exoplanets. The Astrophysical Journal 738, 71 (24pp).

Smith, R. C., 1995. Observational Astrophysics. Cambridge University Press.

Snellen, I. A. G., de Kok, R. J., de Mooij, E. J. W., Albrecht, S., Jun. 2010. The orbital motion, absolute mass and high-altitude winds of exoplanet HD209458b. Nature 465, 1049–1051.

Southworth, J., Dominik, M., Jrgensen, U. G., Rahvar, S., Snodgrass, C., Alsubai, K., Bozza, V., Browne, P., Burgdorf, M., Calchi Novati, S., Dodds, P., Dreizler, S., Finet, F., Gerner, T., Hardis, S., Harpse, K., Hellier, C., Hinse, T. C., Hundertmark, M., Kains, N., Kerins, E., Liebig, C., Mancini, L., Mathiasen, M., Penny, M. T., Proft, S., Ricci, D., Sahu, K., Scarpetta, G., Schfer, S., Schnebeck, F., Surdej, J., Mar. 2011. A much lower density for the transiting extrasolar planet WASP-7. Astronomy & Astrophysics 527, A8.

Thrastarson, H. T., Cho, J. Y.-K., Jun. 2010. Effects of Initial Flow on Close-In Planet Atmospheric Circulation. The Astrophysical Journal 716, 144–153.

Thrastarson, H. T., Cho, J. Y.-K., Mar. 2011. Relaxation Time and Dissipation Interaction in Hot Planet Atmospheric Flow Simulations. The Astrophysical Journal 729, 117–+.

Timmes, F. X., Swesty, F. D., Feb. 2000. The accuracy, consistency, and speed of an electron-positron equation of state based on table interpolation of the helmholtz free energy. The Astrophysical Journal Supplement Series 126, 501–516.

Tuomi, M., 2012. Evidence for nine planets in the HD 10180 system. Astronomy & Astrophysics 543, A52, 12pp.

Wahl, S. M., Wilson, H. F., Militzer, B., Aug. 2013. Solubility of iron in metallic hydrogen and stability of dense cores in giant planets. The Astrophysical Journal 773, 95 (5pp).

Watkins, C., Cho, J. Y., May 2010. Gravity waves on hot extrasolar planets. I. Propagation and interaction with the background. The Astrophysical Journal 714, 904–914.

Weiss, A., Hillebrandt, W., Thomas, H.-C., Ritter, H., 2004. Cox & Giuli's Principles of Stellar Structure, extended 2nd Edition. Advances in Astronomy and Astrophysics. Cambridge Scientific Publishers.

Wilson, H. F., Militzer, B., Mar. 2012a. Rocky Core Solubility in Jupiter and Giant Exoplanets. Physical Review Letters 108, 111101.

Wilson, H. F., Militzer, B., Jan. 2012b. Solubility of water ice in metallic hydrogen: consequences for core erosion in gas giant planets. The Astrophysical Journal 745, 54–59.

Wolszczan, A., Frail, D. A., Jan. 1992. A planetary system around the millisecond pulsar PSR1257+12. Nature 355, 145–147.